INVESTIGATION OF IMAGE ERRORS IN VLBI IMAGES OF SN 1993J

BAHMAN KARIMI

A THESIS SUBMITTED TO THE FACULTY OF
GRADUATE STUDIES IN PARTIAL FULFILMENT
OF THE REQUIREMENTS FOR THE DEGREE OF

MASTER OF SCIENCE

GRADUATE PROGRAM IN PHYSICS AND ASTRONOMY
YORK UNIVERSITY
TORONTO, ONTARIO

October 2013

INVESTIGATION OF IMAGE ERRORS IN VLBI IMAGES OF SN 1993J

BAHMAN KARIMI

A THESIS SUBMITTED TO THE FACULTY OF
GRADUATE STUDIES IN PARTIAL FULFILMENT
OF THE REQUIREMENTS FOR THE DEGREE OF

MASTER OF SCIENCE

GRADUATE PROGRAM IN PHYSICS AND ASTRONOMY
YORK UNIVERSITY
TORONTO, ONTARIO

October 2013

Abstract

All deconvolved images from observational data obtained from very-long-baseline interferometry (VLBI) arrays are subject to image errors. They are caused by noise and incomplete sampling in the u-v plane. To investigate image errors we simulated data on the basis of VLBI observations of SN 1993J taken on 2007 Nov. 3. We computed the brightness distribution of a model of a supernova, calculated the visibility data of the model and made an image with the simulated data. The difference between model image and the image made with the simulated data indicates image errors. We found that image errors are larger by a factor ~ 1.6 than the rms fluctuations of the background noise. We investigated the modulation of the brightness around the ridge of the shell and concluded that brightness variations are significant for the 2007 observations and also for those made in 1996, 1997 and 2010.

Acknowledgement

I would like to express my gratitude to my supervisor Professor Norbert Bartel for providing outstanding supervision and engagement through the learning process of this Master thesis. He has been very helpful, patient and understanding of my conditions for the past four years. He spent countless hours to correct this thesis.

I would like to thank Dr. Michael Bietenholz for teaching me AIPS and helping me to do research for this thesis by spending countless hours.

Thank you to Professors Marshal McCall and Michael De Robertis for their advice and guidance as members of my supervisory committee. Also I would like to thank Marlene Caplan for her advice and help.

Thank you to my parents for all they have done for my education. Finally, thank you to my wife, Maryam for her never-ending support, unconditional love, and the happiness she brings to my life.

Contents

List of Tables

List of figures

Introduction

1.1 Astrophysical motivation

Supernovae are among the most energetic single events in the universe. They represent the explosive end stage of stars. To study the structure, evolution, kinematics and astrophysical nature of supernovae, images of them are of utmost importance. However, supernovae have been detected in modern times only in other galaxies which are so far away from Earth that they cannot be in general angularly resolved with optical telescopes. Only radio technique of very-long-baseline interferometry (VLBI) provides a means to resolve these sources on the sky and study them in detail.

Supernovae have been observed with VLBI since 1982 (Bartel et al. 1985) and images have been obtained with an angular resolution about 100 times better than what could have been obtained with the Hubble Space Telescope. The supernova most intensively studied with VLBI is SN 1993J. Since the first measurements from 1993 onward (Bartel et al. 1994; Marcaide et al. 1994), tens of images have been made of the expanding supernova (Bietenholz et al. 2010; Marcaide et al. 2012). These images show a shell of emission with apparent brightness modulations around the rim and no clear sign of a central source that may be expected as the remnant of the exploded star.

The shell itself and the modulations around the rim give important information about the

interaction of the ejecta of the supernova with the circumstellar medium left over from the progenitor star. The central region of the shell is expected to become transparent with time and may reveal the centre of explosion and its environment. A detailed study of the expanding shell, the modulation around the rim, their changes with time and a search of a central source is of high interest. However, images are subject to image errors, and a thorough study of such errors is important for the astrophysical interpretation of the images. Such detailed study is the subject of this thesis.

1.2 VLBI

Very-long-baseline-interferometry (VLBI) is a radio astronomical technique to obtain sky positions and images of celestial radio sources with an accuracy and angular resolution 100 times higher than those obtainable with the Hubble Space Telescope. For this technique many radio telescopes at distances of up to about 12,000 km apart are used to synthesize a virtual radio telescope that has an angular resolving power of a radio telescope as big as the Earth itself. Its angular resolution at a frequency of 5 GHz is ~ 1 milliarcsecond (mas). Many telescopes form an interferometer array. This array is pointed toward celestial radio sources, and data are recorded at each individual telescope and stored on magnetic tapes in the past and on disks at present.

The telescopes are synchronized with the aid of hydrogen maser clocks at each of the telescopes. These are the most accurate clocks for observational periods of the order of a

day. After the observations are finished, the tapes or disks are shipped to a central correlator. In some cases the data can be transmitted to the central correlator via the internet. Then the data from each pair of the VLBI array of antennas are correlated. The output from the correlator contains visibility data of the observed celestial source that depend on the characteristics of the pair of telescopes such as their sensitivities, their projected separations and their orientation as seen from the celestial source. These visibility data are Fourier transformed to make an image of the observed celestial source with an extremely high angular resolution. The imaging process, however, is not straightforward since the synthesized virtual radio telescope is not equivalent to a telescope with a solid surface. Quite the opposite, the solid part of the synthesized array consists only of the relatively small antennas that move with the Earth during the course of a day. Most of the surface of the synthesized virtual radio antenna is empty space. This has repercussions for the imaging process and the quality of the images.

1.3 VLBI imaging

In VLBI observations a particular imaging process is used to compensate for the shortcomings of the synthesized antenna as large as the Earth. A widely used software package is the Astronomical Image Processing System (AIPS) of the National Radio Astronomy Observatory (NRAO) that we also use for our studies. The sources studied with VLBI are compact sources, such as active galactic nuclei in radio galaxies, quasars, pulsars, celestial masers, radio stars and radio supernovae. The high-resolution images of these

radio sources enable us to obtain unique information about their dynamics and kinematics and to study their astrophysical nature. All images made from VLBI observations are subject to significant systematic errors. One important kind of error is the image errors. In this this thesis, image errors in VLBI images of SN1993J are investigated in detail to allow for a more reliable interpretation of the astrophysical nature of the supernova.

1.4 Image errors

Image errors in VLBI images arise from noise and incomplete sampling of the u-v coverage generated by the array of antennas. The gaps in the u-v coverage produce sidelobes in the images that are larger than hose in the case where no gaps occurred. Sidelobes are generated from each brightness feature in the image. If there is only one brightness feature in the image the sidelobes appear as ripples around this feature. If there are many brightness features in the image then the ripples can overlap and interfere and a more complex sidelobe pattern can occur. Sidelobes from bright features within an image are likely to obscure any fainter features. To reduce the sidelobes, an algorithm called CLEAN (Hogbom, 1974), which will be fully described later in the thesis, is often used, but this algorithm is not perfect and produces image errors. Such image errors can cause a misinterpretation of VLBI images since the images with such errors do not represent the true sky brightness distribution of the source. Thus, understanding how image errors in VLBI images can be reduced is important for

astrophysical studies. By reducing image errors we can increase the fidelity and improve the interpretation of VLBI images significantly. Having images with smaller image errors could then reveal features of the structure of the source that otherwise could not be known to be due to the source.

This study will report on investigating image errors in VLBI images of SN 1993J which have been observed with VLBI from one month after the explosion to the present and several tens of images obtained to study the evolution of the structure of the expanding radio shell. All these images are subject to image errors. Our study will show how image errors in VLBI images can be minimized.

1.5 Thesis objectives

This section will define the objectives and the scope of this thesis. The objectives of this thesis are: to provide the fundamental information about the technique of interferometry, to study the main characteristics of SN 1993J, to introduce different models of a supernova, namely a symmetric spherical shell model, an asymmetric spherical shell model and a disk model, to simulate of VLBI observations for different model supernovae, to investigated on of image errors in clean images made from simulated VLBI observations to figure out what selection of parameters in the CLEAN algorithm can make clean images with image errors as small as possible, to quantify image errors in clean images made from simulated visibility data and real visibility data, to introduce

the "best" clean image of SN 1993J with the smallest image errors and relatively good resolution, to search for any compact source such as pulsar a wind nebula (PWN) or an emission region associated with a black hole which may exist in the centre of SN 1993J, and if not found, to set a conservative limit on the flux density of such a compact source in the centre of SN1993J.

In Chapter 2 we discuss the concept of VLBI and synthesized imaging in radio astronomy. In Chapter 3 we introduce supernovae in general and SN 1993J in particular. We also introduce SN 1986J as a supernova which is of importance in this thesis because of it has a compact source in its centre. In Chapter 4 we present different models of supernovae, namely the symmetric spherical shell model, asymmetric spherical shell model and disk model. We describe the simulation study of VLBI observations for different realizations of noise, channel-averaged noise and zero noise, different models of a supernova, different angular diameters of a supernova, different weighting schemes, different values of the robustness factor, different number of clean components, different values of gain and different u-v coverages, all in Chapter 5.

In Chapter 6 we report the results of our simulation study. In Chapter 7 we display the "best" clean images of SN 1993J from VLBI observations, present an investigation of the modulation of the brightness distribution along the ridge of the shell and also a search for, for instance, a PWN that can be expected in the centre of SN 1993J. In Chapter 8 we

give a discussion of the obtained results based on the comparison of clean images from our simulations study with clean images of SN 1993J taken from earlier epochs, namely 1996 Dec. 13 and 1997 Nov. 15, and also from the latest epoch of VLBI observations taken on 2010 Mar. 5. Finally, in Chapter 9, we give our conclusions based on our results and discussion.

2. Technique of VLBI

Interferometry in general and VLBI in particular can be best understood in terms of a set of pairs of antennas. In Figure 2.1 the basic characteristics of one pair of antennas are sketched. This figure shows the geometrical relationship between the x-y sky plane and the u-v plane or aperture plane. The baseline vector of two telescopes is called $\vec{B}$. The magnitude of this vector is the separation between two antennas. If the orientation of $\vec{B}$ is such that it is perpendicular to the line of sight to the observed source, then the two antennas appear at their largest separation seen from the source. If the orientation of $\vec{B}$ is different, then the projected baseline length, B cosφ, becomes relevant.

The angular resolution of the antenna pair is given by $\theta \sim \lambda/(B\cos\varphi)$, where λ is the wavelength of the incoming radiation. For example, a wavelength of 3.6 cm (frequency, ν=8.4 GHz) and a projected baseline of 10,000 km, gives a resolution of ~ 0.7 mas. As the Earth rotates, the projected length and orientation of the baseline of a pair of antennas changes with time and results in a u-v track on the u-v plane. This u-v plane is perpendicular to the line of sight to the target source. One can think of it as a plane seen from the source on which the baseline vector, $\vec{B}$, is projected with one end being in the centre of the u-v coordinate system. When the Earth rotates, the projected baseline length and orientation change and an ellipse is drawn on the u-v plane. Having more than two

radio telescopes results in more baselines each projected on the u-v plane with the Earth rotating, and more ellipses than only one are produced on the u-v plane . This results in more u-v tracks and a more densely covered u-v plane. For three antennas, A, B, C, three independent baselines can be formed, AB, BC and AC. For an array with n antennas, the number of independent antenna pairs or baselines is n(n-1)/2. We used 18 radio telescopes to observe SN 1993J on 2007 Nov. 3. This results in 153 independent baselines with one track for each baseline on the u-v plane. The whole set of tracks on the u-v plane makes a u-v coverage. Every track on the u-v plane is related to one individual baseline. A good u-v coverage can be achieved by proper selection of the individual antennas, selection of a circumpolar source and optimally using the rotation of the Earth to generate long u-v tracks. I (x, y) is the brightness distribution of the source on the sky that is observed by the interferometer. The x-y plane is tangential to the celestial sphere in the direction of the vector $\vec{S}_0$. In Figure 2.1 , $\vec{S}_o$ is the vector to the source centre, $\vec{S}$ is a vector in a slightly different direction to one particular part of the brightness distribution of the source, $\vec{\sigma}$ is the difference vector with $\vec{\sigma}=\vec{S}-\vec{S}_o$. The spatial coordinates x, y are measured in angular units (rad) and the spatial frequency coordinates u, v are measured in mega- wavelengths. In addition, the positive values of x (R.A.) and u are west on the sky, the positive values of y (decl.) and v are north on the sky. (For more information see Thompson et al. 1986 and also see Burke and Graham-Smith 1997).

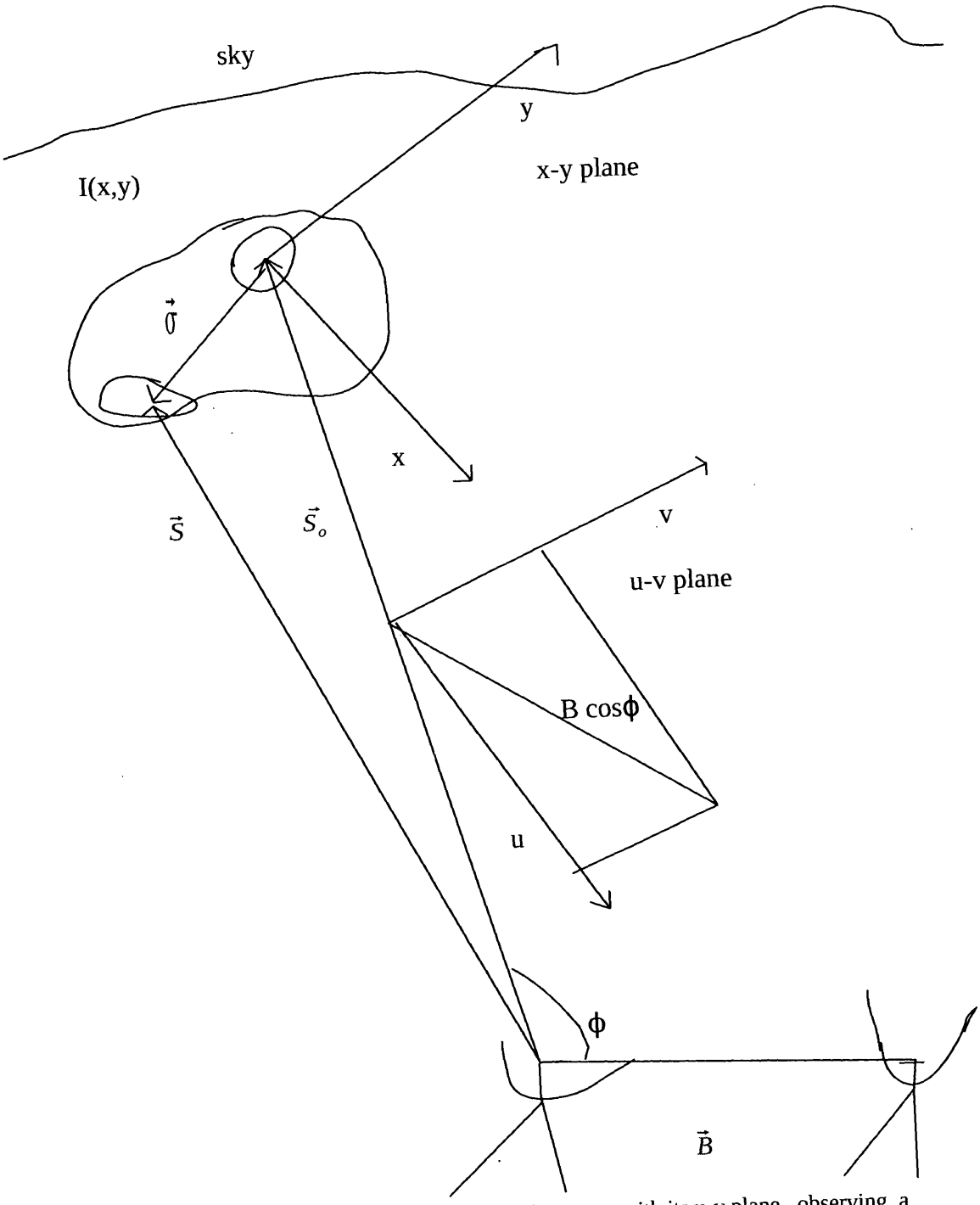

Figure 2.1. Geometric illustration of a two-element interferometer with its u-v plane, observing a source with a brightness distribution I(x, y). B cosϕ is the projection of $\vec{B}$ on the u-v plane. (see also Thompson et al. 1986)

2.1 The u- v coverage

For VLBI observations the u-v plane is never filled completely. Only for an antenna as large as the Earth itself would that be the case. Missing spacings in the u-v coverage imply a loss of Fourier components in the synthesized image. The resultant map will have sidelobes that are much larger and more complex than those generated by a filled aperture of such a large antenna. The sidelobes can be reduced by adding more antennas to an array and increasing the length of time of the observation and thus lengthening the u-v tracks. Also, the declination of the source has an impact on the u-v coverage. We show different u-v coverages for different declinations obtained with the same array, *VLBA*[1] , in Figure 2.2. For sources with a high declination, δ, δ= 64 deg for example, an excellent u-v coverage is obtained. For sources with lower declination, the u-v coverage becomes less extended north-south. For a declination of δ=18 deg, for example, the u-v coverage is much worse than for the highest declination in the figure. Due to the rotation of the Earth over the course of the time of the observations, the samples for a particular baseline trace out an almost elliptical path in the u-v plane. Also for the case of the VLBA, the u-v coverage is very good for the inner portion of the u-v plane.

---

1. The Very Long Baseline Array (VLBA) comprises ten radio telescopes spanning 5,351 miles. It is the world's most extend, dedicated telescope array.

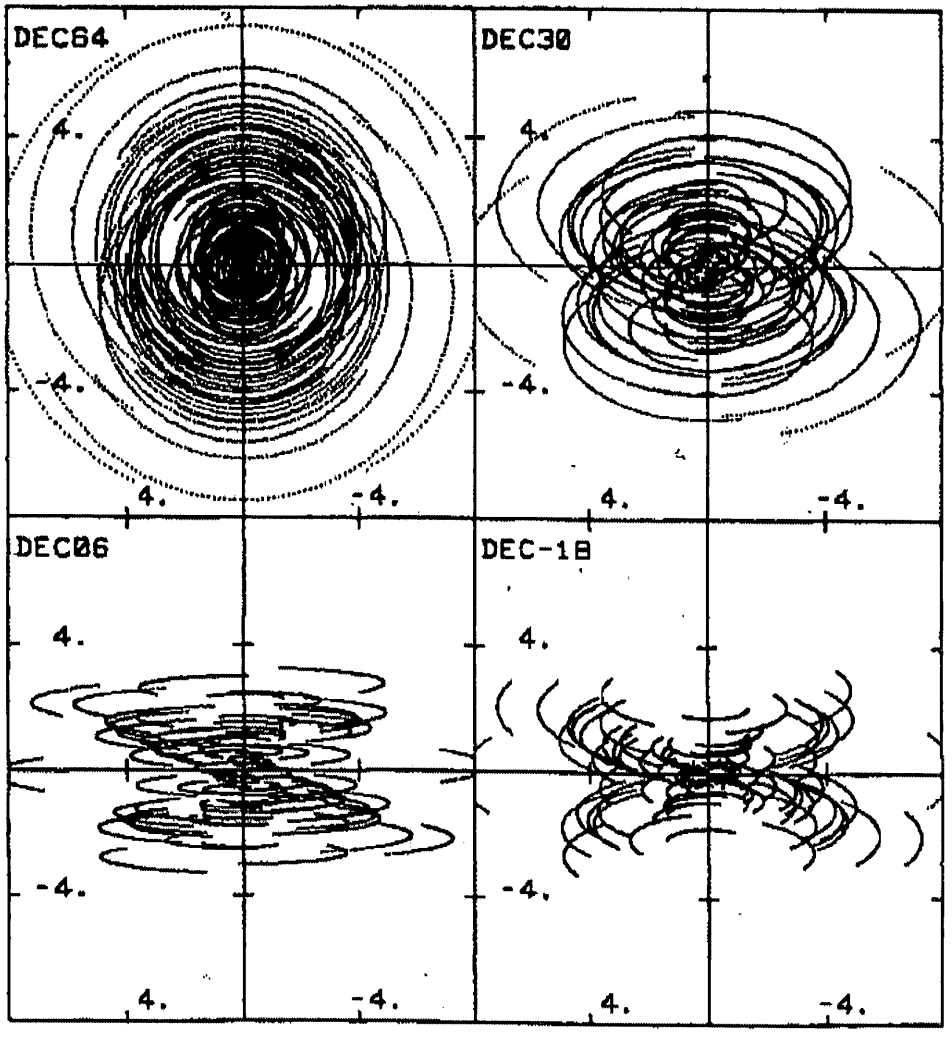

Figure 2.2 The u-v coverages as a function of the declination of the target sources for the 10-antenna VLBA. The declinations are given in the upper left corner for each panel. Arbitrary units only are given for both, u and v. The horizontal axis shows u and the vertical axis v. The Figure is taken from Thompson, et al. (1986).

2.2 Visibilities and the brightness distribution

Radio astronomers developed a method, called synthesis imaging, to use data measured by an interferometer array to make an image of an observed, celestial source. Such an image displays the brightness distribution of the source on the sky. All measurements by the interferometer array are related to the complex visibility function, V(u,v), as a function of u and v in the u-v plane. Figure 2.1 shows the geometrical relationship between the x-y sky plane and the u-v plane. The u-v plane is related via the Fourier transformation to the image plane. The complex visibility function, V(u,v), is the inverse Fourier transform of the observed source brightness distribution, I(x,y). Their relationship is given by,

$$V(u,v)=\int_{-\infty}^{+\infty}\int_{-\infty}^{+\infty} I(x,y)\,e^{2\pi i(ux+vy)}\,dxdy \qquad (2.1)$$

The brightness distribution of the source , I(x,y), can then be obtained as ;

$$I(x,y)=\int_{-\infty}^{+\infty}\int_{-\infty}^{+\infty} V(u,v)\,e^{-2\pi i(ux+vy)}\,dudv \qquad (2.2)$$

(see, Thompson et al. 1986)

To reconstruct the brightness distribution of an arbitrary source, an interferometer must

completely sample the visibility function. Obviously only one two-element interferometer observing for only one moment in time will produce only one sample of the visibility function in the u-v plane which is extremely bad u-v coverage for the observed source. In practice we use multiple interferometers, namely an array, observing for a long time to produce relatively good u-v coverage. The goal is to sample the visibility function at as many projected baseline lengths and orientations in the u-v plane as possible. So, in theory the best image, I (x, y), can be constructed if V(u, v) is known for each point in the u-v plane. However, in practice V(u, v) is known only for the points along the tracks in the u-v plane as shown in Figure 2.2. In an extreme case, namely in the case of only one interferometer producing just one track in the u-v plane that is generated by the changing projected baseline of the pair of antennas and its orientation, V(u, v) is sampled just along that track.

2.3 The dirty image and the dirty beam

Ideally, the visibility function, V(u, v), should be sampled by an interferometer array at each point in the u-v plane. One can make or construct an image for an observed radio source using equation 2.2. In practice, the visibility function is known only for sampled points along narrow tracks in the u-v plane. Then, the visibility function is given by

$$V_S(u,v)=S(u,v)V(u,v) \qquad (2.3)$$

where S(u, v) is the sampling function. The sampling function is a generalized function which can be expressed in terms of the 2-dimension. Dirac delta function as

$$S(u,v)=\sum_k W_k \delta(u-u_k)\delta(v-v_k) \qquad (2.4)$$

where W_k is the weight at point k and k is an index running from 1 to the number of the last observed data point. Fourier inverting equation 2.3 into the image plane using the convolution theorem gives us

$$\mathrm{I_d}(x,y)=B(x,y)*\mathrm{I}(x,y) \qquad (2.5)$$

where $\mathrm{I_d}(x,y)$ is the dirty image, B(x, y) is the point spread function (PSF) or beam pattern (dirty beam) of the interferometer array, and "*" denotes convolution. The beam pattern is obtained by Fourier transforming the sampling function given by Equation 2.4. To emphasize or de-emphasize different points of the u-v plane and in effect particular points of the visibility function or to control the shape of the beam pattern, different weighting functions are assigned to the visibility points in the u-v plane. The weighted, sampled visibility function is given by

$$V_w(u,v)=\sum_k W_k \delta(u-u_k,v-v_k)V(u_k,v_k) \qquad (2.6)$$

There are different choices of weighting functions, W_k, such as C, CS, and robustness

weighting with natural and uniform weighting as extremes. This weighting can be used to account for different noise variances in different samples, or to account for differences in the density of sampling in different parts of the u- v plane, or to improve the sensitivity to extended objects (Richard et al. 1985). Here we briefly review different weighting schemes used in this thesis.

2.4 Visibility data weighting

Visibility data weighting is a two-part process. First the visibilities are weighted by some function of their statistical uncertainty, σ. Then, the weights may be further modified according to the density of sampling in the u-v plane. For the first part, we can use C or CS weighting (see section 2.4.1 for a definition). For the second part we have the robustness factor, again, with natural and uniform weighting as extremes.

2.4.1 Weighting as a function of the rms noise

The visibility data can be weighted as a function of the rms noise of the data recorded at the telescopes of the array expressed by σ. In this thesis we use weighting in terms of $1/\sigma^2$ and $1/\sigma$, the first, for which the code C is used, and the second, for which the code CS is used, with "S" denoting the use of the square root. Both types of weighting have advantages and disadvantages. For a weak source where uncorrelated noise, represented by σ, dominates, C- weighting could essentially reduce the VLBI array to just the largest two antennas since they will produce visibilities with, by far, the smallest

σ. This is problematic for weak sources if they almost cannot be detected with interferometers with small antennas. Using CS- weighting produces a more even-weighted u-v coverage when the range in sigma is quite large due to the range of large and small telescopes. CS-weighting increases the weight of the visibilities of the smaller telescopes in comparison to the visibilities of the large telescopes and in effect makes better use of the u-v coverage. (Briggs, 1995). However, if the source is strong and the range of large and small telescopes is not that large, then C- weighting may be the more appropriate way to process the data.

2.4.2 Weighting by effectively modifying the density in the u-v plane

Another kind of weighting visibility data is given by effectively modifying the density of the visibility data in the u-v plane. We can use natural or uniform weighting depending on whether, for example for the u-v coverages in Fig. 2.2, more weight should be given to the inner portion or the outer portion of the u-v coverage, respectively.

Natural weighting means that no further modification of the weights beyond the C or CS-weighting is applied. If we have a dense inner part of the u-v coverage as in Fig. 2.2, then the natural weighting would emphasize the inner part of the u-v coverage. As a result, the size of the beam is then more determined by the inner part of the u-v coverage, i.e. then the beam would be rather large.

Uniform weighting means that the existing weights are reduced in areas of the u-v coverage where the density of the weights is high. For instance, in case of the u-v coverages in Figure 2.2 the density of the visibility data is high in the inner part of the u-v coverage. Uniform weighting in effect evens out the density of the visibility data across the u-v coverage.

Compromising between natural and uniform weighting is possible through the robustness factor (Briggs, 1995). These factors effectively range from -5 to + 5 and can be applied if "complex" weighting is chosen in AIPS. The factor -5 is equivalent to uniform weighting. The factor +5 gives a weighting similar to natural weighting. For the u-v coverages in Fig. 2.2, using negative values of robustness factors leads to images with a relatively small size of the beam which results in a high-resolution image. In contrast, using positive values of robustness factors makes images with a relatively large size of beam.

In Figure 2.3 we show the u-v coverage obtained from VLBI observations of SN 1993J. As described in section 2.1, this excellent u-v coverage was used in this thesis for our analysis. The u-v coverage is related to the beam pattern. The beam pattern, B(x, y), is the response of our instrument to a point source. The beam pattern is given as

$$B(x,y)=\int_{-\infty}^{+\infty}\int_{-\infty}^{+\infty} S(u,v)e^{2\pi i(ux+vy)}\,dudv \qquad (2.7)$$

It is also called the " dirty beam." In general the beam pattern has sidelobes, positive and negative ones . The sidelobes can be as large as the main lobe, for instance in the case of a two-element interferometer, but for VLBI observations with more than 10 antennas the sidelobes are usually ~ 20 % of the peak of the main lobe or smaller. Figure 2.3, right panel, shows a plot of the beam pattern obtained from the u-v coverage shown in the left panel. The central area shows the main lobe. The sidelobes are shown as circular ripples around the main lobe. The inner-most sidelobe is at 15%- 20% of the peak of the main lobe. More gaps in the u-v coverage would cause larger sidelobes in general. However, the weighting function , W_k, can influence the strength of the sidelobes. It can also influence the width of the main lobe.

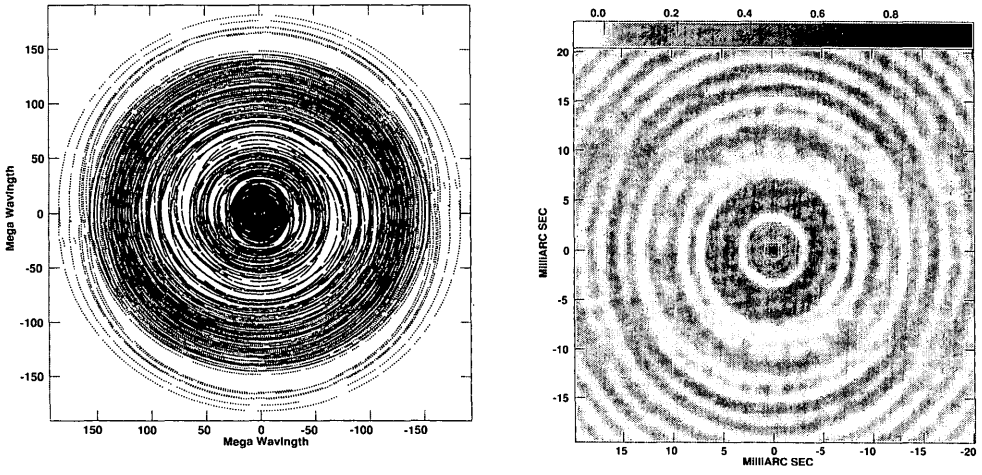

Figure 2.3 The u-v coverage (left panel) and beam pattern (right panel) for VLBI observations of SN 1993J on 2007 Nov. 3. For the left panel the horizontal axis is u and the vertical axis is v. Both, u and v are measured in mega wavelengths. The grey scale of the beam pattern is given in Jy/beam, normalized to unity.

According to equation 2.5, an image of a celestial source can be made by Fourier transforming the sampled visibility function, $V_s(u, v)$. Such an image is the dirty image namely, $I_d(x, y)$. Figure 2.4 shows the dirty image for SN 1993J using visibility data from VLBI observations. The dirty image does not show the true brightness distribution, I(x, y). As indicated in equation 2.5, the true brightness distribution, I(x, y), of the observed source is expressed through the convolution with the dirty beam, B(x, y). It needs to be extracted from the dirty image, $I_d(x, y)$. The dirty image given in Figure 2.4 was produced from the visibility data corresponding to the u-v coverage and the dirty beam shown in Figure 2.3. The dirty image has a central component and relatively large sidelobes as is seen in Figure 2.4.

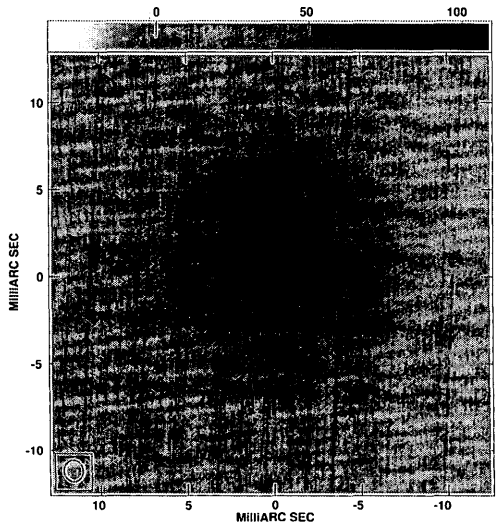

Figure. 2.4 An example of a dirty image of SN 1993J using VLBI observations on 2007 Nov. 3. The peak brightness is 88.0 μJy/beam. The background rms brightness of noise is 7.0 μJy/beam. The strongest side- lobes are at 67% of the peak of the central component.

Since the dirty image contains relatively large sidelobes, it does not show a good approximation of the true brightness distribution, I(x,y). $I_d(x, y)$ needs to be deconvolved to reduce or even remove the large sidelobes and to provide an image that is a better approximation of the brightness distribution . The most common image algorithm for VLBI imaging is CLEAN (Hogbom 1974), which was mentioned earlier. This is also the image algorithm we use in this thesis. In the following we will describe this algorithm and show how we can "clean" a dirty image to produce a clean image.

2.5 The CLEAN algorithm

In this section a clean image is produced from a dirty image. Because of the largely incomplete sampling of the visibility function in the u-v plane, the dirty image, $I_d(x, y)$, cannot be deconvolved directly. Instead assumptions need to be made about the true brightness distribution, I(x, y), and an iterative process is used to obtain a clean image, $I_c(x, y)$, that is a good representation of I(x, y). This process is called CLEAN. The assumptions or *a priori* constraints are:

1) The brightness distribution is assumed to be non-zero within a limited region of known shape and position on the sky.
2) The brightness distribution can be represented by a collection of point sources. In that way, each of the point sources displays a beam pattern weighted by the strength of the point source. The dirty image is then a collection of the point source responses.

The major task of obtaining a good representation of the true brightness distribution is then to reveal the collection of the point sources.

The steps in the interactive process to obtain a clean image namely, $I_c(x, y)$, that is a good representative of the true brightness distribution, I(x, y), are as follows:

1. Find the position and strength of the peak in the dirty image $I_d(x, y)$.
2. Subtract from the dirty image, at the position of the brightness peak, the dirty beam, $B_d(x, y)$, normalized to unity and then multiplied by the brightness of the peak and further multiplied by the loop gain γ which is always <1 and typically ~ 0.1. This way, one point source is subtracted for this iteration.
3. Record the position and magnitude of the point source subtracted.
4. Return to stage 1, unless any remaining peak is below some user-specified level.
5. Convolve the accumulated collection of point sources with a "clean" beam, usually an elliptical Gaussian fitted to the central lobe of the dirty beam. This is the clean image, $I_c(x, y)$.
6. Add the residuals of the dirty image from stage 1, to the image formed in stage 5, (see Rohlfs and Wilson, 1986).

An example of a clean image, $I_c(x, y)$, made in such a way with the residuals added is given in Figure 2.5. It is produced from the dirty image, $I_d(x, y)$, given in Figure 2.4 and the dirty beam, $B_d(x, y)$, given in Figure 2.3.

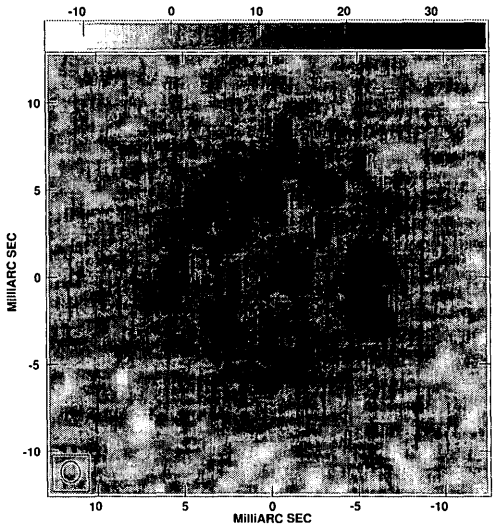

Figure 2.5 The deconvolved clean image of SN 1993J made using the CLEAN algorithm. Here and hereafter in all images, the grey scale at the top is given in μ Jy/beam and the full- width at half-maximum (FWHM) of the Gaussian fit to the inner portion of the dirty beam is given at the lower left. Also, North is up and East to the left.

It is apparent that the clean image, when compared with the dirty image, does not have the relatively large sidelobes anymore and is a much better representation of the true brightness distribution than the dirty image. We use the clean image for the purpose of the astrophysical interpretation of the imaged source, in the case of SN 1993J for the interpretation of the expanding radio shell and the interaction of the shock with the circumstellar medium (CSM). However, the CLEAN process is not ideal. This clean image is still subject to image errors. The main goal of this thesis is to find out how image errors can be reduced and the astrophysical interpretation of the VLBI images improved.

Chapter 3. Supernovae

3.1 General characteristics of supernovae

To familiarize the reader with the general characteristics of supernovae we give a brief description of this class of celestial objects with a particular focus on those aspects that are relevant for this thesis.

At this time, thousands of optical supernovae are known but only several dozen have been detected at radio wavelengths and only a portion of them studied with VLBI (see, e.g., Bartel and Bietenholz 2013). Supernovae are divided into two main groups : supernovae resulting from the detonation of white dwarfs and supernovae resulting from the core-collapse of massive stars. Supernovae resulting from the detonation of a white dwarf are known as Type Ia supernovae. This type of supernova is produced by runaway carbon fusion in a white dwarf in a close binary system. The spectrum of a Type Ia supernova does not show hydrogen or helium lines since hydrogen and helium escaped long ago before the progenitor became a white dwarf. Type Ia supernovae are used as "standard candles " for estimating the distances of distant galaxies. Through such distance measurements the acceleration of the universe was discovered and the existence of dark energy inferred. Supernovae resulting from the core-collapse of massive stars are known as Type Ib/c and Type II. All radio supernovae have massive stars as progenitors.

They are therefore of Type Ib/c or Type II. The spectra of Type Ib supernovae show He lines but those of Type Ic do not, and the spectra of Type Ib/c supernova do not show H lines too (Schlegel et al. 1996). The spectra of Type II show H and also He lines (e.g., Beswick 2006, and also see Zelik et al. 1992).

In all massive stars, shortly after the fusion of iron in the centre, the core collapses and forms a neutron star or a black hole. The surrounding material bounces back, and a shock wave is generated that travels to the outer layers of the star. When the shock wave breaks out through the surface of the star, the exploding star starts to brighten up enormously and becomes visible as a supernova. The gas of the exploding star expands outward. The shock wave expands further out into the CSM left over from the progenitor star. Figure 3.1 shows different parts of the supernova's structure and its surrounding area. It presents the photosphere, the neutral ejecta with the temperature of about 10^4 K, the ionized ejecta with the temperature of about 10^5 K, the reverse shock which expands into the ejecta, the shocked ejecta with a temperature of about 10^7 K, the contact surface where the ejecta hit the CSM and where Rayleigh-Taylor fingers can develop into the shocked CSM with a temperature of about $3x10^8$ K and the forward shock which expands into the CSM with a temperature of about $3x10^5 K$. Also, Figure 3.1 shows the outer and inner radii, namely θ_o, which is the expected location of the forward shock and θ_i, which is the expected location of the reverse shock. The forward and reverse shock fronts move in opposite directions indicated by arrows as seen from

the contact surface. For detailed information about different parts of the structure of a supernova see, e.g., Bartel et al. (2007).

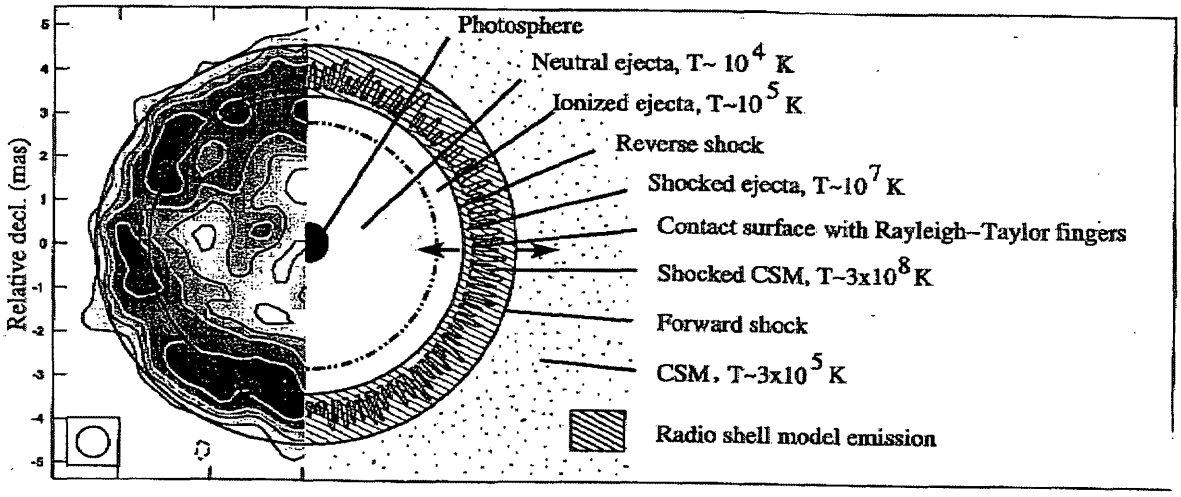

Figure 3.1 Half of the observed brightness distribution of SN 1993J (left side of panel) and a sketch of the characteristics of the ejecta interacting with the CSM. Figure taken from Bartel et al. (2007). For details in the Figure, see text. For the complete image of SN 1993J, see Figure 3.4.

3.2 Radio emission from core-collapse supernovae

The progenitor of a core-collapse supernova sheds mass from its surface at a rate typically about 10^{-4} to $10^{-5} M_{sun}\,yr^{-1}$, where, M_{sun} is the mass of the sun. This wind has a velocity of ~ 10 $km\,s^{-1}$ and fills the surroundings of the progenitor as the CSM for 1000's of years before the star explodes. After the shock front of the exploding star breaks through the surface of the star (shock break-out), the shock front interacts

with the CSM. This interaction generates a forward shock and a reverse shock as depicted in Figure 3.1. Radio synchrotron emission is expected from accelerated electrons in te magnetic field assumed to be generated between these two shock fronts. This radio emission region is indicated by dashed lines in Figure 3.1. Because of this interaction with the CSM, all supernovae originating from massive stars are expected to show shell morphology in the radio. Therefore, the radio brightness distribution would have the morphology of the 2D projection of a 3D shell. Radio radiation is expected to peak along a circle that coincides with the projection of the inner surface of the shell. This ridge emission is visible in Figure 3.1 in case of SN 1993J (left side of panel). In addition to the shell radio emission, the radio emission could also emanate from the centre of a radio supernova. Such emission could arise from a PWN or the environment of a black hole. Either of these remnants could be expected to be left over from the explosion of the progenitor star and reside in the centre of the supernova shell. Since the progenitor star of SN 1993J had a mass of about 25 M_{sun} (Höflich et al. 1993), we can expect a compact radio source in the centre of SN 1993J such as a PWN or an emission region associated with a black hole. In this study we also focus on the centre of SN 1993J to search for a compact source.

3.3 Radio lightcurves of supernovae

Determining the multi-frequency radio lightcurves of a supernova and the evolution of such lightcurves with time enables us to find out more about the density and the structure

of the CSM. The radio lightcurves give us information about the presupernova wind such as its clumpiness and filamentary nature and also the mass-loss rate, structure, stage in which the star passed on its way to exploding and possibly any companions. Figure 3.2 shows the lightcurves of SN 1993J that were obtained from observations at eight different frequencies. At the early stages of the expansion of the supernova most of the CSM is still surrounding the supernova in its original form. The CSM is ionized by the photons from the explosion and is optically thick to the radio radiation. The flux density is relatively low. As the supernova shock front expands, the radio radiation is increasingly less absorbed. The flux density increases. This increase can be seen in each of the plots in Figure 3.2.

After some time the swept-up CSM transitions from being optically thick to being optically thin to radio radiation. At that point the radio brightness reaches its maximum. After reaching the peak, the flux density decreases with time. The time at which the flux density reaches the peak is frequency dependent, being relatively early at high frequencies and occurring later in time at lower frequencies. The appearance of the supernova is expected to change. During the rise of the flux density the supernova is expected to have a disk-like structure (Marscher 1985) . Only the projected surface of the expanding shell can be seen. After the transition from being optically thick to being optically thin the projection of the 3D supernova starts to become visible and a shell is expected to develop when the CSM becomes completely optically thin. At that time the

supernova assumes a shell-like structure which can be resolved with VLBI in some cases and which can enable us to make a detailed image of the supernova and to extract astrophysical information from it.

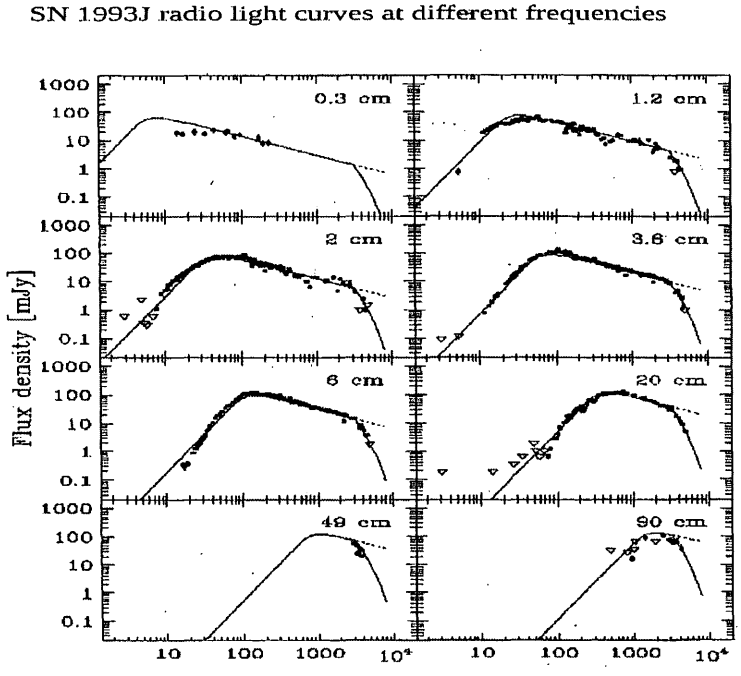

Figure 3.2 Radio lightcurves of SN 1993J at different wavelengths . The horizontal axis shows time after shock breakout in days. Figure is taken from Weiler et al. (2007).

3.4 VLBI observations of supernovae

For VLBI observations to be feasible the supernova has to be moderately bright, and for the observations to be worthwhile it has to be moderately close (otherwise we just see a

point-source). Several radio supernovae have been observed with VLBI, and high resolution images were obtained to reveal the supernova morphology and to study the evolution of the expanding supernova shell and the characteristics of the CSM. The radio radiation for some supernovae can be quite strong and detectable with radio antennas at several frequencies.

More than a dozen radio supernovae have been detected with VLBI, but only a few could be imaged in detail. Of these few SN 1979C (Bartel et al. 1985, 2003, 2008), SN1986J (Bartel et al. 1987) and SN1993J (Bartel et al. 2002, 2007, Bietenholz et al. 2002, 2010, Marcaide et al 2009, 2012, Marti-Vidal et al. 2011) are particularly well studied and a series of images of theses supernovae were made. These images gave us useful information about the angular size, the expansion and deceleration of the shell, and the history of the progenitor star. Also SN 1987A was imaged in detail. It is located in the Large Magellanic Cloud only 50 kpc away from Earth. Images were obtained with the Australian interferometer, ATCA, at different frequencies. (Manchester et al. 2002). Also VLBI observations of SN 1987A exist, both early on (Jauncey et al. 1988) and at late times (Tingay et al. 2009; Ng et al. 2011). As examples, we will discuss two supernovae recently observed with VLBI which show very different structures. These are SN1986J which has shell structure and a compact source in the projected centre and, SN 1993J, which has only shell structure.

3.4.1 SN 1986J

SN 1986J was the first optically identified supernova for which a detailed image was made (Bartel et al. 1991). VLBI observations of SN 1986J at a wavelength of 3.6 cm revealed a shell-like structure of this supernova. The ridge of the shell is heavily modulated in brightness. This strong modulation is likely due to the interaction of the shock front with the CSM left over from the progenitor star. In addition, a compact component was seen in the projected center of the expanding radio shell (see Figure 3.3). For detailed information, see Bietenholz et al. (2008). This compact component could be a very dense condensation in the shell facing the observer which by chance coincidence would be located in projection in the centre of the shell. It could also arise in the inner part of the shell as a result of a binary (Chevalier, 2012). It could also be a PWN or radiation from the environment of a black hole, in other words, radiation from the compact remnant of the explosion. Radiation from such a remnant is expected to become visible as soon as the shell becomes transparent to radiation from the interior. Two of these possibilities were discussed by Bietenholz et al. (2004). Recently, SN 2008 iz, was found to also show a compact component in the centre, but the component has faded below the detection threshold in the latest image (Brunthaler et al. 2010).

3.4.2 SN 1993J

Supernova 1993J is the supernova that has been studied most in the radio. This radio source has been observed with VLBI at different frequencies, and a wealth of information

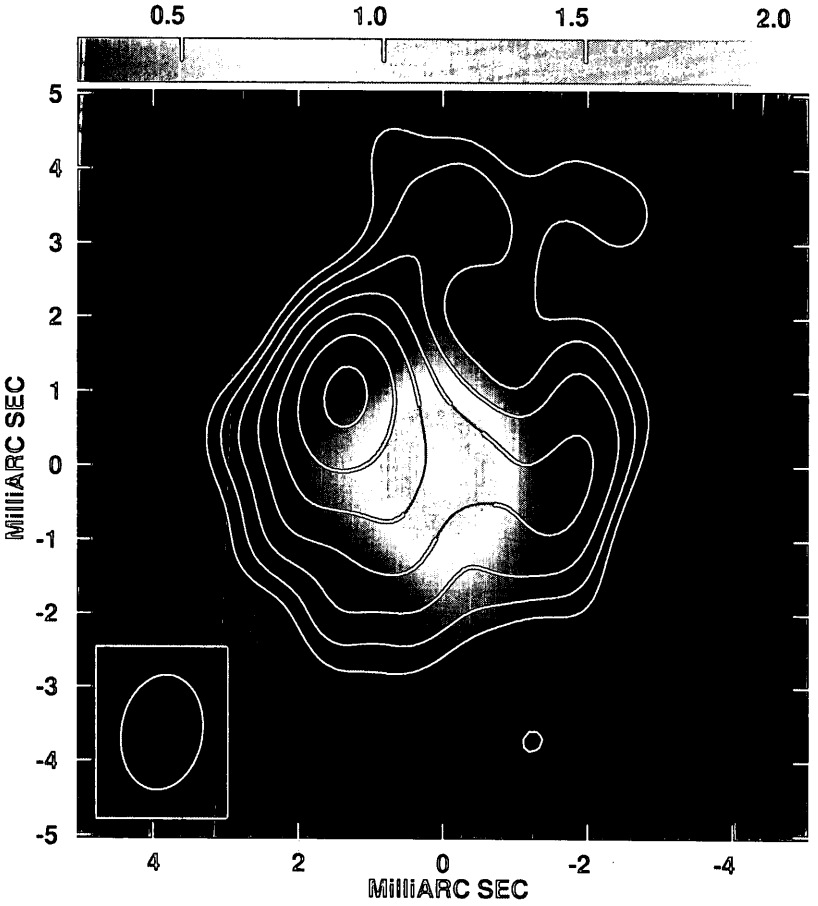

Figure 3.3 A composite VLBI image of SN 1986J at 5 and 15 GHz. The 5 GHz contour image shows radio emission from the shell. In contrast, the 15 GHz grey-tone image shows a compact component in the centre of SN 1986J. The 5.0 GHz observations were taken on 2002 Nov. 11 and the 15 GHz observations were taken on 2003 Jun. 22. The contours are drawn at 11.3, 16, 22.6, ..., 90.5% of the peak brightness of 2.04 mJy/beam for 5.0 GHz. The greyscale for the 15 GHz map is labeled at the top in mJy/beam. Figure taken from Bietenholz et al. (2004).

was obtained. Radio emission from SN 1993J was detected a few days after shock break-out (Pooly and Green 1993; Weiler et al. 1994; Phillips et al. 1993) and its peak at 8.4 GHz was ~ 120 mJy . In addition, the radio lightcurve of the supernova was modeled in

terms of the interaction of the expanding shell with the CSM (van Dyk et al. 1993). The size of the supernova was determined using VLBI by Bartel et al. (1993) and also Marcaide et al. (1993, 1994). These measurements led to calculating the angular expansion velocity (Bartel et al. 1994; Marcaide et al. 1995a). VLBI observations of SN 1993J showed a shell-like radio structure of this supernova 239 days after its explosion (Marcaide et al. 1995; Bartel et al. 1995).

Studies of the radio lightcurve and the spectral properties imply that SN 1993J is a Type IIb, a subclass of a Type II which characterizes a supernova with a low-mass hydrogen outer layer. The morphology of SN 1993J is close to what one would expect for an ideal shell. It is an almost pure spherically symmetric shell. The ridge appears to be somewhat modulated in brightness. To which degree some or all of these modulations are real and to which degree image errors play a role is not clearly known. In this thesis we investigate image errors in clean images made from simulated VLBI observations for symmetric and asymmetric spherical shell models as well as for a disk model of a supernova. It is expected that the ridge of the shell of a supernova is modulated in brightness. This modulation is expected since the CSM and/or the ejecta are expected to be asymmetric. But the question here is how asymmetric are they expected to be. In this thesis we investigate whether the modulations seen for SN 1993J are real, at least partly, or totally due to image errors.

3.4.3 Is there any compact source in the centre SN 1993J ?

One interesting task in this study is to search for any compact source that may exist in the centre of SN 1993J. The progenitor star of SN 1993J was a massive star, and the remnant, a neutron star with a pulsar wind nebula around it or a black hole is expected to exist in the centre of the shell. We used data from VLBI observations at epoch 2007 Nov. 3 for the analysis in this thesis when the supernova was 14 years old.

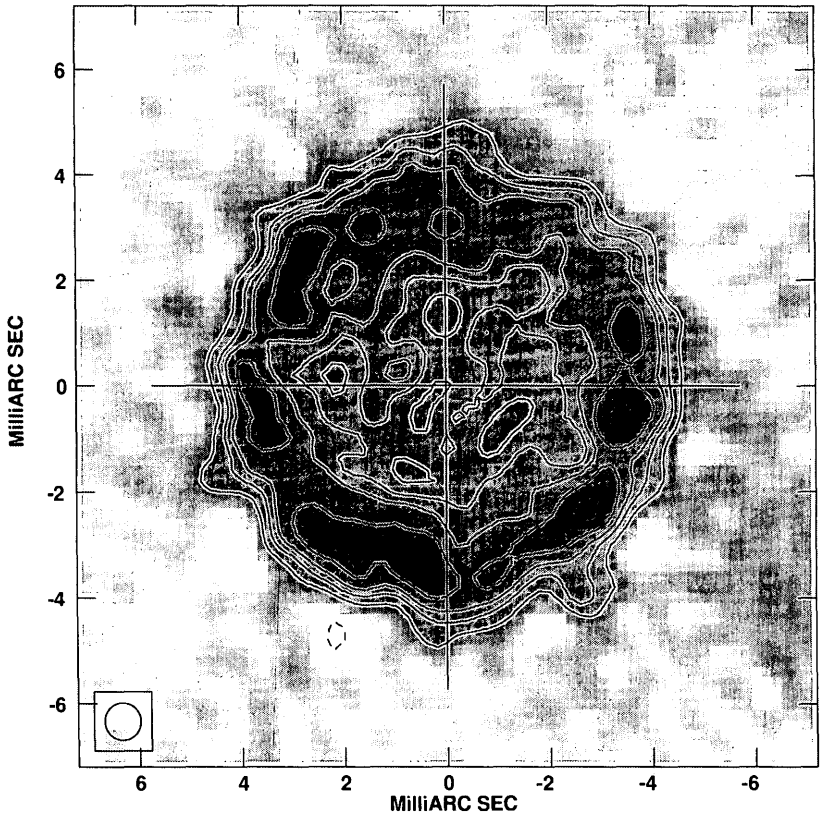

Figure 3.4 A composite image of SN 1993J at 8.4 GHz. Three separate VLBI data sets, at times, t=2080 , 2525 and 2787 d are combined to achieve a higher signal-to-noise ratio. The FWHM of the beam of this clean image is 0.7 mas. The contour levels are drawn at -16, 16, 32, 45.3, 46 and 90% of the peak brightness. Figure taken from Bietenholz et al. (2003).

Chapter 4 Models of Supernovae

This chapter provides a frame work for introducing different models of the brightness distribution of a supernova, namely a symmetric spherical shell model, an asymmetric spherical shell model and a disk model. Each model has its own characteristics and very generally the three models describe three different kinds of the brightness distribution of supernovae.

The introduced models of supernovae can therefore be used for the study of the interferometric VLBI images of supernovae in general and for SN 1993J in particular. All of the introduced models are free of image errors and are therefore ideal for simulation studies to investigate image errors that are generated through the imaging process. In the following we give for each of the three models the astrophysical justification and the description in detail.

4.1 The symmetric spherical shell model

The interaction of the shock wave with the CSM leads to the emission of radio radiation. This radiation is generated in a shell between the forward and reverse shocks. Thus, a

radio supernova usually has a shell-like structure, provided the supernova is optically-thin. If the interaction is isotropic then a symmetric spherical shell is expected for a supernova. For such a case, a symmetric spherical shell model is made to represent an image of an idealized supernova with shell-like structure.

The AIPS task IMMOD was used to make a 2D projection of a 3D symmetric spherical shell model so that the brightness distribution of a supernova as it would appear on the sky could be displayed. This model was then convolved with a CLEAN beam. Figure 4.1 (top panel) shows the brightness distribution of the sky projection of a symmetric spherical shell model with an outer angular diameter, $\theta_o = 15$ mas and inner angular diameter, $\theta_i = 12$ mas. The brightness has a minimum in the centre. With increasing radius the brightness increases and reaches a maximum along a circular ridge and then falls off sharply toward the edge of the shell. The highest brightness of the radio emission comes from the ridge of the radio shell. The total flux density of the symmetric spherical shell model is 1.6 mJy.

4.2 The asymmetric spherical shell model

The radio emission is emitted from the shock region of the supernova interacting with the CSM. If the CSM and/or the ejecta are not isotropic, then the radio emission would be expected to be influenced and, as a consequence, the brightness distribution of the supernova would become asymmetric. In case of SN 1993J, the geometry of the shell is

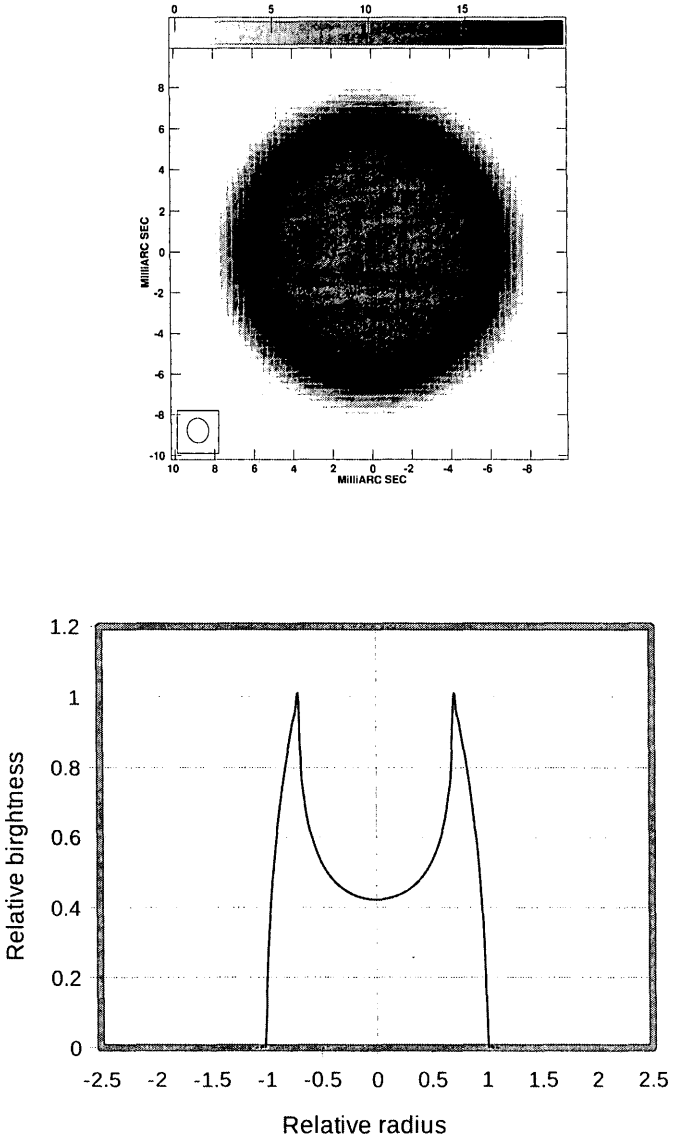

Figure 4.1 Top panel: The brightness distribution of the projection on the sky of a symmetric spherical shell model of a supernova with $\theta_o = 15.0$ mas and after convolution with the CLEAN beam displayed at the bottom left. The thickness of the shell is 3.0 mas so that $\theta_o/\theta_i = 1.25$, where θ_o is the angular diameter of the outer shell and θ_i is the angular diameter of the inner shell. The grey scale is labeled in μJy/beam. Bottom panel: Cross-section or brightness profile of the supernova. The vertical axis is the relative brightness. The radius scale of the profile is normalized to $\theta_o/2$ such that unity is equal to 7.5

mas in the upper panel. The radius scale is adjusted to the scale of the image in the top panel for easy comparison. The brightness scale is also normalized, such that unity is equal to the peak brightness. It should be pointed out that the profile in the lower part of this figure has not been convolved with the CLEAN beam. The total flux density of the symmetric spherical shell model is 1.6 mJy.

almost ideally circular, however the brightness along the ridge of the shell is modulated. This can be clearly seen in early images of SN 1993J (Bietenholz et al. 2008). In the early images the dynamic range is high, and the modulation is almost certainly real. In later images the dynamic range is much lower than in the early images and it is not clear whether the apparent modulation is real or not. The addition of a component on the ridge of the model makes, in a simple way, the brightness distribution asymmetric.

To calculate the brightness distribution of an asymmetric spherical shell model we used, as before, the 2D projection of a 3D spherical shell model, but now added a point source to the symmetric spherical shell model. We chose to have a point source on the ridge of the brightness distribution so as to model a strong component on the ridge which could be thought of as being produced by a condensation of the CSM or the ejecta. We used the AIPS task IMMOD to make an asymmetric spherical shell model of the brightness distribution of a supernova. The position of the point source along the ridge was arbitrarily selected to be on the western side. We do not think that the specific selection of the position of the point source would significantly influence our results. The point source was selected to have a flux density of 54.0 μJy so as to clearly dominate the

brightness along the ridge. Then the total flux density of the asymmetric spherical shell model is 1.654 mJy. This model serves as a specific case for the general investigation of how any asymmetry in the brightness distribution of a supernova affects the quality of the VLBI images.

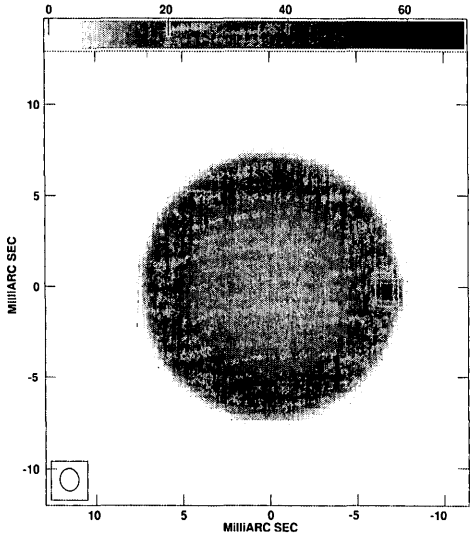

Figure 4.2 An asymmetric spherical shell model of a supernova. The models as in Figure 4.1 (top panel), but now with a brightness distribution that is not uniform along the ridge due to a point source having been added on the western side. The diameter of the asymmetric spherical shell model is 15.0 mas and the total flux density is about 1.654 mJy with 0.054 mJy from the point source.

4.3 The disk model

As a third model for this study, a disk model for the brightness distribution of a supernova is introduced. This model is used to investigate the early stages of a supernova expanding into the CSM, namely at a time when the supernova shell is still optically

thick. At a very early stage of the evolution the supernova is still optically thick and the shell structure cannot yet be observed. At this time only radiation emerges from close to the surface of the expanding supernova, and the supernova looks like a disk. In this case the brightness distribution is uniform over the entire surface of the disk.

The total flux density of the disk model is 1.6 mJy.

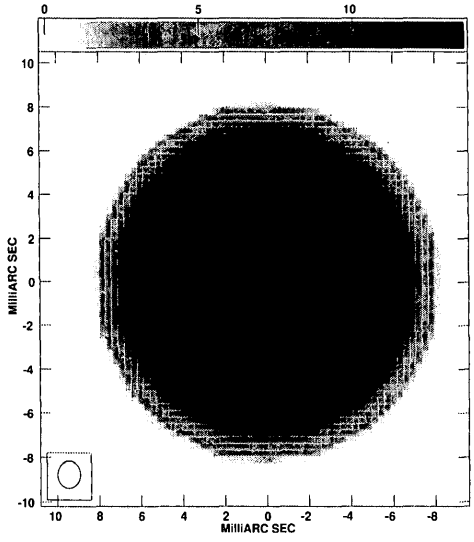

Figure 4.3 A disk model of the brightness distribution of a supernova. The disk is circular and the brightness distribution is uniform across the disk. The diameter of the disk is θ_o=15.0 mas with the total flux density of 1.6 mJy.

Chapter 5

Simulations of VLBI observations of model supernovae

In this Chapter we present an analysis of the simulation of VLBI observations of different brightness distributions of model supernovae, namely, of the symmetric spherical shell model, the asymmetric spherical shell model and the disk model. We vary the size, weighting scheme, robustness factor, number of clean components, value of gain and u-v coverage. These simulations were done to study the characteristics of image errors including systematic effects in VLBI images, how they are affected by the settings of parameters in the CLEAN algorithm and how the image errors in clean images made from simulated visibility data can be reduced. We note that a similar but less thorough analysis was done by Heywood et al. (2009).

5.1 Computing visibility data for the u-v coverage of the VLBI observations

In this study, we simulated one particular epoch of VLBI observations of SN 1993J taken on 2007 Nov. 3. For this purpose we recreated the u-v coverage from VLBI observations

of SN 1993J using the AIPS task UVMOD to compute visibility data for each model supernova. In effect, the observed visibility data were replaced for each point of the u-v coverage by the visibility data computed for the model supernovae.

5.2 Adding noise to simulated visibility data

In order to simulate the VLBI observations as closely as possible, we added thermal noise to the simulated visibility data set. The level of noise was taken so that the noise in the background radio emission region in the images was the same as the corresponding noise in the images from the VLBI observations. We therefore took the same set of visibility data and generated a large number, N, of sets of visibility data each with a different realization of noise added. To distinguish between the effects of noise and systematic errors, we generated a large number, N, with different realizations of the noise. We should point out that we put the noise realizations into different channels. We chose N=200. The value of $\sigma_{i,noise}$ for each specific channel "i" of noise realization with $1 \leqslant i \leqslant 10$ and N= 200 as examples is given in Table 5.1. Also $\sigma_{i,noise}$ is the image background rms. As can be seen there is a small difference from one channel to the other one, as expected. This large number of channels allows us to decrease the noise level by averaging. Since the noise we added is independent from one channel to the next, the average noise over all the channels should decrease as $(\bar{\sigma})_{noise} \propto 1/\sqrt{N}$. With N=200, $(\bar{\sigma})_{noise}$ should then decrease by a factor 14.1. This factor is large enough so that the $(\bar{\sigma})_{noise}$ for the averaged data is expected to be clearly smaller than the

deconvolution errors. We should point out here what we mean when we refer to a clean image. A clean image is an image with any one of 200 different realizations of noise. In other words, we can think of a 200-channel clean image as one image produced by the CLEAN algorithm in each of the 200 channels and each with a different realization of noise. We will specifically talk about the averaged clean image in section 5.5. There is a difference between the 200-channel clean image and the averaged clean image. Also we should note that throughout this and the following chapters, when we are talking about image errors we refer to errors due to noise and deconvolution errors. Further, to simplify reading, we will simply use σ_{noise} in the remainder of the thesis and clarify in the text what we mean by it.

Channel, i	$\sigma_{i,noise}$ (μ Jy/beam)
1	2.92
2	2.88
3	3.00
4	2.88
5	2.96
6	2.88
7	2.93
8	2.96
9	2.92
10	2.96
200	2.92

Table 5.1 The image background rms, $\sigma_{i,noise}$ in the selected example channels i, each with a different realization of noise.

5.3 Strategy for the simulations of VLBI observations of model supernovae

Through this study, VLBI observations of SN 1993J taken on 2007 Nov. 3 have been used for the simulation study. The simulation study was done in a systematic way in eight steps as described below. A summary of the simulation study is given in Table 5.2.

1. We first chose different models of the brightness distribution of a supernova, namely a symmetric spherical shell model, an asymmetric spherical shell model and a disk model. For each of these models we chose the same fixed parameters for the size, weighting scheme, robustness factor, clean components, gain and u-v coverage. The goal was to investigate image errors as a function of the brightness distribution of model supernovae. (see # 1-3 in Table 5.2).

2. We then chose one specific model, the symmetric spherical shell model, and varied the size of the shell, θ_o, to investigate image errors as a function of θ_o by leaving leaving the other parameters, the weighting scheme, robustness factor, clean components, gain and u-v coverage fixed. We selected three different sizes, 19.5, 15.0 and and 5.6 mas (see # 4 -6 in Table 5.2).

3. We then chose one specific model and one specific size, namely the symmetric spherical shell model with θ_o=15.0 mas, and varied the weighting scheme to investigate image errors as a function of the weighting scheme by leaving the remaining parameters, the robustness factor, clean components, gain and u-v coverage fixed. We then selected two different weighting schemes namely C and CS (see

7-8 in Table 5.2).

4. We then chose one specific model, one specific size and one specific weighting scheme, namely the symmetric spherical shell model with θ_o =15.0 mas, and weighting scheme C, and varied the robustness factor by leaving clean components, gain and the u-v coverage fixed. We selected 11 different robustness factors namely -5, -4, -3, -2, -1, 0, 1, 2, 3, 4, 5, to investigate image errors as a function of robustness factor (see lines # 9 -10 in Table 5.2). Robust weighting allows the weighting varying smoothly from uniform weighting to natural weighting. Again, a robustness factor of -5 corresponds to uniform weighting, while one of +5 corresponds to natural weighting.

5. We then chose one specific model, one specific size and one specific weighting scheme, namely the symmetric spherical shell model with θ_o =15.0 mas, and weighting scheme CS, and varied the robustness factor, by leaving clean components, gain and the u-v coverage fixed. We selected 11 different robustness factors namely -5, -4, -3, -2, -1, 0, 1, 2, 3, 4, 5, to investigate image errors as a function of robustness factor (see lines # 11 -12 in Table 5.2).

6. We then chose one specific model, one specific size, one specific weighting scheme and one particular robustness factor, namely the symmetric spherical shell model with θ_o=15.0 mas, weighting scheme C and robustness factor 0, and we varied the

number of clean components by leaving the gain and u-v coverage fixed. We selected four different values of 2000, 4000, 10000 and 20000 for the number of clean components to investigate image errors as a function of clean components (see lines # 13-16 in Table 5.2).

7. We then chose one specific model, one specific size, one specific weighting scheme, one particular robustness factor, and one particular number of clean components, namely the symmetric spherical shell model with $\theta_o = 15.0$ mas, weighting scheme C and robustness factor 0, clean components 20000, and we varied the value of the gain to investigate image errors as a function of gain by leaving the u-v coverage fixed. We selected three different values of gain, namely 0.02, 0.05 and 0.08 (see # 17-19 in Table 5.2).

8. We then chose one specific model, one specific size, one specific weighting scheme, one particular robustness factor, one particular number of clean components, and one specific value of gain, namely the symmetric spherical shell model with $\theta_o = 15.0$ mas, weighting scheme C and robustness factor 0, clean components 20000, and gain 0.08 and we varied the u-v coverage to investigate image errors as a function of u-v coverage.

   We selected two different u-v coverages, namely the full and the reduced one (see # 20-21 in Table 5.2). The reduced u-v coverage was produced by eliminating all baselines to the VLA. We chose to eliminate the VLA as it is the most sensitive telescope

in the array, and thus its elimination is expected to have the largest effect on the image quality and a difference from the case with the full u-v coverage is expected to be best visible.

5.4 Simulation of VLBI observations for model supernovae

In this section we will present our simulations for different model supernovae that have been made through the simulation study. For this purpose the simulated visibility data with the u-v coverage of the VLBI observations of SN 1993J taken on 2007 Nov. 3 were used to make clean images. We will present our results following the order of the eight steps of the strategy described in the previous subsections.

We first investigated image errors as a function of the supernova model (see lines # 1 to 3 in Table 5.2). We made clean images for the symmetric spherical shell, asymmetric spherical shell and disk model, and the other parameters were left constant, namely θ_o=15.0 mas, weighting scheme C, robustness factor 0, clean components 20000, gain 0.08 and u-v coverage full. Figure 5.1 shows the clean images for these three model supernovae.

Table 5.2 Scheme of the strategy for the simulation study

Model of supernova	θ_o (mas)	Weighting scheme	Robustness factor	# of clean components	Gain	u-v coverage	#
Symmetric	15.0	C	0	20000	0.08	full	1
Asymmetric	15.0	C	0	20000	0.08	full	2
Disk	15.0	C	0	20000	0.08	full	3
Symmetry	19.5	C	0	20000	0.08	full	4
Symmetry	15.0	C	0	20000	0.08	full	5
Symmetry	5.6	C	0	20000	0.08	full	6
Symmetric	15.0	C	0	20000	0.08	full	7
Symmetric	15.0	CS	0	20000	0.08	full	8
Symmetric	15.0	C	-5, -4, -3,-2, -1	20000	0.08	full	9
Symmetric	15.0	C	0,1, 2, 3, 4, 5	20000	0.08	full	10
Symmetric	15.0	CS	-5, -4,-3, -2, -1	20000	0.08	full	11
Symmetric	15.0	CS	0, 1, 2, 3,4, 5	20000	0.08	full	12
Symmetric	15.0	C	0	2000	0.08	full	13
Symmetric	15.0	C	0	4000	0.08	full	14
Symmetric	15.0	C	0	10000	0.08	full	15
Symmetric	15.0	C	0	20000	0.08	full	16
Symmetric	15.0	C	0	20000	0.02	full	17
Symmetric	15.0	C	0	20000	0.05	full	18
Symmetric	15.0	C	0	20000	0.08	full	19
Symmetric	15.0	C	0	20000	0.08	full	20
Symmetric	15.0	C	0	20000	0.08	reduced	21

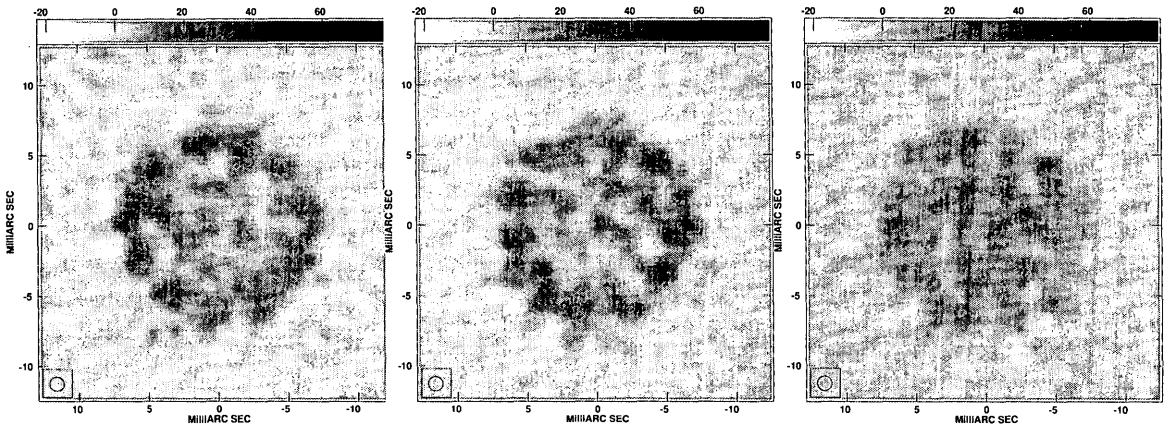

Figure 5.1 Clean images made from simulated VLBI observations of the three different model supernovae. The left panel displays the clean image for the symmetric spherical shell model, the middle panel for the asymmetric spherical shell model and the right panel for the disk model. The other parameters were left constant, namely θ_o=15.0 mas, weighting scheme C, robustness factor 0, clean components 20000, gain 0.08 and full u-v coverage. Again, here and hereafter for each panel, the grey scale is given at the top of the panel in μJy/beam and the CLEAN beam at the lower left corner. The grey scale was chosen to be the same for all images, and its maximum is given by the peak brightness of the point source in the asymmetric spherical shell model.

The differences between these clean images and the images of the perfect models as shown in Chapter 4 are image errors in the clean images. The image errors are the cause for the decreased quality and the modulation of the brightness in the clean images. In contrast, the images from the perfect model are smooth and do not have these variations. Nevertheless, the structure of the shell is clearly visible in the images displayed in the left and the middle panels. The point source is also clearly visible in the image in the middle panel.

Second we investigated image errors as a function of θ_o (see lines # 4 to 6 in Table 5.2). We made clean images for three different values of θ_o , namely 19.5, 15.0 and 5.6 mas and the other parameters were left constant, namely as the symmetric spherical shell model, weighting scheme C, robustness factor 0, clean components 20000, gain 0.08 and u-v coverage, full. Figure 5.2 shows clean images for θ_o=19.5, 15.0 and 5.6 mas.

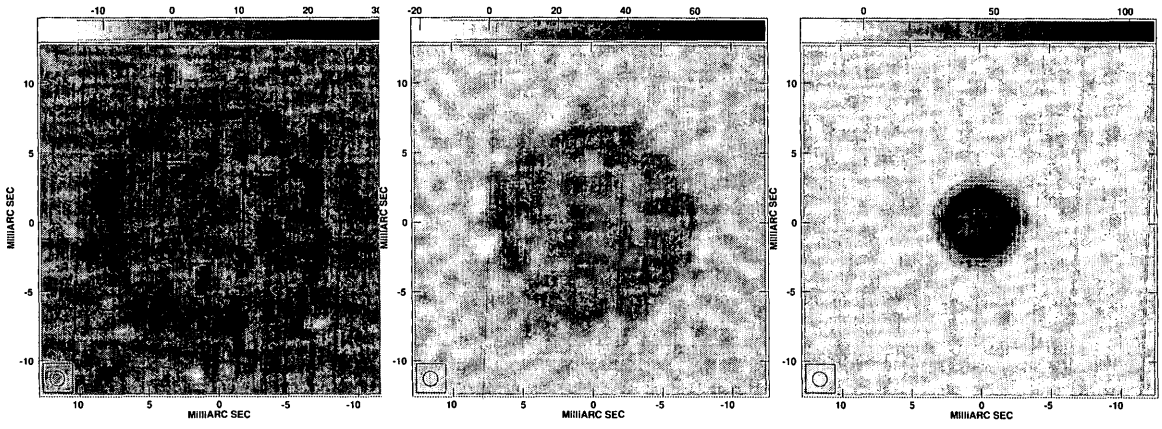

Figure 5.2 Clean images made from simulated VLBI observations of the symmetric spherical shell model for different values of θ_o . The left panel displays the clean image for θ_o=19.5 mas, the middle panel for θ_o=15.0 mas and the right panel for θ_o=5.6 mas. For further description see caption of Figure 5.1.

With decreasing θ_o, the peak brightness in the clean image goes up. This is because we chose the same total flux density for each model. It is also apparent that the clumpiness decreases with decreasing θ_o indicating that image errors are smaller for smaller values of θ_o while the beam size remains constant. The structure of the shell is clearly visible in each of the clean images but best in the right panel.

Third we investigated image errors as a function of the weighting scheme (see lines # 7 and 8 in Table 5.2). We made clean images for two different weighting schemes C and CS and the other parameters were left constant, namely as the symmetric spherical shell shell model with $\theta_o = 15$ mas, robustness factor 0, clean components 20000, gain 0.08 and u-v coverage, full. We show the corresponding clean images in Figure 5.3.

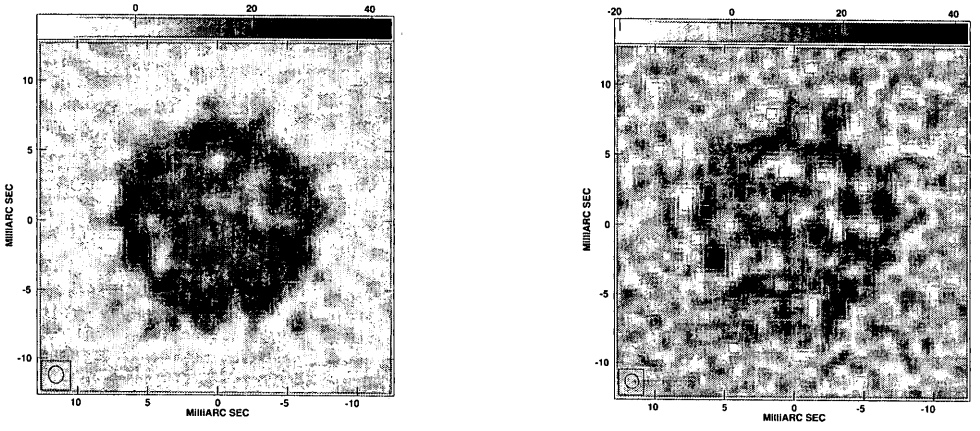

Figure 5.3 Clean images of the symmetric spherical shell model with $\theta_o = 15.0$ mas made for different weighting schemes. The left panel displays the clean image made using weighting scheme C and the right panel displays the clean image made using weighting scheme CS. The other parameters are left constant, namely as robustness factor 0, clean components 20000, gain 0.08 and u-v coverage, full.

In the clean images presented in Figure 5.3 the shell structure is again clearly visible but there is apparent intensity modulation around the ridge of the shell. It is also apparent that the "clumpiness" is more pronounced in the image produced with weighting scheme CS. This means that for a source like SN 1993J at a late epoch the image errors are larger if the weighting scheme CS is used.

Fourth, we investigated image errors as a function of robustness factor (see lines # 9 and 10 in Table 5.2). We made clean images for different robustness factors ranging from -5 to +5, and the other parameters were left constant, namely as the symmetric spherical shell model with θ_o=15 mas, weighting scheme C, robustness factor 0, clean components 20000, gain 0.08 and full u-v coverage. Then we made 11 different clean images corresponding to 11 different robustness factors. Each clean image has its own characteristics. Figure 5.4 shows three of the clean images, for robustness factors, -5, 0 and +5.

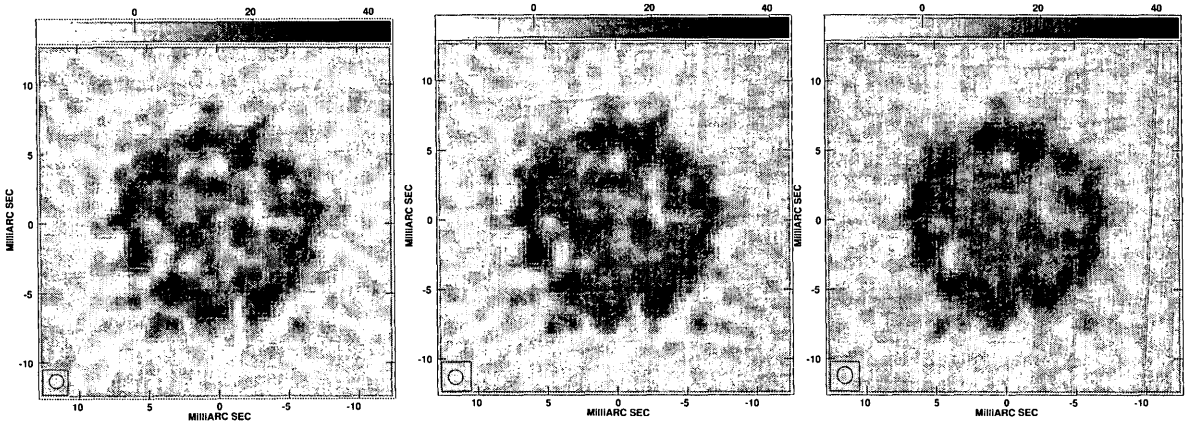

Figure 5.4 Clean images made from simulated VLBI observations for the symmetric spherical shell model with θ_o=15 mas and weighting scheme C, clean components 20000, gain 0.08 and full u-v coverage for different robustness factors . The left panel displays the clean image for robustness factor -5, (uniform weighting) the middle one displays the clean image made from robustness factor 0 and the right panel displays the clean image for robustness factor 5 (natural weighting).

As again can be seen from all the clean images, the shell structure is clearly visible and clumpiness is again apparent. Differences between the robustness factors -5 and 0 are not easily visible from the images, and may only be revealed clearly in the quantification

analysis described in later chapters. But it can be seen that the right panel has the largest beam, although only marginally so, and that the image looks slightly smoother than the others.

Fifth, we investigated image errors as a function of robustness factor (see lines # 11 and 12 in Table 5.2). We made clean images for different robustness factors ranging from -5 to +5, and the other parameters were left constant, namely as the symmetric spherical shell model with θ_o=15 mas, weighting scheme CS, robustness factor 0, clean components 20000, gain 0.08 and full u-v coverage. Then we made 11 different clean images corresponding to 11 different robustness factors. Each clean image has its own characteristics. Figure 5.5 shows three of the clean images, for robustness factors, -5, 0 and +5.

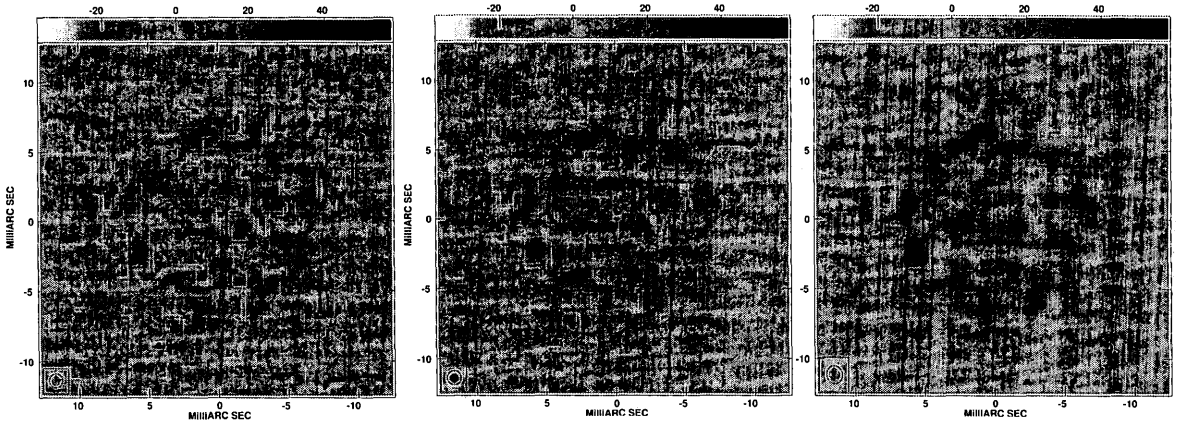

Figure 5.5 Clean images made from simulated VLBI observations for the symmetric spherical shell model with θ_o=15 mas and weighting scheme CS, clean components 20000, gain 0.08 and full u-v coverage for different robustness factors . The left panel displays the clean image for robustness factor -5, (uniform weighting) the middle one displays the clean image made from robustness factor 0 and the right panel displays the clean image for robustness factor 5 (natural weighting).

As again can be seen from all the clean images, the shell structure is clearly visible and clumpiness is again apparent. Differences between the robustness factors -5 and 0 are not easily visible from the images, and may only be revealed clearly in the quantification analysis described in later chapters. But it can be seen that the right panel has the largest beam, although only marginally so, and that the image looks slightly smoother than the others. It is interesting to point out that all three clean images show two pronounced components around the ridge of the shell due to the effect of noise.

Sixth, we investigated image errors as a function of clean components (see line # 13, 14 15 and 16 in Table 5.2). We made clean images for four different numbers of clean components namely 2000, 4000, 10000, 20000 and the other parameters were left constant, namely as the symmetric spherical shell model with $\theta_o = 15$ mas, weighing scheme C, robustness factor 0, gain 0.08 and full u-v coverage.

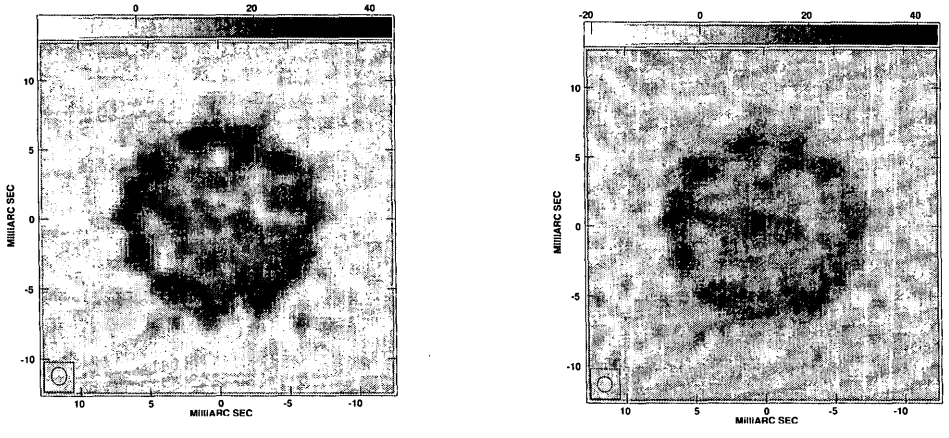

Figure 5.6 Clean images of the symmetric spherical shell model with $\theta_o = 15.0$ mas made for different numbers of clean components. The left panel displays the clean image made using 20000 and the right panel displays the clean image made using 4000 clean components. The other parameters are left costant, namely as weighting scheme C, robustness factor 0, gain 0.08 and u-v coverage, full.

As can be seen from Figure 5.6 the clean image made using 4000 clean components has more brightness variation in the inner part than the clean image made from 20000 clean components. In particular it has an apparently more pronounced central component than what is visible in the clean image using 20000 clean components. In Chapter 6 we will investigate the effect of clean components in detail.

Seventh, we investigated image errors as a function of gain (see line # 17, 18, 19 in Table 5.2). We made clean images for different values of gain namely, 0.02, 0.05, 0.08 and the other parameters were left constant, namely as the symmetric spherical shell model with size of θ_o=15 mas, weighing scheme C, robustness factor 0, clean components 20000 and full u-v coverage. We display two clean images made from gains 0.08 and 0.02 in Figure 5.7

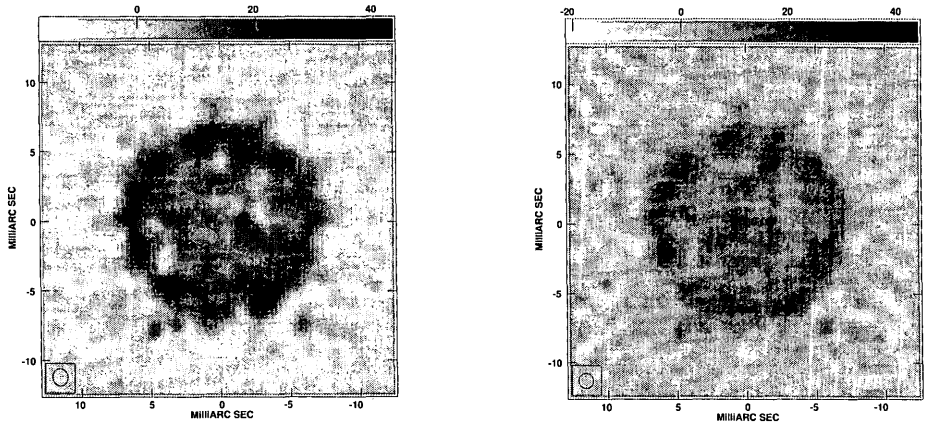

Figure 5.7 Clean images of the symmetric spherical shell model with θ_o=15.0 mas made for different values of gain. The left panel displays the clean image made using 0.08 and the right panel displays the clean image made using 0.02 for gain. The other parameters are left constant, namely as weighting scheme C, robustness factor 0, clean components 20000 and u-v coverage, full.

As can be seen from Figure 5.7 the clean image made using 0.02 for gain has an apparently rather bright component in the centre that is not that clearly visible in the clean image made from 0.08 for gain. In Chapter 6 we will investigate the effect of clean components in detail.

Eighth, we investigated image errors as a function of the u-v coverage (see lines # 20 and 21 in Table 5.2). We removed all visibility measurements associated with the VLA from the full u-v coverage from VLBI observations of SN 1993J to obtain a reduced u-v coverage. We made a clean image for the reduced u-v coverage, and the other parameters were left constant, namely we chose the symmetric spherical shell model with θ_o=15 mas for weighting scheme C and robustness factor 0, clean components 20000, gain 0.08. We display two clean images made from the full and the reduced u-v coverage in Figure 5.8.

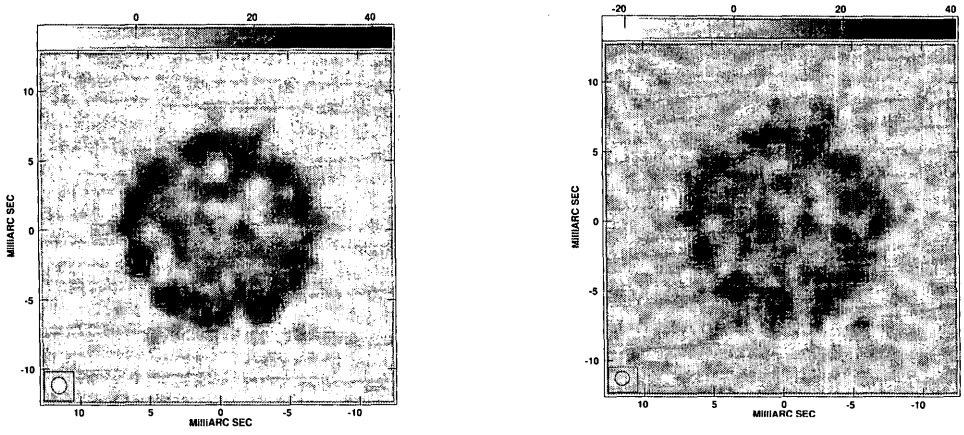

Figure 5.8 Clean images from simulated VLBI observations for the symmetric spherical shell model of a supernova for θ_0=15.0 mas, weighting scheme C, robustness factor 0, clean components 20000, gain 0.08 for different u-v coverages. The left panel displays the clean image made from the full u-v coverage and the right panel displays the clean image made from the reduced u-v coverage.

As can be seen from comparing the two images it appears, as expected, that the clumpiness is larger in the clean image made from the reduced u-v coverage (right panel) .

5.5 The Channel-averaged clean images

To investigate the systematic effects in clean images, we averaged 200 different channels, or noise-realizations. We made the channel-averaged clean images using the AIPS task SQASH. This averaging is expected to reduce the random noise by a factor of ~14 so that any systematic effects will be more apparent. Figure 5.6 presents three of the channel-average clean images for three different robustness factors, namely -5, 0 and 5.

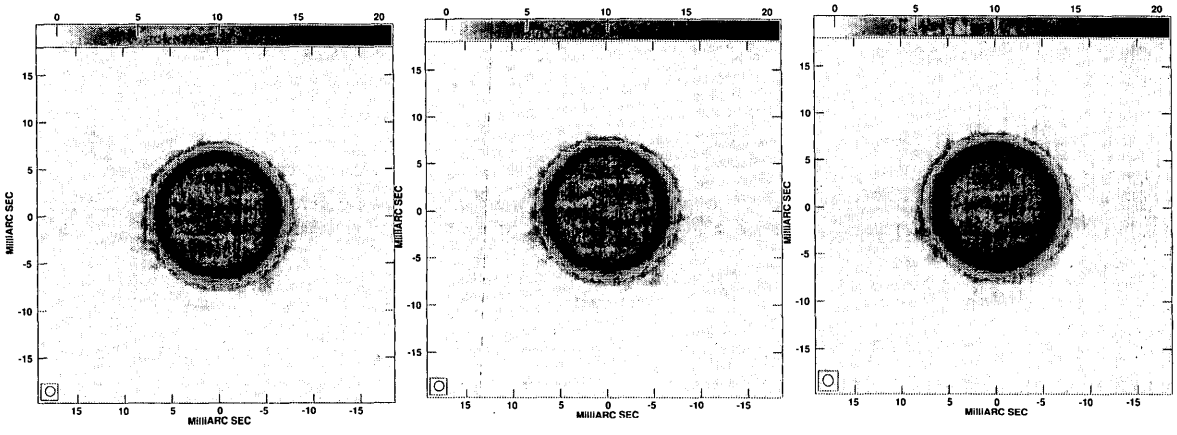

Figure 5.9 Channel-averaged images from simulated VLBI observations for the symmetric spherical shell model for θ_o=15 mas, weighting scheme C, for three different robustness factors, clean components 20000, gain 0.08 and full u-v coverage. Left panel displays the channel-averaged image made with the robustness factor -5, the middle panel shows the channel-averaged image made with robustness factor 0 and the right panel shows the channel-averaged image made with robustness factor 5. The grey-scale was chosen to be the same for all three images, for easier comparison.

As can be seen from all the channel-averaged images, the shell structure is much clearer than in the images in Figure 5.4. Clearly, the noise contribution to the image errors is much smaller. Differences between the robustness factor -5 and 0 are not easily visible from the images, and, again, may only be revealed in the quantitative analysis described in a later chapter. However, it is clear that the image made from robustness factor +5 has a slightly larger convolving beam resulting in a smaller angular resolution, smaller background noise rms and larger brightness values. We are going to quantify image errors in clean images made from simulated visibility data in Chapter 6.

Chapter 6

Image errors in clean images from simulated VLBI observations of model supernovae

This chapter will focus on estimating image errors which include errors due to noise in clean images and deconvolution errors due to incomplete u-v sampling. All clean images are susceptible to these errors. Furthermore, we will describe the procedure of estimating the image errors in clean images. We first discuss the quantification of image errors in clean images. Then we study the image errors as a function of different parameters. In particular we are interested in a qualitative visual assessment of image errors as well as a quantitative assessment of the image errors by computing statistical values. We then study image errors as a function of the 1) noise level of the simulated visibility data, 2) model supernova, 3) outer angular diameter, 4) weighting scheme, 5) robustness factor, 6) number of clean components, 7) value of the gain and 8) u-v coverage. The main strategy is to make an image of a model supernova, a clean image from the simulated data and a difference image from the two former images. This difference image shows image errors directly.

6.1 The quantification of image errors in clean images

We measure the background rms noise in clean images made from simulated VLBI

observations. In practice we run the AIPS task IMSTAT over the region of the clean image that appears to be free of radio emission. We measure the rms about the mean of the brightness distribution for such an empty region of radio emission. It should be pointed out that through this study the same region was chosen to estimate the rms noise for each clean image as it is shown in Figure 6.1.

For the quantification of image errors in a clean image we use the background in the clean images and also use the difference image. The difference between the clean image made from simulated VLBI observations for a model supernova and an image of the same model is what we call the "difference image." The difference image enables us to estimate image errors in the clean image. For this purpose we use the AIPS task COMB to obtain the difference image which is obtained from subtracting the model image from the clean image. The image errors in the clean images were measured by computing the rms brightness of the difference image. We note that the rms was computed over all 200 channels. The rms is the standard deviation of the mean in the clean box of the difference image. We subtract the brightness of each pixel in the model image from the brightness of each pixel in the clean image. We define the rms of the difference image as

$$rms_{diff} = \frac{\sqrt{\left(d_1^2 + d_2^2 + .. + d_M^2\right)}}{M} \qquad (6.1)$$

where d_i shows the brightness of pixel # i in the difference image where 1<i<M and

M is the number of pixels in the clean box. We are now determining the image errors in the clean images made from simulations of VLBI observations by computing the rms_{diff} along the path described in this section.

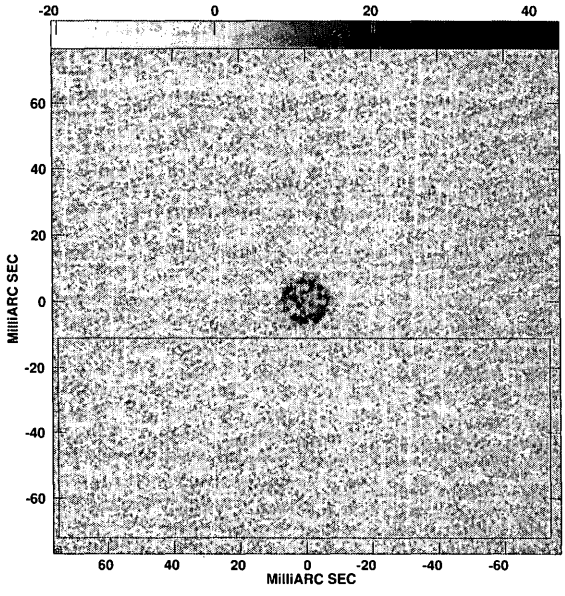

Figure 6.1 An example channel with one noise realization from a clean image made from simulated VLBI observations. The rectangular box is the region where we estimate the rms brightness of the noise. This region is free of radio emission. The clean box is shown at the middle of this image which is slightly larger than the size of the supernova so that covers the supernova fully. This is the area where we estimate rms_{diff} in the difference image.

6.2 Image errors in the clean images as a function of different parameters

In this section we investigate image errors in clean images by using our computations of the rms of the brightness noise of the background in clean images namely σ_{noise}, as well as rms_{diff} of the difference images to quantify image errors. We investigate errors

as a function of 1) different realizations of noise and 2) different noise levels 3) model supernova, 4) θ_o, 5) weighting scheme, 6) robustness factor, 7) clean components 8) gain and, 9) u-v coverage.

6.2.1 Image errors in clean images for different noise realizations

This section shows the results of estimating image errors in clean images as a function of different noise realizations by keeping the other parameters, namely, the model (symmetric spherical shell model), θ_o, the weighting scheme, the robustness factor, clean components, gain and the u-v coverage fixed. For the best comparison and ease of understanding, first the brightness distribution of the model supernova, second the clean image and third the difference image for the three different noise realizations are presented in Figure 6.2. Here and hereafter the left panel represents the model image, the middle panel the clean image made from the simulated VLBI observations and the right panel the difference image computed from subtracting the model image from the clean image. It can already be seen in the difference images that the residual brightness variations are larger in the area of the model supernova than in the background. Clearly image errors are larger than what is given by σ_{noise} alone.

We summarize the results from estimating image errors as a function of different noise realizations in Table 6.1. Here and hereafter in similar tables we list a number of parameters important for evaluating the quality of the images. We list the maximum

brightness in the clean image, B_{max} . Then we list σ_{noise}, which is the rms brightness of the background noise of the clean image where there is no radio emission. Again, the same region was chosen for all clean images. Then we list rms_{diff} which shows image errors of the clean images made from the simulated VLBI observations. Then we list the ratio of rms_{diff} to σ_{noise} . This ratio will be used later to determine the image errors in the clean image of SN 1993J where we use real visibility data as will be described in Chapter 7. We also give σ_{rel} which is the ratio of rms_{diff} to the peak brightness, namely rms_{diff}/B_{max}, which can be used to judge which images have smaller relative errors. Finally we list the full-width at half -maximum, FWHM, and the position angle, p.a., of the elliptical Gaussian clean beam.

As is seen from Table 6.1, the peaks of the brightness for all three clean images are the same as we expected because the total of flux density for all images is 1.6 mJy and also the size of the beam is the same. The values of σ_{noise} for the images are slightly different as are the values of the image errors namely, rms_{diff}. Here we want to clarify for the reader that we estimated the value of the rms_{diff} over only one channel for each of the three clean images, whereas in general we will estimate rms_{diff} over 200 channels. The most important result is indicated by $rms_{diff}/\sigma_{noise}$. This ratio is always larger than 1. That means the values of rms_{diff} are larger than the rms brightness of background noise. Also the values of σ_{rel} imply that all images have almost the same quality, as expected. Note that each of these parameters, rms_{diff} , $rms_{diff}/\sigma_{noise}$ and σ_{rel} charac-

terize image errors. From here on when appropriate we will mention which kind of image

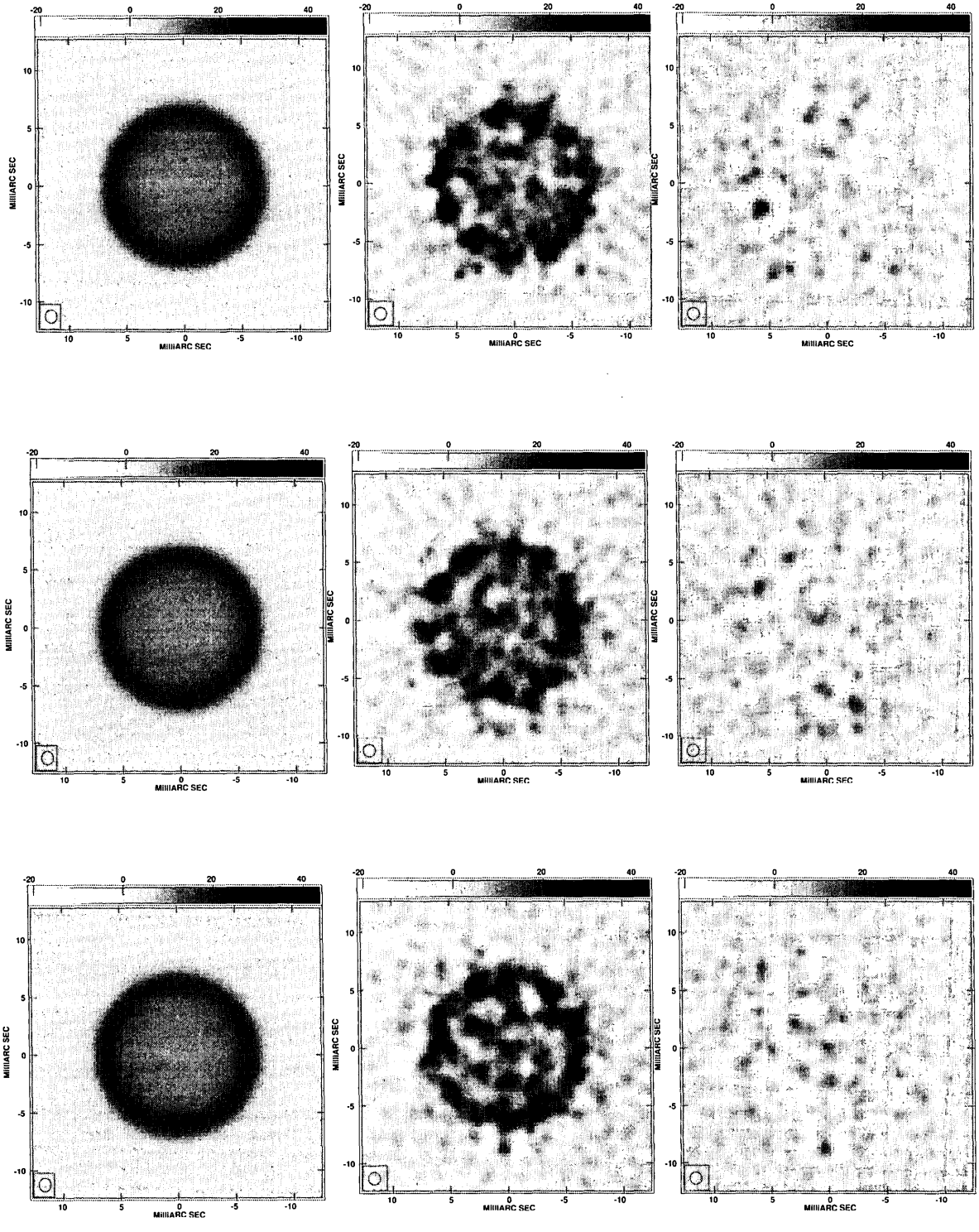

Figure 6.2 The left panel shows the brightness distribution of the projection on the sky of a model supernova. The middle panel shows the clean image for one specific realization of noise from simulated VLBI observations of the model from the left panel. The right panel shows the difference for that same example channel as shown in the middle panel computed from subtracting the right panel (model image) from the clean image (middle panel). Each row shows one specific realization of noise. In other words, we show the model, clean image and difference image for three different realizations of noise. The brightness scale is indicated as a grey scale at the top in μJy/beam. The same scale was used for all 9 maps.

errors we refer to.

Table 6.1 Key characteristics of the model, clean and difference images for different noise realizations [1]

Noise realization [2]	B_{max} [3] (μJy/beam)	σ_{noise} [4] (μJy/beam)	rms_{diff} [5] (μJy/beam)	$rms_{diff}/\sigma_{noise}$ [6]	σ_{rel} [7]	FWHM, p.a. [8] (mas), (deg)
1	17.0	3.1	5.1	1.65	0.30	1.07 × 1.04, 21.4
2	17.0	3.1	4.9	1.58	0.29	1.07 × 1.04, 21.4
3	17.0	3.2	5.0	1.56	0.29	1.07 × 1.04, 21.4

1. We used a symmetric spherical shell model with $\theta_o = 15.0$ mas, weighting scheme C, robustness factor 0, 20000 clean components, gain 0.08 and full u-v coverage.
2. Number of channels. We list the first three of the 200 different channels.
3. The peak brightness of the model image.
4. The noise background, σ_{noise}, of the clean image over the region which is free of radio emission.
5. Image errors of the clean images made from simulated VLBI observations for the different clean images in terms of rms_{diff} computed from the difference images over the clean box as given in equation 6.1.
6. The ratio of rms_{diff} and σ_{noise}. This ratio is as an important indicator of image errors.
7. The relative uncertainty of the peak of the brightness distribution, $\sigma_{rel} = rms_{diff}/B_{max}$.
8. The FWHM and p.a. of the Gaussian clean beam.

6.2.2 Image errors in clean images for the 200-channel average

So far we have estimated image errors in clean images, each with 200 different noise re-

alizations in as many channels. The image errors should contain a purely statistical contribution from the noise that we added and a contribution from the incomplete u-v coverage. It is not clear whether there is a systematic component from the incomplete u-v coverage. Averaging the 200 channel clean images should decrease σ_{noise} by a factor ~ 14. Measuring the rms_{diff} for the averaged image should then indicate if there is a systematic component, by comparing whether it also decreases by a factor 14 in comparison to rms_{diff} for a single channel.

This section shows the results from investigating image errors in averaged clean images. We have selected one particular parameter, namely the robustness factor. We vary this parameter and keep the other parameters, namely the supernova model, θ_o, weighting scheme, clean components, gain and the u-v coverage fixed. We show in Figure 6.3 the symmetric spherical shell model for $\theta_0 = 15.0$ mas, the averaged clean image and the averaged difference image for robustness factors, -5 and 5. We summarize the results of estimating image errors in the averaged clean images in Table 6.2.

We can see that the averaged clean images (middle panel) are smooth and show much less clumpiness in comparison to the clean images in Figure 6.2. They also show lower background noise. The difference images (right panels) show the deconvolution errors. Both difference images show the round structure clearly. The difference image for robustness -5 shows a shell structure and a bright point in the centre where the

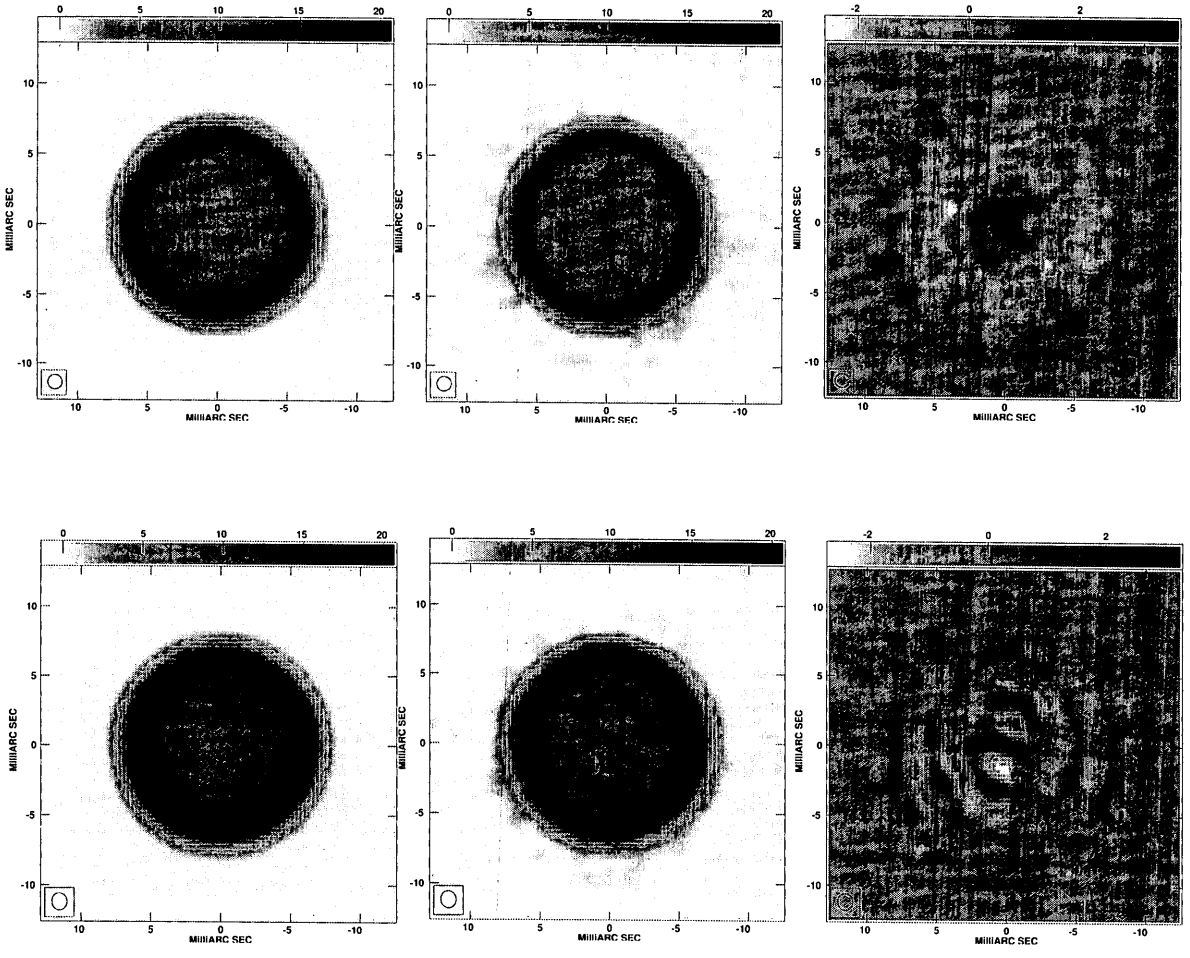

Figure 6. 3 The images made from two different robustness factors of the imaging process. The first row shows the images for robustness factor -5 , the second row for robustness factor 5. The images are in the same order as presented in Figure 6.2 except here we show the model image, the averaged clean image and the averaged difference image for the symmetric spherical shell model, $\theta_o = 15$ mas, weighting scheme C,clean components 20000, gain 0.08 and the full u-v coverage. The grey scale is the same for the left and middle panels in the two rows. It is smaller by a factor ~ 4 for the right panels in the two rows to make the residual pattern more visible.

difference image for robustness 5 shows more ripples. This means that the values of the brightness at the centre of the clean images are not equal to the value of the brightness in the centre of the model. Therefore, great care needs to be taken when searching for a compact component in the centre of the shell of a supernova.

Table 6.2 Key characteristics of the averaged clean images using different robustness factors[1]

Robustness factor	B_{max} (μJy/beam)	σ_{noise} (μJy/beam)	rms_{diff} (μJy/beam)	$\frac{rms_{diff}}{\sigma_{noise}}$	σ_{rel}	FWHM, (mas),	p.a. (deg)
-5	16.2	0.26	0.76	2.92	0.47	1.03 × 1.02,	-36.3
-4	16.2	0.26	0.76	2.92	0.47	1.03 × 1.02,	-36.3
-3	16.1	0.27	0.76	2.81	0.47	1.03 × 1.02,	-36.2
-2	16.3	0.27	0.73	2.70	0.44	1.03 ×1.02,	-35.6
-1	16.3	0.26	0.71	2.73	0.42	1.03 × 1.03,	-23.7
0	17.3	0.24	0.65	2.71	0.33	1.07 × 1.04,	21.4
1	18.4	0.22	0.65	2.95	0.33	1.15 × 1.02,	21.4
2	19.4	0.22	0.65	2.95	0.33	1.21 × 1.07,	10.2
3	19.8	0.22	0.64	2.91	0.32	1.21 × 1.08,	10.4
4	20.1	0.22	0.64	2.91	0.32	1.22 × 1.08,	10.5
5	20.2	0.21	0.64	3.05	0.32	1.22 ×1.08,	10.5

1. We used a symmetric spherical shell model for $\theta_o = 15.0$, weighting scheme C, robustness factor 0, clean components 20000, gain 0.08 and the full u-v coverage.

As is apparent from Table 6.2, the peak of the brightness of the averaged clean image varies around the values between 16.0 and 20.2 μJy/beam and is the smallest for robustness factor -5 and the largest for factor 5. This is expected since increasing the robustness factor emphasizes more and more the denser inner region of the u-v coverage

and therefore broadens the beam. With a larger beam for our model supernova, the brightness should increase. Also, with a larger beam the background noise is more averaged and σ_{noise} should decrease.

Indeed, the values for σ_{noise} in our Table 6.2 decrease. The interesting issue is that σ_{noise} of the averaged clean images is reduced by a factor of 13.0 in comparison to the clean images from any noise realization, which is very close to what was expected namely that σ_{noise} of the averaged clean images would be reduced by a factor of 14.1. Reducing σ_{noise} of the averaged clean images is a consequence of averaging over 200 channels. It is a significant result that rms_{diff} does not go down by the square root of 200 but only by a factor of 6.7 to 7.8. This indicates a systematic component to rms_{diff} which is not independent from one noise realization to the other. The ratio of $rms_{diff}/\sigma_{noise}$ for the averaged-channel clean images ranges from 2.71 to 3.04. It is expected that they are larger than in Table 6.1 because we reduced the background noise by averaging. The systematic component however is not that much reduced resulting in larger $rms_{diff}/\sigma_{noise}$ values . The value of σ_{rel} is used to judge the quality of the clean image. The images with smaller σ_{rel} have better quality and are more reliable. The values of σ_{rel} vary from 0.32 to 0.47 in Table 6.2. The value of σ_{rel} for the clean image made with robustness factor -5 is 0.47 whereas that of the clean image made with robustness factor +5 is just 0.32. The difference can be easily seen from the difference

images in Figure 6.3 (right panels). Also the size of the elliptical Gaussian clean beam depends on the robustness factor. Images made from negative values of the robustness factor are high-resolution images with small FWHM of the elliptical Gaussian clean beam. In contrast, the images made from positive values of the robustness factors have larger FWHM of the elliptical Gaussian clean beam.

6.2.3 Image errors in clean images for zero noise

So far we estimated the image errors in clean images with different noise realizations and the channel-averaged clean images. Now we are interested in investigating image errors in clean images with zero noise. Then we will be able to compare the obtained results from estimating the image errors in clean images with the three different levels of noise. We make clean images with no noise to study the pure effect of incomplete u-v coverage on clean images. We choose the symmetric spherical shell model, $\theta_o = 15.0$ mas, weighting scheme C, robustness factor 0, clean components 20000, gain 0.08 and u-v coverage, full. First, the brightness distribution of the model supernova, second the clean image and third the difference image are presented in Figure 6.4. The difference image in Figure 6.4 (first row) shows pure deconvolution errors because the clean image is free of noise. The difference image shows circular ripples. This difference image gives a lower limit on deconvolution errors.

The complicating factor is that deconvolution errors are also expected to depend on the noise level. The difference image in Figure 6.4 (second row) shows deconvolution

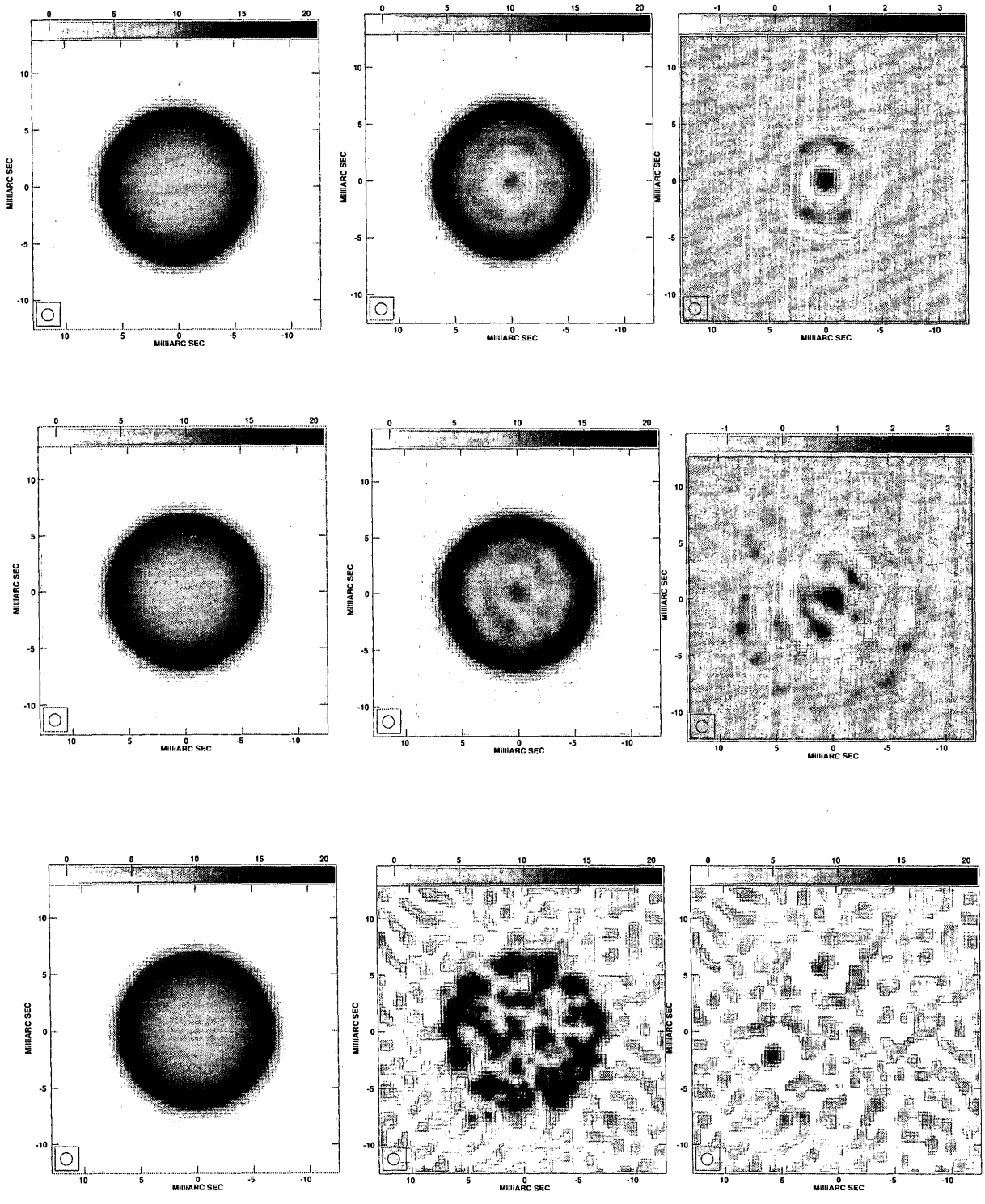

Figure 6.4 First row, the left panel shows the brightness distribution of the projection on the sky of a model

supernova. The middle panel shows the clean image with zero noise from simulated VLBI observations of the model from the left panel. The right panel shows the difference image computed from subtracting the model image from the clean image (left panel). The second row shows the model image, the 200-channel averaged clean image and the difference image. The third row shows the model image, the clean image with one realization of noise and the difference image.

errors together with some contribution from noise. The noise level is low since the noise was reduced in the clean image through averaging. The difference image in Figure 6.4 (third row) shows image errors due to noise and deconvolution errors. Here no circular ripples are visible anymore and image errors are apparently dominated by noise. In Table 6.3 we list our quantitative analysis of the images.

Table 6.3 The key characteristics of the model, clean and difference image for the study of the effect of noise[1]

Noise characterization	B_{max} (μ Jy/beam)	σ_{noise} (μ Jy/beam)	rms_{diff} (μ Jy/beam)	$\frac{rms_{diff}}{\sigma_{noise}}$	σ_{rel}	FWHM, p.a. (mas), (deg)
No noise	17.0	—	0.36	—	0.01	1.07× 1.04, 21.4
Averaged noise	17.0	0.24	0.56	2.33	0.03	1.07× 1.04, 21.4
One realization of noise	17.0	3.2	5.0	1.56	0.29	1.07× 1.04, 21.4

1. The data in this Table are listed in the same order as in Table 6.1. We used the symmetric spherical shell mode with θ_o=15.0, weighting scheme C, robustness factor 0, clean components 20000, gain 0.08 and the full u-v coverage.

The values of the peak brightness of the model images are the same because the model and the size of the convolving beam are the same. Again, as expected, the value of σ_{noise} for the channel-averaged clean image is reduced to 0.24 μJy/beam. The reduction factor is 3.2/0.24=13.3 very close to the expected factor. The value of rms_{diff} for the clean image with zero noise is 0.36 μJy/beam. This value of the rms_{diff} is just due to pure incomplete u-v coverage for zero noise. The value of rms_{diff} for the averaged clean image is 0.56 μJy/beam, larger than what would be expected from the added contribution of σ_{noise} = 0.24 μJy/beam. On a purely statistical basis, rms_{diff} would be expected to be $\sqrt{(0.24^2+0.36^2)}$ =0.43 μJy/beam or just 0.19 μJy/beam larger if the deconvolution errors were purely statistical. However, it is not the the case. The value of rms_{diff} is larger by 0.32 μJy/beam, or 2.3 times larger than σ_{noise}. Based on our analysis here we can say that the absolute contribution of deconvolution errors, because of incomplete u-v coverage, increases with σ_{noise}. This is an important result from this thesis. However, the ratio of rms_{diff} to σ_{noise} goes down. For a clean image with one realization of noise it is 1.56. This means that the value of the image errors are again larger than the value of the rms background noise. When we assess clean images using the value σ_{rel}, we can conclude that the clean images with one realization of noise have the largest relative image errors and the worst quality. Furthermore, due to using the same combination of parameters of weighting scheme C and the robustness factor 0, all images have the same beam size.

6.2.4 Image errors in clean images for different models of a supernova

This section presents the results of estimating image errors in clean images as a function of the supernova model, namely the symmetric spherical shell model, the asymmetric spherical shell model and the disk model, by keeping the other parameters, namely θ_o, the weighting scheme, the robustness factor, the clean components, gain and the u-v coverage fixed as listed in rows 1 to 3 in Table 5.2 and described in section 5.4. Again, for best comparison and ease of understanding, first the brightness distribution of the model supernova, second the clean image and third the difference image for the three different supernova models are presented in Figure 6.5. In Table 6.4 we list our quantitative analysis of the images.

As is seen from Table 6.1 the peak brightness of the disk model is the smallest one among the models because the disk model shows a uniform distribution of brightness over the supernova model and because the models have the same total flux density of 1.6 mJy. Again, we want to point out that here and hereafter all the values for the rms_{diff} were estimated over 200 channels. For this reason σ_{noise} and rms_{diff} for the symmetric spherical shell model can be slightly different than from those in Table 6.1 for the same model. We will now use the symmetric spherical shell model for the rest of this chapter.

As is seen from Table 6.4 the peak brightness of the disk model is the smallest one among the models because the disk model shows a uniform distribution of brightness

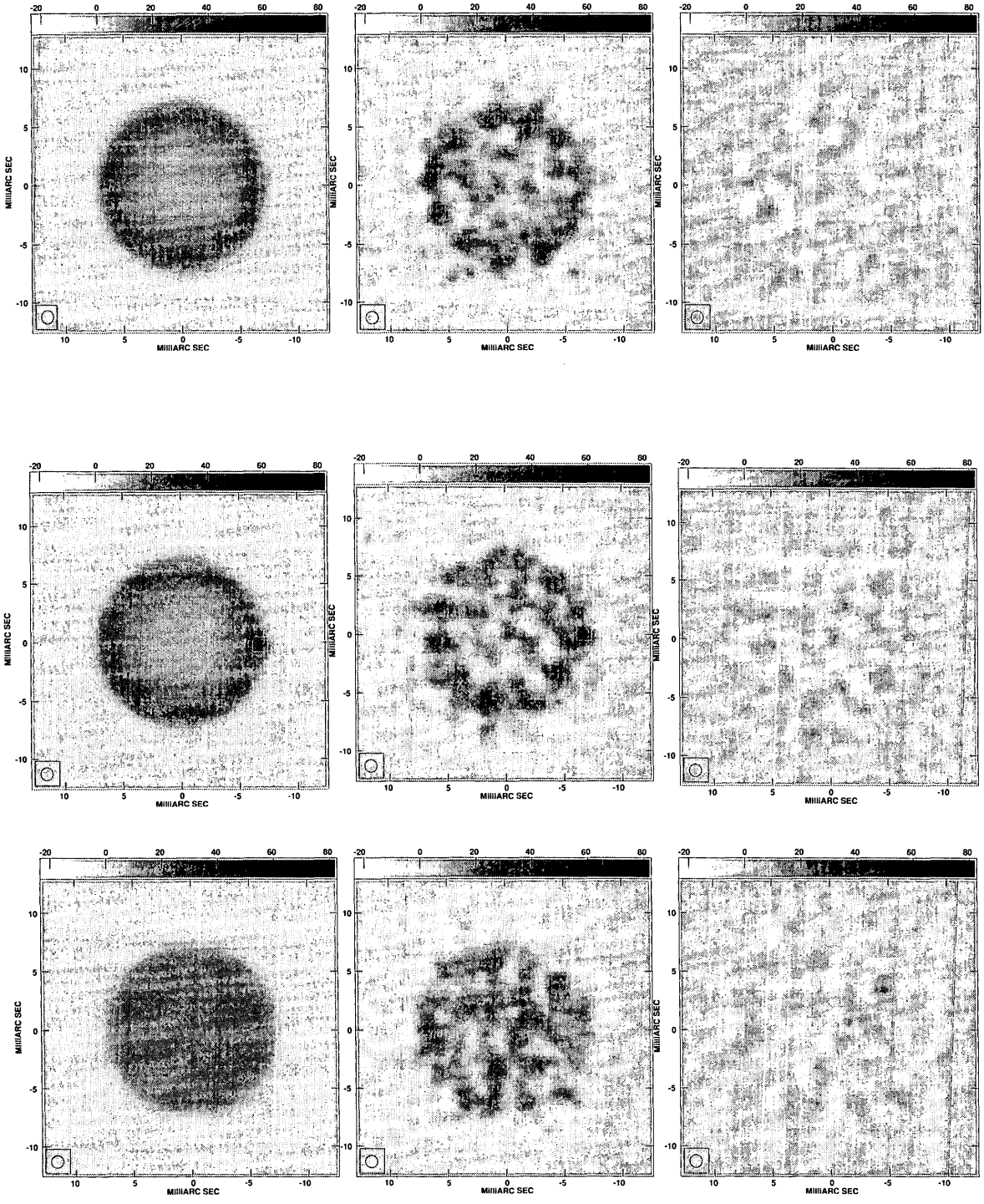

Figure 6.5 The upper row shows the symmetric spherical shell model, the middle row shows the asymmetric spherical shell model and the lower row shows the disk model.

Table 6.4 Key characteristics of the model, clean and difference images for different model supernovae

Model 1 supernovae	B_{max} (μJy/beam)	σ_{noise} (μJy/beam)	rms_{diff} (μJy/beam)	$\frac{rms_{diff}}{\sigma_{noise}}$	σ_{rel}	FWHM, (mas), P.a. (deg)
Symmetric	17.0	3.2	5.0	1.56	0.29	1.07 x1.04, 21.4
Asymmetric	17.3	3.1	5.0	1.61	0.29	1.07 x1.04, 21.4
Disk	11.4	3.1	4.7	1.52	0.42	1.07 x1.04, 21.4

1. Different supernova models, namely the symmetric spherical shell model, the asymmetric spherical shell model and the disk model, with $\theta_o = 15.0$ mas, weighting scheme C, robustness factor 0, clean components 20000, gain 0.08 and full u-v coverage as listed in rows 1 to 3 in Table 5.2. The other parameters are listed in the same order as described in Table 6.1. The value of B_{max} for the asymmetric spherical shell model does not correspond to the peak of the brightness of the point source in the model image. In stead it was chosen to be the maximum of the ridge of the shell in the model image. The reason for that is to obtain a reasonable value for σ_{rel} that can be compared to the value of σ_{rel} for the other models.

over the supernova model and all the models have the same total flux density of 1.6 mJy. The value of the σ_{noise} for all three clean images is almost the same because the same region was chosen to estimate the σ_{noise} . The image errors in terms of rms_{diff} for the clean image of the disk model are larger than σ_{noise} . In particular, the $rms_{diff}/\sigma_{noise}$ is about 1.6. This ratio for the clean image of the asymmetric shell model is just slightly larger than others. The σ_{rel} of the clean image for the disk model is the largest one namely 0.42. All clean images have the same size of the FWHM because they have been made with the same weighting scheme and robustness factor, namely C and 0, respec-

tively. Again, we want to point out that here and hereafter all the values for the rms_{diff} were estimated over 200 channels. For this reason σ_{noise} and rms_{diff} for the symmetric spherical shell model can be slightly different from those in Table 6.1 for the same model. We will now use the symmetric spherical shell model for the rest of this chapter.

6.2.5 Image errors in clean images for different values of θ_o

This section will present the results of estimating the image errors in clean images made from simulated visibility data as a function of θ_o , by keeping the other parameters, namely the model, weighting scheme, robustness factor, clean components, gain and u-v coverage fixed, as listed in rows 4 to 6 in Table 5.2. Figure 6.6 presents the symmetric spherical shell model, clean images for one realization of noise and the difference images for θ_o = 19.5, 15.0 and 5.6 mas, displayed in the top, middle and bottom row, respective respectively. As we can see from Figure 6.6 the clean image with θ_o=5.6 mas shows an almost uniform brightness distribution around the ridge of the shell. In contrast, the clean image with θ_o=19.5 mas does not show a uniform or smooth brightness distribution along the ridge and has the worst quality. We list the results from estimating image errors in the clean images for the three different values of θ_o in Table 6.5.

As can be seen from Table 6.5 the clean image with the smallest angular diameter has the largest peak brightness. That is because model images have the same total flux density,

namely 1.6 mJy. The brightness rms of the noise, σ_{noise}, for all the clean images is approximately the same because, again, the same level of the noise has been added to the simulated data and also the same region was selected to determine σ_{noise}. The values of the rms_{diff} vary from 4.5 to 5.2 and are 1.45 to 1.59 times larger than those of σ_{noise}, also approximately the same for all θ_o, as expected. The values for σ_{rel} are largest for θ_o=19.5 mas and decrease rapidly with decreasing θ_o. The smallest value of σ_{rel} is for the clean image with the smallest θ_o,namely 5.6 mas which is just 0.05. Clearly, σ_{rel} is more dependent on the size of the model if all of them have the same flux density and the same beam, than on the kind of the model. The size of the Gaussian clean beam for all clean images is the same because all clean images have been made with the same weighting scheme, robustness factor and u-v coverage.

6.2.6 Image errors in clean images for different weighting schemes

This section will present the results from investigating image errors in the clean images as a function of weighting schemes C and CS by keeping the other parameters namely, model supernova, θ_o , robustness factor, clean components, gain and u-v coverage fixed

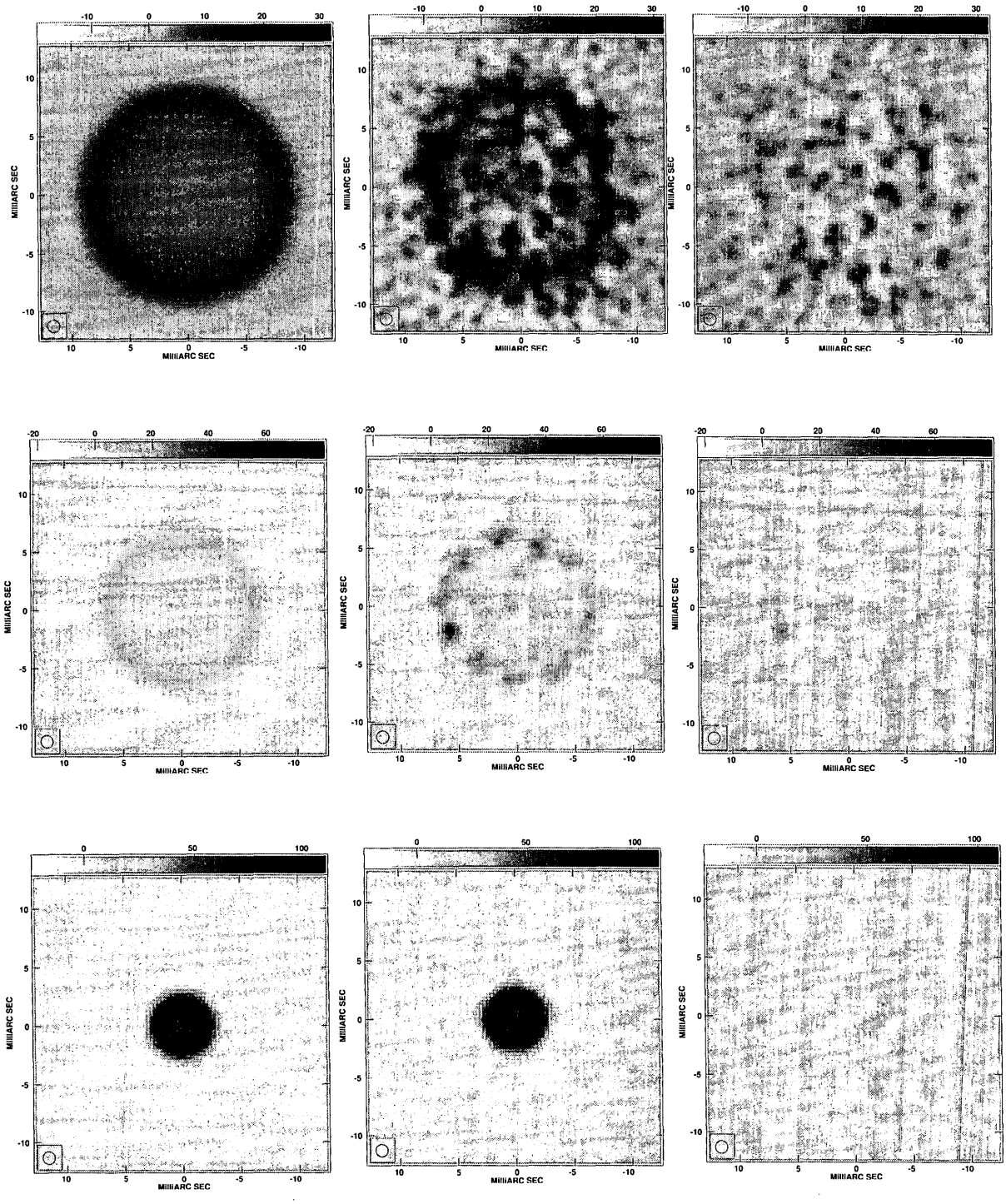

Figure 6.6 The images for a symmetric spherical shell model for three different values of θ_o, namely 19.5, 15.0 and 5.6 mas for the top, middle and bottom row, respectively.

Table 6.5 Key characteristics of the model, clean and difference images for different θ_o

θ_o 1 (mas)	B_{max} (μJy/bem)	σ_{noise} (μJy/beam)	rms_{diff} (μJy/beam)	$\frac{rms_{diff}}{\sigma_{noise}}$	σ_{rel}	FWHM, p.a. (mas), (deg)
19.5	10.6	3.1	4.5	1.45	0.42	1.07 ×1.04, 21.4
15.0	17.0	3.2	5.0	1.56	0.29	1.07 ×1.04, 21.4
5.6	85.5	3.2	5.1	1.59	0.06	1.07 ×1.04, 21.4

1. The outer angular diameter of the shell. The other parameters are listed in the same order as described in Table 6.2. We used the symmetric spherical shell model with θ_0=15.0, weighting scheme C, robustness factor 0, 20000 clean components, gain 0.08 and the full u-v coverage.

as listed in rows 7 to 8 in Table 5.2. We show the brightness distribution of the model supernova, the clean images made for two different weighting schemes and the difference images in Figure 6. 7. We summarize the key characteristics of the images in Table 6.6. It can be seen clearly from Table 6.6 that B_{max} of the clean image made from weighting scheme C is larger than that of the clean image for CS. This may be due to noise fluctuations. Both the σ_{noise} value and rms_{diff} value for weighting scheme C are only 60 to 70% of those for the image made with weighting scheme CS. Again we want to remind the reader that the value of rms_{diff} is estimated over 200 channels for both clean images. The rms_{diff} to σ_{noise} ratios are less different and again clearly larger than unity. When rms_{diff} is compared to B_{max} we get values of σ_{rel} that reach, for the image with weighting scheme CS, to more than 0.5. Clearly the clean image made with CS

weighting scheme has larger image errors. The images also have slightly different beam sizes because of the different weighting of the antenna data.

Table 6.6 Key characteristics of clean and difference images made from different weighting schemes

Weighting scheme [1]	B_{max} (μJy/bem)	σ_{noise} (μJy/beam)	rms_{diff} (μJy/beam)	$\frac{rms_{diff}}{\sigma_{noise}}$	σ_{rel}	FWHM, (mas), p.a. (deg)
C	17.0	3.2	5.0	1.56	0.29	1.07 × 1.04, 21.4
CS	15.6	4.7	8.5	1.81	0.54	1.02 × 0.98, 22.3

1. The weighting scheme as defined in Chapter 2. The other parameters are listed in the same order as described in Table 6.2. We used the symmetric spherical shell model for θ_o=15.0 mas, robustness factor 0, 20000 clean components, gain 0.08 and full u-v coverage for weighting scheme C and CS.

6.2.7 Image errors in clean images for different robustness factors

This section presents the results from investigating image errors in clean images as a function of robustness factor, by keeping the other parameters, namely supernova model, θ_o, weighting scheme, clean components, gain and u-v coverage fixed as listed in row 9 in Table 5.2. Figure 6.8 shows an image of the symmetric spherical shell model, clean and difference images for two particular robustness factors, -5 and 5. We summarize the results of estimating image errors for clean images made for robustness factors -5, -4, -3,

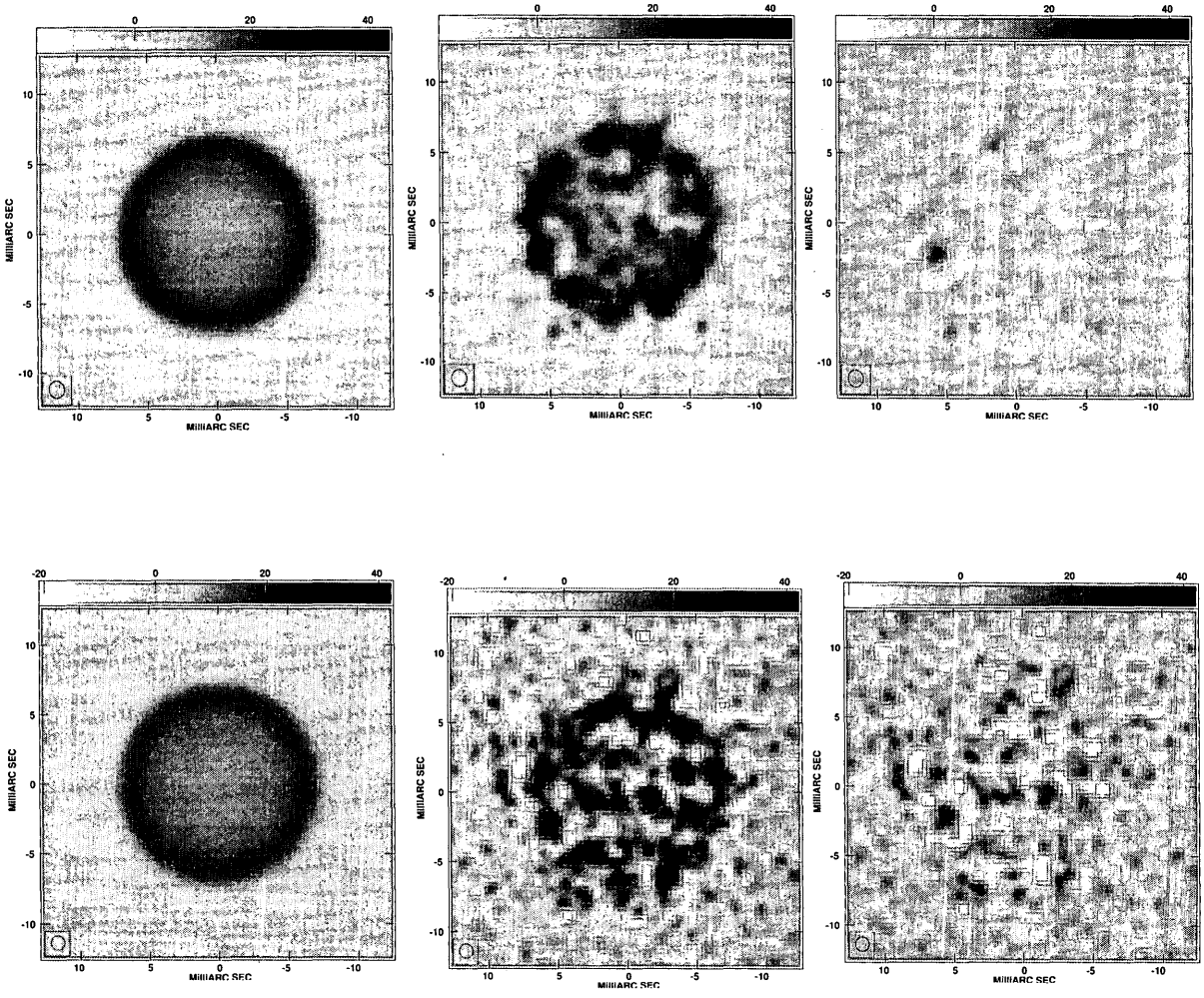

Figure 6.7 Images for a symmetric spherical shell model for two different weighting schemes. The first row shows images made from weighting scheme C and the second row shows images for CS. The images are shown in the same order as shown in Figure 6.1. The grey scale for two rows of the image are almost the same to better show the effect of using different weighting schemes.

-2, -1, 0, 1, 2, 3, 4, 5 using weighting schemes C and CS separately in Tables 6.7 and 6.8, respectively.

The obtained results from our simulation study for weighting scheme C show that the clean images made from positive robustness factors have a larger peak brightness than those made from negative robustness factors. This is due to our u-v coverage which is denser in the inner region than in the outer region. This has the effect of broadening the beam. With a broader beam, B_{max}, the flux density per beam area, is expected to increase for our model. In the same way, rms_{diff}, may be expected to decrease. It is interesting to see that for a robustness factor -5, the value of rms_{diff} is ~ 1.5 times larger than the value of σ_{noise} and increases to ~ 1.8 for a robustness factor of +5. As can be seen, the clean image made from robustness factor +5 has better quality than the clean image made with robustness factor -5. This means that the clean image for +5 has smaller image errors than the clean image made for -5. All said, the values of σ_{rel} indicate that clean images made with positive robustness factors have smaller image errors, however the angular resolution is worse. The best compromise between low rms_{diff} and σ_{rel} and a small beam for high angular resolution is a robustness factor of 2.

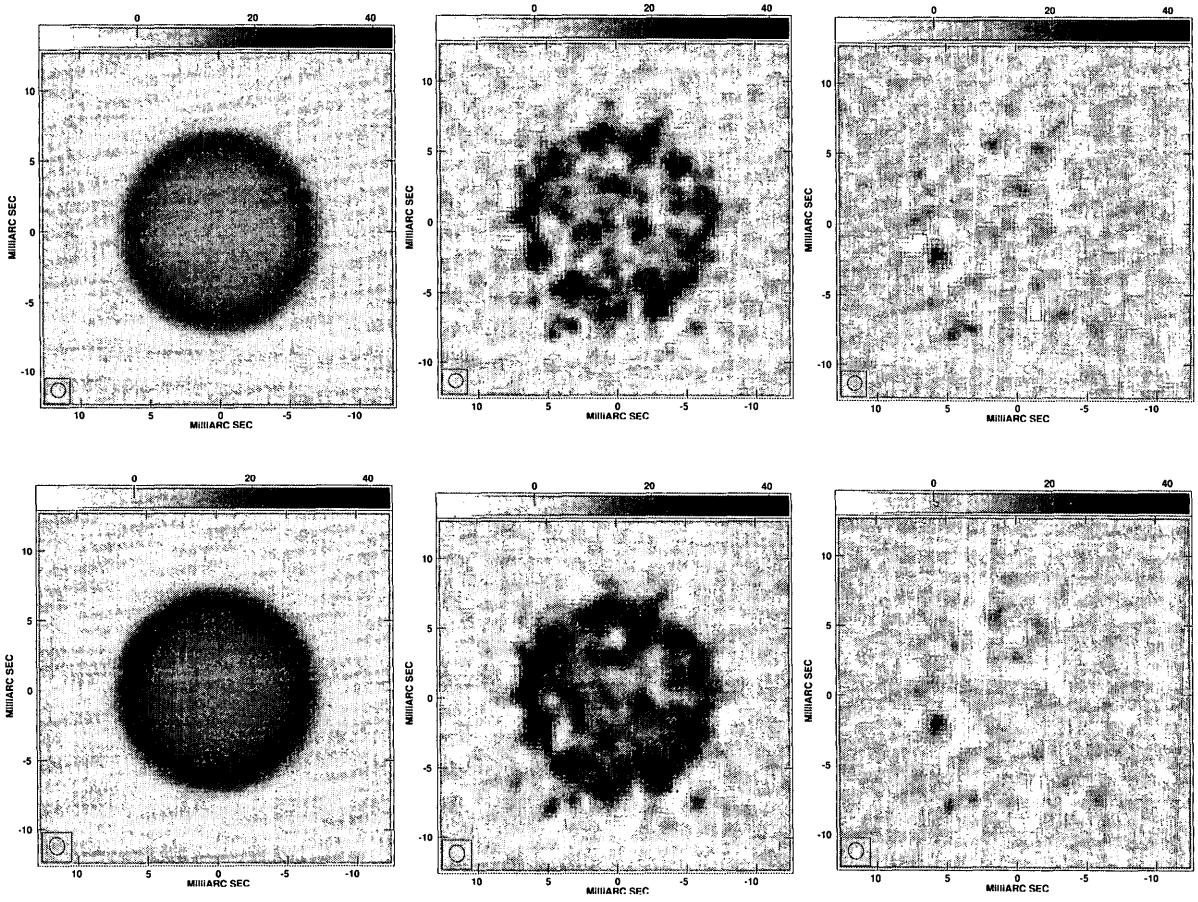

Figure 6.8. The images made from robustness factor, -5 and 5 . The first row is for -5 (uniform weighting), the second row is for 5 (natural weighting). The images in the columns are in the same order as shown in Figure 6.2. The grey scale is the same for all images.

Table 6.7. Key characteristics of the clean and difference images for different robustness factors for weighting scheme C

Robustness factor [1]	B_{max} (μJy/beam)	σ_{noise} (μJy/beam)	rms_{diff} (μJy/beam)	$\frac{rms_{diff}}{\sigma_{noise}}$	σ_{rel}	FWHM, (mas),	p.a. (deg)
-5	16.2	3.5	5.4	1.54	0.33	1.03 x1.03,	-36.3
-4	16.2	3.5	5.4	1.54	0.33	1.03 x1.02,	-36.3
-3	16.1	3.5	5.4	1.54	0.33	1.03 x1.02,	-36.3
-2	16.2	3.5	5.4	1.54	0.33	1.03 x1.02,	-36.2
-1	16.3	3.4	5.2	1.53	0.32	1.03 x1.03,	-35.6
0	17.0	3.2	5.0	1.56	0.29	1.07 x1.04,	21.4
1	18.0	2.9	4.9	1.69	0.27	1.07x1.04,	21.4
2	19.4	2.8	4.9	1.75	0.25	1.20 x1.07,	10.2
3	20.0	2.8	4.9	1.75	0.25	1.21 x1.08,	10.4
4	20.0	2.8	4.9	1.75	0.25	1.22 x1.08,	10.4
5	20.0	2.8	4.9	1.75	0.25	1.22 x1.08,	10.4

1. The robustness factors as described in chapter 2. The other parameters for a symmetric shell model with $\theta_o = 15.0$, weighting scheme C, 20000 clean components, gain 0.08 and full u-v coverage are listed in the same order as described in Table 6.1.

When the study is done with weighting scheme CS, the values of B_{max} vary over a slightly larger range than when weighting scheme C is used. More important, the values of σ_{noise} and rms_{diff} are about 80% higher than for weighting scheme C. The outer portion of the u-v coverage is largely unfilled which results in large values of rms_{diff}.

Table 6.8. Key characteristics of the clean and difference images for different robustness factors for weighting scheme CS

Robustness factor [1]	B_{max} (μJy/bem)	σ_{noise} (μJy/beam)	rms_{diff} (μJy/beam)	$\frac{rms_{diff}}{\sigma_{noise}}$	σ_{rel}	FWHM, p.a. (mas), deg
-5	14.7	6.2	9.6	1.55	0.65	1.0x 0.94, 1.4
-4	14.7	6.2	9.6	1.55	0.65	1.0x 0.93, 1.4
-3	14.7	6.2	9.6	1.55	0.65	1.0x 0.94, 1.4
-2	14.7	6.1	9.5	1.56	0.65	1.0 x 0.94, 1.8
-1	14.9	5.9	9.3	1.58	0.62	1.0 x 0.95, 3.9
0	15.6	4.7	8.5	1.81	0.55	1.0x 0.98, 22.3
1	17.8	4.7	8.2	1.74	0.46	1.1x1.0, 6.7
2	20.7	4.7	8.4	1.79	0.41	1.3x1.1, 12.0
3	21.5	4.7	8.5	1.81	0.40	1.3 x 1.1, 12.0
4	21.5	4.7	8.5	1.81	0.40	1.3x1.1, 12.0
5	21.6	4.7	8.5	1.81	0.40	1.3x1.1, 12.0

1. Data are listed in the same order as in Table 6.2 but now the CS weighting scheme is used.

This has the effect of $rms_{diff}/\sigma_{noise}$ remaining about unchanged for C and CS weighting. The values of σ_{rel} increase ~ 80% since rms_{diff} increases a lot but B_{max} remains about unchanged. Also, with the largest baselines relatively more emphasized, that leads to higher-resolution clean images, namely clean images with a smaller value of FWHM. For better inspection, we plot in Figure 6.9 the variation of σ_{noise} and rms_{diff} versus the robustness factor for clean images made from weighting scheme C and CS. The smoothness of the variation can now be clearly seen. It is also clearly apparent that the trend of the functions is similar for C and CS weighting but that CS weighting will

result for our images in a larger background noise and larger image errors.

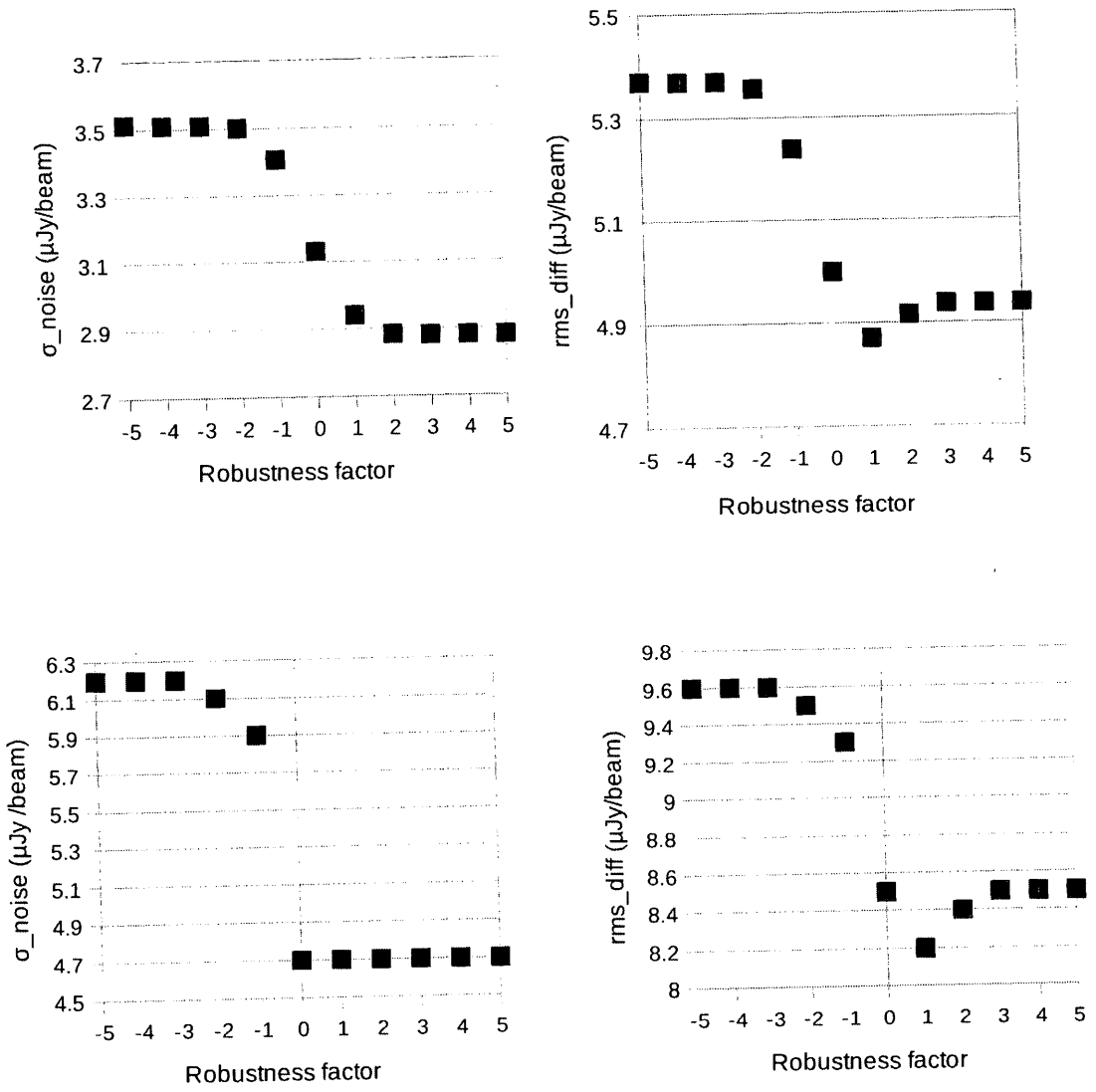

Figure 6.9. The variation of rms of the background noise, σ_{noise} and rms_{diff} as a function of robustness factors for the clean images made from simulated visibility data for two different weighting schemes. The first row displays the variations for the clean image for weighting scheme C and the second row is for weighting scheme CS.

6.2. 8 Image errors of clean images for different clean components

This section presents the results from investigating image errors in clean images as a function of clean components. We vary the number of clean components by keeping the other parameters, namely supernova model, θ_o , weighting scheme, and robustness factor, gain and u-v coverage fixed as listed in row 10 in Table 5.2. In Figure 6.9 we present, as before, first the brightness distribution of the model supernova, second the clean image and third the difference image for the 20000 clean components in the first row and for the 4000 clean components in the second row. Then we summarize the results from estimating image errors in the clean images made from different numbers of clean components in Table 6.9.

As it is seen from Table 6.9, B_{max} is the same for all entries since the same model and the same beam were used. Also, understandably (almost) the same values for σ_{noise} were obtained. However, rms_{diff} and $rms_{diff}/\sigma_{noise}$ increase with the number of clean components. This was not necessarily expected. For instance, as mentioned already in Chapter 5.4, the clean image with 4000 clean components shows a rather bright central component which does not appear particularly bright in the clean image with 20000 clean components. Nevertheless, rms_{diff} is smaller for the image with 4000 clean components. Inspection of the difference image indicates that this rather bright central component may be only a spurious effect. In general, using the larger value of clean components in the CLEAN algorithm leads to images with larger image errors in the form of rms_{diff} and $rms_{diff}/\sigma_{noise}$, while σ_{noise} remains about constant. This is a

surprising result. The reason is not clear. One possibility is that the total cleaned flux density is already close to 1.6 mJy for the clean image with 10000 and 20000 clean components. Using a larger number of clean components does not increase the cleaned

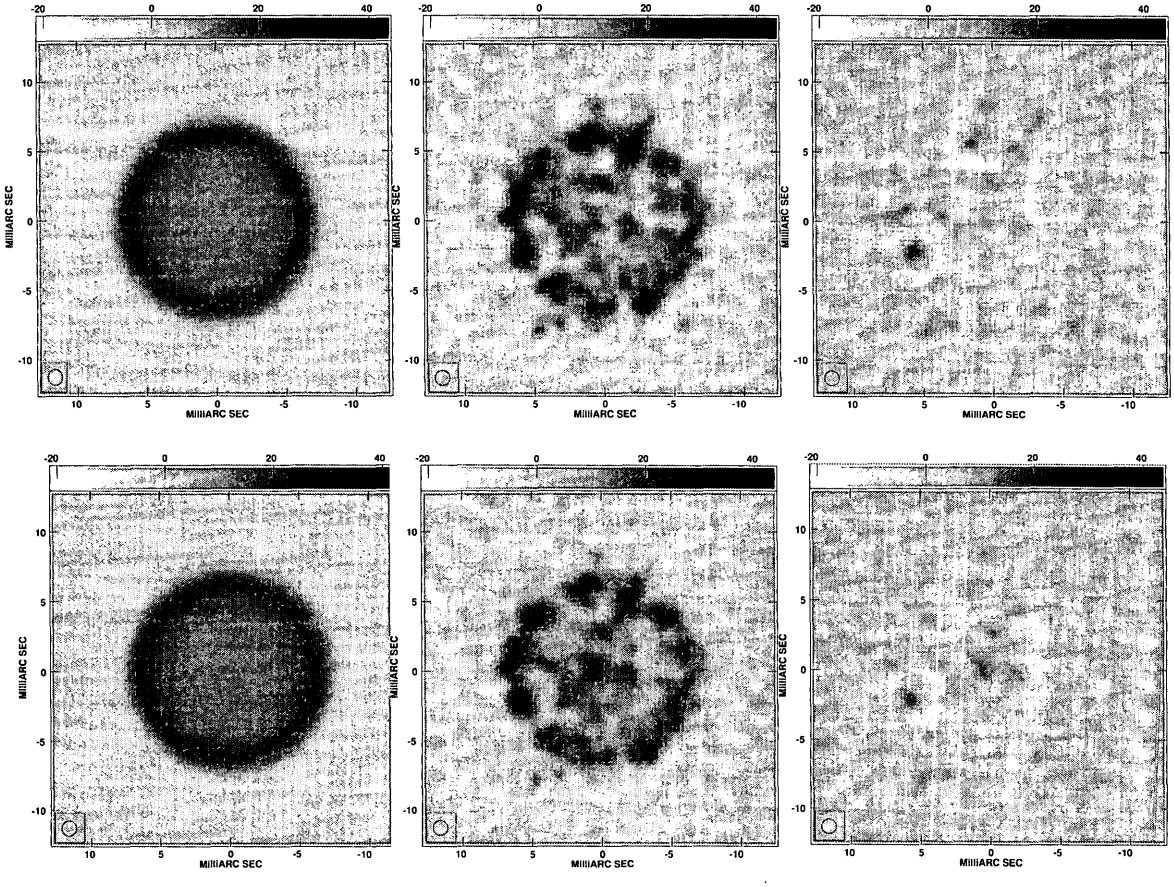

Figure 6.10. The images made from clean components 20000 and 4000. The first row is for 20000 and the second row is for 4000. The images are in the columns in the same order as shown in Figure 6.2. The grey scale is the same for all images.

flux density much, but instead the noise in a clean image. This process may increase rms_{diff}. The best choice for the number of clean components appears to be ~ 4000 since it gives us the smallest value for rms_{diff} and σ_{rel} although the cleaned flux

density is with 81% of the total flux density, a bit low. However, it could be that this percentage increases with optimizing the other parameters. We will study that in Chapter 7.

Table 6.9 Key characteristics of the clean and difference images made from different clean components [1]

Clean components [1]	B_{max} (μJy/beam)	σ_{noise} (μJy/beam)	rms_{diff} (μJy/beam)	$\frac{rms_{diff}}{\sigma_{noise}}$	σ_{rel}	FWHM, (mas), p.a. (deg)
2000	17.0	3.2	3.9	1.22	0.23	1.07 × 1.04, 21.4
4000	17.0	3.1	3.8	1.23	0.22	1.07 × 1.04, 21.4
10000	17.0	3.1	4.3	1.39	0.25	1.07× 1.04, 21.4
20000	17.0	3.2	5.0	1.56	0.29	1.07× 1.04, 21.4

1. The number of clean components as described in Chapter 2. The other parameters for a symmetric shell model with $\theta_o = 15.0$, weighting scheme C, gain 0.08 and full u-v coverage are listed in the same order as described in Table 6.1. The total cleaned flux density is, for the clean image with 2000, 4000, 10000 and 20000 clean components, 0.97, 1.30, 1.54 and 1.59 mJy, respectively.

6.2.9 Image errors of clean images for different gains

This section presents the results from investigating image errors in clean images as a function of gain. We vary the value of the gain by keeping the other parameters, namely supernova model, θ_o, weighting scheme, robustness factor, clean components and the u-v coverage fixed as listed in rows 17-19 in Table 5.2. In Figure 6.11 we present, as before, first the brightness distribution of the model supernova, second the clean image and third the difference image for different values of gain in the CLEAN algorithm. Then

we summarize the results from estimating image errors in the clean images in Table 6.10. While B_{max} and σ_{noise} remain, as expected, unchanged, rms_{diff} , $rms_{diff}/\sigma_{noise}$ and σ_{rel} increase with gain. In particular, the clean image for a gain of 0.08 has larger image errors and worse quality than the clean image made from a gain of 0.02, while σ_{noise} remains about constant.

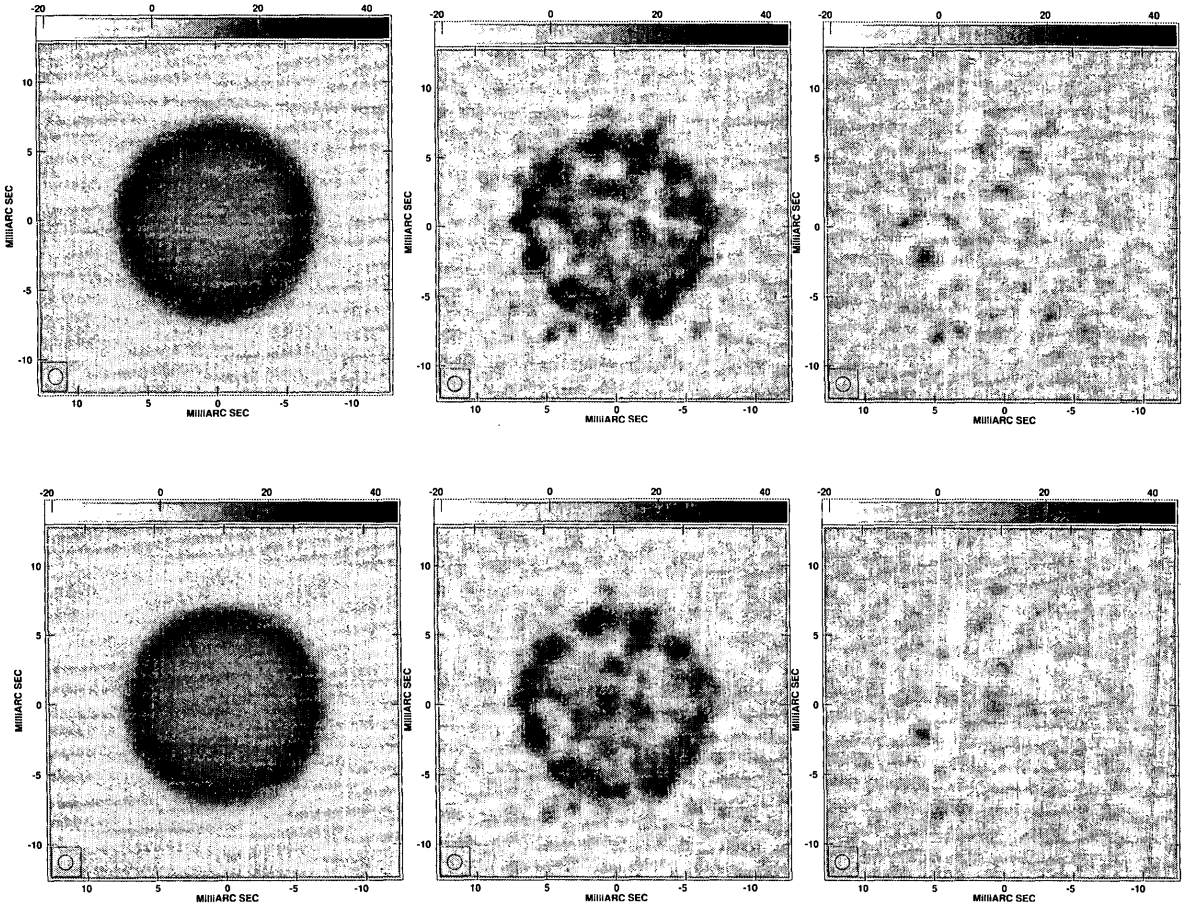

Figure 6.11. The images made from gains for 0.08 and 0.02. The first row is for 0.08 and the second row is for 0.02. The images are in the columns in the same order as shown in Figure 6.2. The grey scale is the same for all images.

As a result, instead of using the larger value of gain in the CLEAN algorithm, we can use a smaller gains to make clean images with smaller image errors provided that the cleaned flux density is close to the total flux density. This result is also surprising. Again, it could be that increasing noise was cleaned with a larger gain and that this process led to a larger rms_{diff}.

Table 6.10 Key characteristics of clean and difference images made from different values of gains [1]

Gain [1]	B_{max} (μJy/beam)	σ_{noise} (μJy/beam)	rms_{diff} (μJy/beam)	$\frac{rms_{diff}}{\sigma_{noise}}$	σ_{rel}	FWHM, p.a. (mas), (deg)
0.02	17.0	3.1	3.9	1.26	0.23	1.07 × 1.04, 21.4
0.05	17.0	3.1	4.5	1.45	0.26	1.07 × 1.04, 21.4
0.08	17.0	3.2	5.0	1.56	0.29	1.07 × 1.04, 21.4

1. The value of gain as described in Chapter 2. The other parameters for a symmetric shell model with $\theta_o = 15.0$, weighting scheme C, clean components 20000 and full u-v coverage are listed in the same order as described in Table 6.1. The total cleaned flux density for the clean images with gain 0.02, 0.05 and 0.08 is 1.37, 1.56 and 1.60 mJy, respectively.

All clean images have the same size of the FWHM and position angle because all images have been made from the same weighting scheme, robustness factor and u-v coverage. The best choice for the gain, in view of the previous choice of 4000 components, seems to be a gain of 0.05. Although a gain of 0.02 provides the smallest number for rms_{diff} and σ_{rel}, the cleaned flux density is too low if we use this gain together with 4000

clean components. A gain of 0.05 appears to be optimal.

6. 2. 10 Image errors of clean images for different u-v coverages

This section presents the results from investigating image errors in clean images as a function of u-v coverage. We vary the u-v coverage by keeping the other parameters, namely supernova model, θ_o, weighting scheme, robustness factor, number of clean components and gain fixed as listed in row 21 and 22 in Table 5.2. In Figure 6.12 we present, as before, first the brightness distribution of the model supernova, second the clean image and third the difference image for the full u-v coverage in the first row and the equivalent images for the reduced u-v coverage in the second row. Then we summarize the results from estimating image errors in the clean images in Table 6.11.

As is seen from Table 6.11, the model image corresponding to the full u-v coverage has a slightly larger peak brightness. This may be just due to the slightly different beam size. More important and as expected, with the beam size not very different it has a lower amount of background noise, σ_{noise}, and a lower value for rms_{diff}. The ratio rms_{diff} to σ_{noise} remains about the same. It also has a lower value σ_{rel} indicating that the clean image for full u-v coverage has lower relative image errors than the clean image made from the reduced coverage.

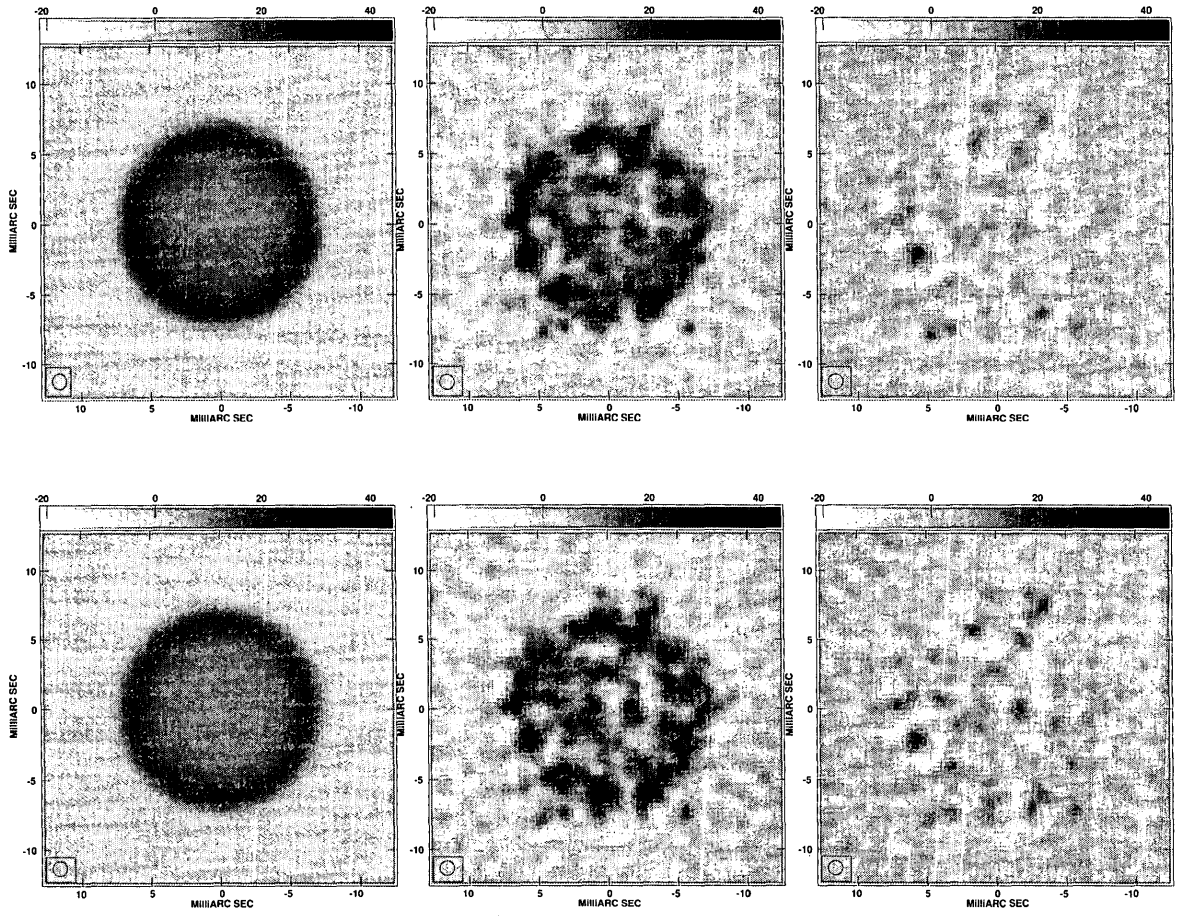

Figure 6.12 . Images made from the full and reduced u-v coverage. The images are in the same order as presented in Figure 6.2. The first row shows the images made from the full and the second row from the reduced u-v coverage. The grey scale at top of each image is the same for all images.

Table 6.11 Key characteristics of the clean image and difference images using different u-v coverages [1]

u-v coverage [2]	B_{max} (μJy/beam)	σ_{noise} (μJy/beam)	rms_{diff} (μJy/beam)	$\frac{rms_{diff}}{\sigma_{noise}}$	σ_{rel}	FWHM, p.a. (mas), (deg)
Full	17.0	3.2	5.0	1.56	0.29	1.07 × 1.04, 21.4
Reduced	16.4	3.6	5.5	1.52	0.33	1.04 × 1.03, -67.1

1. Clean images for the symmetric spherical shell model for θ_o=15.0 mas, weighting scheme C, robustness factor, 0, 20000 clean components, gain 0.08 and u-v coverage, full and reduced, respectively.
2. The u-v coverage as described in Chapter 2. The other parameters are listed in the same order as described in Table 6.1.

6.3 Summary of results from the simulation study

This section will present the summary of our results from the simulation study. The image errors arise from the noise and incomplete u-v coverage. We summarize the analysis in the same order as described in the previous sections.

Image errors in clean images as a function of noise: Our statistical analysis shows that the image errors in clean images, namely given by $rms_{diff}/\sigma_{noise}$ and σ_{rel}, are largely dominated by noise. Our noiseless simulation study (see section 6.2. 3) shows that rms_{diff} is only 0.36 μJy/beam. This value comes from deconvolution errors where no noise is present. It can be considered as a lower limit for deconvolution errors for our data. The value of rms_{diff} increases to 0.56 μJy/beam for the 200-channel averaged clean images more than what would be expected from the σ_{noise} =0.24 μJy/beam if

added in quadrature. For clean images with one realization of noise, the systematic contribution of the deconvolution errors increases further. As an important result, the ratio $rms_{diff}/\sigma_{noise}$ becomes ~ 1.6.

Image errors as a function of model supernovae: Our results show that $rms_{diff}/\sigma_{noise}$ between 1.56 and 1.61 and σ_{rel} between 0.29 and 0.42 are almost independent of whether the supernova is a symmetric spherical shell or an asymmetric spherical shell, respectively. This is an important result for further analysis since our results can be applied independent of the specific brightness modulation along the rim.

Image errors in clean images as a function of θ_o: Our analysis shows that the $rms_{diff}/\sigma_{noise}$ varies between 1.45 and 1.59. The largest variation occurs for σ_{rel} which varies between 0.42 for θ_o=19.5 mas and 0.06 for θ_o=5.6 mas. This is a result of the significantly increasing value of B_{max}. It means that the images with small θ_o are the most reliable in our study.

Image errors in clean images as a function of weighting scheme: Our analysis shows that $rms_{diff}/\sigma_{noise}$ and σ_{rel} of the clean image increases from 1.56 to 1.81 and from 0.29 to 0.54 from weighting scheme C to CS. Clearly the clean images made from weighting scheme C are of higher quality.

Image errors as a function of robustness factors: Our analysis shows that the values of $rms_{diff}/\sigma_{noise}$ vary between 1.54 and 1.75 and those of σ_{rel} between 0.25 and 0.33 for the clean images for weighting scheme C, when increasing the robustness factor from -5 to +5 . Also the values of $rms_{diff}/\sigma_{noise}$ vary between 1.55 and 1.81 and those of σ_{rel} between 0.40 and 0.65 for the clean images for weighting scheme CS. This indicates that for our source weighting, scheme C clearly produces higher quality clean images.

Image errors in clean images as a function of clean components: Our analysis shows that the values of $rms_{diff}/\sigma_{noise}$ vary between 1.22 and 1.56 and those of σ_{rel} between 0.22 and 0.29 for the clean images for weighting scheme C and robustness factor 0, when increasing the number of clean components from 2000 to 20000. This is an unexpected result and indicates that a relatively small number of clean components produces higher quality image provided, presumably, that nearly all the flux density is cleaned. The cleaned flux density for 2000 clean components is 0.97 mJy but for the 20000 clean components the total cleaned flux density is 1.60 mJy, very close to 100 % of the total flux density.

Image errors in clean images as a function of gain: Our analysis shows that the values of $rms_{diff}/\sigma_{noise}$ vary between 1.26 and 1.56 and those of σ_{rel} between 0.23 and 0.29 for the clean images for weighting scheme C and robustness factor 0 and clean components 20000, when increasing the value of gain from 0.02 to 0.08. Again this is an unexpected

result and indicates that smaller gain produces higher quality images, in terms of the small value of rms_{diff} , but the total cleaned flux density might be smaller than that for a larger value of gain. The total cleaned flux density for gain 0.02 is 1.37 mJy while that of gain 0.05 is 1.56 mJy.

Image errors in clean images as a function of u-v coverage: Our analysis shows that the values of $rms_{diff}/\sigma_{noise}$ vary between 1.52 and 1.56 and those of σ_{rel} between 0.29 and 0.33 for the images with full and reduced u-v coverage, respectively. The clear difference is in the σ_{noise} and rms_{diff} values, which are ~ 10% higher, as expected, for the reduced u-v coverage.

Now our simulation study can tell us how to make a clean image with small image errors in terms of small value for rms_{diff} , $rms_{diff}/\sigma_{noise}$ and σ_{rel} and which combination of parameters in the CLEAN algorithm such as weighting scheme, robustness factor, clean components and gain should be used for it. The best selection is a combination of weighting scheme C, robustness factor 2, number of clean components 4000 and gain 0.05.

Now that we have figured out how image errors, namely rms_{diff} , $rms_{diff}/\sigma_{noise}$ and σ_{rel} in VLBI images can be reduced, we can make the "best" clean images of SN 1993J as will be described in detail in Chapter 7.

Chapter 7

The best clean image of supernova 1993J from VLBI observations on 2007 Nov. 3

This chapter is devoted to using the results of our analysis described in Chapter 6 and applying them to VLBI data. We present a new clean image of SN 1993J for one epoch of VLBI observations taken on 2007 Nov. 3 and compare it with one made by Bietenholz and Bartel (2008) using visibility data from the same VLBI observations, and also with the best clean image made from simulated VLBI observations. The simulated VLBI observations are made using a symmetric spherical shell model of a supernova with a total flux density of 1.6 mJy and an outer diameter of 15.0 mas, the same as was found for SN 1993J with a flux density of 1.6 mJy and an outer diameter of 15.0 mas by Bietenholz and Bartel (2008). We will critically evaluate apparent brightness variations in the clean image of SN 1993J on the basis of our simulation studies. As another outcome of this study, we are also determining an upper limit on the spectral luminosity and the brightness of any PWN that may exist in the centre of SN 1993J.

7.1 VLBI observations of SN 1993J

SN 1993J was observed with VLBI on 2007 Nov. 3 using 18 radio telescopes at 5.0 GHz for 24 hours. The corresponding u-v coverage is shown in Figure 7.1. Its high declination enabled us to have 100% visibility of the source from most radio telescopes, and thus a dense and excellent u-v coverage was obtained. The gaps in the u- v coverage produce image errors in the clean images of SN 1993J.

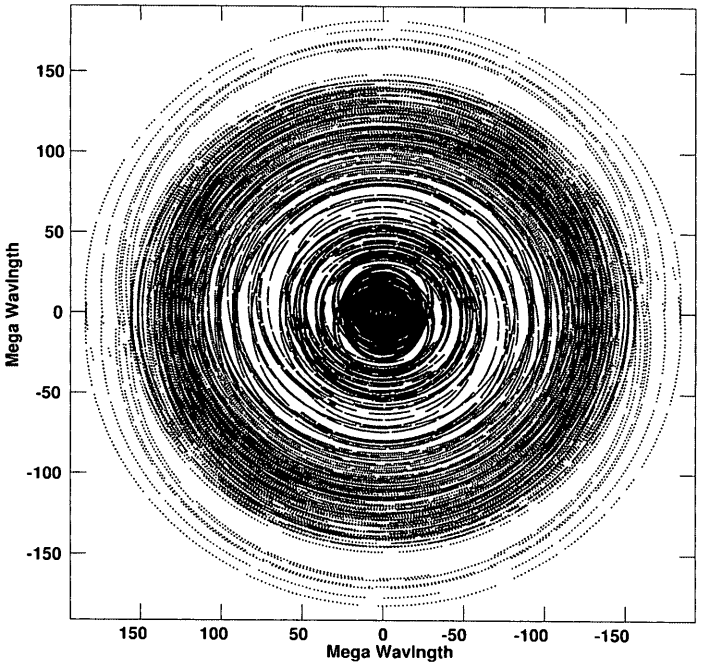

Figure 7.1 The u-v coverage for the VLBI observations of SN1993J on 2007 Nov 3. For these observations 18 antennas were used and the observation frequency was 5.0 GHz. The horizontal axis is the spatial frequency, u, and the vertical axis is the spatial frequency, v. Both, u and v, are given in millions of wavelengths. The key characteristics of the 18 VLBI stations are listed in Table 7.1.

We give information about the VLBI stations that were used for observing SN 1993J in Table 7.1.

Table 7.1: Information for VLBI stations

Code	Location [1]	Affiliation	Diameter (m)
Y	Soccoro, NM	NRAO	130[2]
GB	Green Bank, WV	NRAO	105
EF	Effelsberg, Germany	MPIfR	100
WB	Westerbork, The Netherlands	ASTRON	94[2]
JB	Jodrell Bank, United Kingdom	UM	76
MC, NT	Medicina, Noto Italy	IDR-CNR	32
BR, FD HN,KP, LA,MK, NL, OV, PT	B, WA-F.D, TX-H.N, HA-K.P, AZ – LA, NM-MK, HI- OV,CA- PT, NM- NL, I	NRAO	25[3]
ON	Onsala, Sweden	Onsala Space Observatory	20

1. All antennas with affiliation of NRAO are located in the USA. UM refers to University of Manchester. BR refers to Brewster, WA. FD refers to Fort Davis, TX. HN refers to Hancock, NH. KP refers to Kitt Peak, AZ. LA refers to Los Alamos, NM. MK refers to Mauna Kea, HI. NL refers to North Liberty, IA. OV refers to Owens Valley, CA. PT refers to Pie Town, NM.
2. Interferometer, equivalent solid surface diameter.
3. All these antennas have the same diameter.

7.2 The best clean image of SN 1993J from VLBI observations

This section will present the best clean image of SN 1993J using real visibility data from VLBI observations taken on 2007 Nov. 3. We use the results from our simulation study, namely the best selection of parameters in the CLEAN algorithm, to make the best clean image of SN 1993J. The main characteristics of the best clean image in comparison to other clean images would be that the image errors are as small as possible, to be more reliable for the interpretation of the brightness modulation along the ridge of the projected shell, and that the resolution is as high as possible to show small features of the structure of SN 1993J.

As an important result from our simulation study we used the best selection of parameters namely (C, +2, 4000, 0.05), where C is the weighting scheme, +2 refers to the robustness factor, 4000 refers to clean components and 0.05 refers to gain. To obtain a clean image, the deconvolution process was carried out to reduce the level of the sidelobes. Then the clean components and the residuals from the deconvolution process were added and convolved with a Gaussian-restoring clean beam with a diameter that was chosen to be roughly equal to, or slightly larger than, the maximum axis of an elliptical Gaussian fit to the inner portion of the beam pattern from the robustness-weighted visibility data. The deconvolution process was carried out interactively and the clean cycle terminated when 4000 clean components were produced in the cleaning process. According to our simulation study, about 99 % of the flux density is cleaned. That is clearly sufficient.

This clean image is the best one in terms of small image errors and therefore best suited for the purpose of astrophysical interpretation and to obtain useful information about the nature of SN 1993J. It will be also used to search, with relatively high angular resolution, for a PWN that may exist in the centre of SN 1993J (see section 7.5).

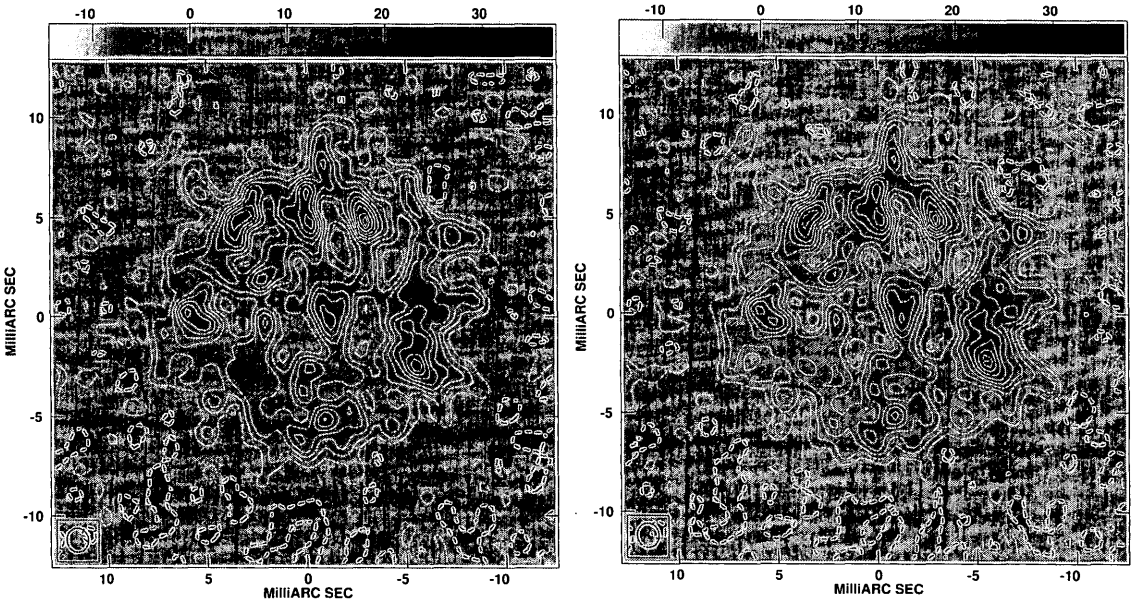

Figure 7.2 Left Panel: Best (this thesis) clean image of SN 1993J from VLBI observations on 2007 Nov. 3. The contours are drawn at -10, 10, 20, 30, 40, 50, 60, 70, 80, 90 and 95% of the peak brightness of 37.0 μJy/beam. The FWHM contour of the Gaussian convolving beam is given in the lower left. Right panel: clean image of SN 1993J from VLBI observations taken on 2007 Nov. 3 (Bietenholz and Bartel 2008). The contouring scheme and the location of the beam display are as in the left panel. The peak brightness is 34.2 μJy/beam.

In Figure 7.2 we show one clean image (left panel) and give the important characteristics in Table 7.2. For comparison we also show the previously equivalent image made by

Bietenholz and Bartel (2008). We give the main characteristics for this image also in Table 7. 2. We compare several key characteristics of these clean images, namely the

Table 7.2 The key information of the VLBI images of SN 1993J

VLBI images 1 of SN 1993J	B_{max} 2 (μJy/beam)	B_{min} 3 (μJy/beam)	σ_{noise} 4 (μJy/bea)	σ 5 (μJy/beam)	FWHM, *p.a.* 6 (mas), (deg)
This thesis	37.0	-13.8	3.1	4.0	1.20 × 1.07, 10.2
Bietenholz and Bartel (2008)	34.0	-13.9	3.1	4.0	1.22 × 1.08, 10.2

1. VLBI images of SN 1993J using real data taken from VLBI observations on 2007 Nov. 3. The first row shows data for the clean image made for this thesis using weighting scheme C, robustness factor 2, clean components 4000 and gain 0.05. The second row shows data for the image made by Bietenholz and Bartel (2008) using NA weighting (robustness factor +5), clean components 2000 and gain 0.05.
2. The peak brightness of the clean image.
3. The minimum value of the brightness of the clean image.
4. The background rms of the brightness of noise of the clean image measured over 190 mas x 60 mas.
5. The image errors of the clean images. For more information, see chapter 7.3.
6. The FWHM and p.a. of the elliptical Gaussian clean beam.

maximum and minimum brightnesses B_{max}, B_{min}, σ_{noise}, and the beam size. As can be seen from Table 7.2 the maximum brightness of the clean image made for this thesis (first row) is 37.0 μJy/beam or about 9 % larger than that of the clean image shown in the right panel, while B_{min} is almost the same. Also σ_{noise} remains the same. The FWHM of both clean images of SN 1993J are slightly different. The

resolution of the image made for this thesis is slightly higher than the resolution of the image made by Bietenholz and Bartel (2008) because of weighting with the smaller robustness factor. This thesis confirms in general the good ad-hoc choice of parameters for the clean image of Bietebholz and Bartel (2008).

On the ridge there are several condensations namely in the north, south-west, south-east and east and also south. The brightness distribution apparently varies around the ridge of the projected shell. We want to figure out whether this variation is real or due to image errors. Further, in the centre of the projected shell there is an apparent source of radio emission. This source in the best image of SN 1993J (left panel) is slightly stronger than that in the image shown in the right panel. What is this apparent emission? Does it come from a PWN or a black hole or is it just due to image errors? Through this study we will try to find out the answer for these important questions.

7.3 Comparison of the best clean image of SN 1993J with the simulated image

In this section we discuss how image errors influence the characteristics and the quality of VLBI images by comparing the best clean image of SN 1993J with the image from our simulation study. For this purpose we first present the best clean image of SN 1993J and the simulated image in Figure 7.3. Both images were made using the same selections of parameters, namely (C, 4000, 2, 0.05). We summarize the key characteristics of both

images in Table 7.3. We see that there are some differences in B_{max}, B_{min} and σ_{noise}, but we think that they are due to the randomness of the data and not important. The

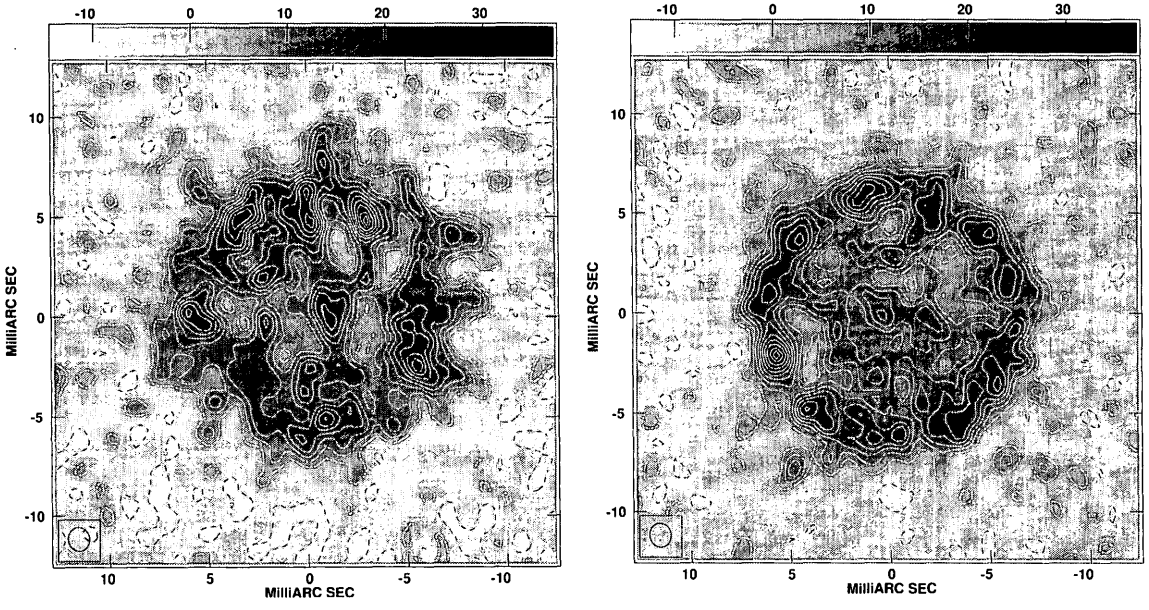

Figure 7.3 Left panel: The best image of SN 1993J made using data from VLBI observations on 2007 Nov. 3 as shown in Figure 7.2 (left panel) and again shown here for easy comparison. Right panel: The simulated image. The contours are drawn at -10, 10, 20, 30, 40, 50, 60, 70, 80, 90 and 95 % of the peak brightness of 37.0 μJy/beam for the best clean image of SN 1993J and 39.0 μJy/beam for the simulated image.

surprising result is relatively small values of rms_{diff} and $rms_{diff}/\sigma_{noise}$. In particular, $rms_{diff}/\sigma_{noise}$ was from our simulation study in Chapter 6 in general between 1.4 and 1.7. We do not quite understand why this ratio is so small and it seems that special attention is necessary if used for important conclusions.

Table 7.3 Key characteristics of the best clean image of SN 1993J and the simulated image

Image 1	B_{max} 2 (μJy/beam)	B_{min} 3 (μJy/beam)	$\sigma_{noise,SN}$ 4	σ_{noise} 5 (μJy/beam)	rms_{diff} 6 (μJy/beam)	$rms_{diff}/\sigma_{noise}$ 7 (μJy/beam)	σ 8 (μJy/beam)	FWHM, p.a. 9 (mas), deg
best	37.0	-13.8	3.1	———	———	———	4.0	1.20 × 1.07, 10.2
sim	39.0	-19.0	———	2.9	3.8	1.31	———	1.20 × 1.07, 10.2

1. The best and simulated images shown in Figure 7.3.

2. The peak brightness of the best clean image of SN 1993J and the simulated image. First row shows data for the clean image of SN 1993J using real data for the combination of (C, 4000, 2, 0.05). The second row is for the simulated image for the symmetric spherical shell model for $\theta_0=15.0$ mas, for the selection of (C, 4000, 2, 0.05) and the u-v coverage, full. Note that B_{max} of the simulated image is for the image as shown in Figure 7.3 and not for the model image as in chapter 6.

3. The minimum value of the brightness of the best clean image of SN 1993J and the simulated image.

4. The background rms of the brightness of noise of the best clean image of SN 1993J measured over 190 mas x 60 mas.

5. The background rms of the brightness of noise of the simulated image of SN 1993J measured over 190 mas x 60 mas.

6. The parameter rms_{diff} refers to image errors for the simulated image.

7. The ratio of the rms_{diff} to σ_{noise} for the simulated image. This ratio was used to determine the image errors of the best clean image as described in section 7.2.

8. The parameter σ refers to image errors of the best clean image of SN 1993J.

9. The FWHM and p.a. of the elliptical Gaussian clean beam.

The best clean image of SN 1993J and the clean image from simulated data both show strong brightness modulations. The apparent modulation along the ridge of the simulated image is not real but just due to image errors because the symmetric spherical shell model Figure 4.1 in Chapter 4 does not show any variation of the brightness along the ridge of the shell. By comparison of the clean image of SN 1993J with the simulated

image we realize that the strength of the modulation looks fairly similar in the real and simulated image. However, the images look quite different. The image in the left panel clearly has pronounced emission in the north and the west, while the simulated image has apparently random variations in the brightness along the ridge. So while the small--scale variations in brightness may not be real in the image in the left panel, the large-scale variations could indeed be real. We will next determine the image errors and then address the question of the reality of modulations again more quantitatively in Chapter 8.

7.4 The image errors of the best clean image of SN 1993J

The main goal in this study is to measure the image errors in the best clean image of SN 1993J. Since all VLBI images of SN 1993J and also images of other radio supernovae are subject to image errors, therefore, understanding how the errors can be estimated is of considerable importance. We have made the best clean image of SN1993J with small image errors using results from simulations of VLBI observations. Now, we want to explain how the image errors of the clean image of SN 1993J are determined. For this purpose , we first take σ_{noise} and the ratio rms_{diff} to σ_{noise} for the simulated image which used the same set of imaging parameters as was used for the best clean image of SN 1993J (Table 7.3). Then we determine the rms brightness of the noise over the empty region, $\sigma_{noise,SN1993J}$ of the best clean image of SN 1993J. The image errors of the best clean image of SN 1993J are estimated by

$$\sigma = (rms_{diff}/\sigma_{noise}).(\sigma_{noise,SN1993J}) \qquad (7.1)$$

As a result, from our simulation study, the ratio of the $rms_{diff}/\sigma_{noise}$ for the simulated image for the best selection of parameters in the CLEAN algorithm, namely (C, 4000, 2, 0.05), is 1.3 (see Table 7.3). We use this ratio to estimate the on-source image error of the clean image of SN 1993J. The background rms brightness of the noise of the best clean image of SN 1993J, $\sigma_{noise,SN1993J}$ (Figure 7.2, left panel), is 3.1 μJy/beam. Then the on-source image error for our best clean image of SN 1993J is $\sigma = 4.0$ μJy/beam. We list this value also in Table 7.3.

7.5 VLBI search for a pulsar wind nebula in the centre of SN 1993J

In this study the best clean image from VLBI observations of SN 1993J with small image errors and relatively high resolution is used for the purpose of our astrophysical interpretation. This image is capable of giving us information about possible radio emission from a compact source in the centre of SN 1993J. As elaborated in section 3.4.2, SN 1993J originated from the explosion of a massive star of $\sim 25 M_{sol}$. At epoch 2007 Nov. 3, SN 1993J was 14 years old and has been expanding since then so that the shell may have become sufficiently large that a search for a neutron star or a black hole at the centre of the supernova remnant might become successful. The question we want to address here is whether the apparent emission seen in the centre of SN 1993J could be due to a PWN

or black hole and if not, what the upper limit on the luminosity of any compact source in the centre would be?

7.5.1 Determining the upper limit of the spectral luminosity of any central compact source

The peak brightness in the centre of the best clean image of SN 1993J is ~ 23 μJy/beam and the peak brightness in the centre of the simulated image is ~ 19 μJy/beam. Also, given an rms_{diff} of 3.8 μJy/beam (see line # 2 in Table 7.3), the peak brightness in the centre of the best clean image is just 6.1 times larger. Taking these results together we conclude that the peak in the centre of the best clean image of SN 1993J is not real. It was just not found to be significantly strong enough to be undoubtedly from the remnant of the explosion. We will therefore place an upper limit on the flux density of any PWN or a source associated with a black hole (BH) that may exist in the centre of SN 1993J.

To place an upper limit on the brightness of any PWN, we run the AIPS task IMSTAT over the inner region with a radius from the centre of SN 1993J of 10% of that of the cleaned area to measure the rms of the brightness. Then we put the upper limit on the brightness of the PWN , B_{PWN}, as

$$B_{PWN} \langle 5\sigma_{centre} \qquad (7.2)$$

where σ_{centre} denotes the rms brightness for the region around the centre. We determined σ_{centre} = 5.5 μJy/beam. We then get

$$B_{PWN} = 28 \quad \mu\text{Jy/beam}$$

This is clearly larger than the peak in the centre, so we are on the conservative side estimating the upper limit. Bietenholz et al. (2003) reported that no compact source was found in the central region of SN 1993J. They place an upper limit on the brightness of 50 μJy/beam at 8.4 GHz. Our upper limit on the brightness of any compact source in the centre is 28 μJy/beam. Since any compact source is thought to be clearly smaller than the beam, we obtain an upper limit on the flux density of $S_{PWN} < 28$ μJy. Further, having an upper limit on the flux density for any central source such as a PWN enables us to place an upper limit on the spectral luminosity, L_{PWN}. We want to express the spectral luminosity of the PWN in the centre of SN 1993J in terms of the spectral luminosity of the Crab nebula. The spectral lumino- sity of a source with flux density, S, and a distance from Earth of d, is

$$L = S 4\pi d^2 \qquad (7.3)$$

The spectral luminosity of a PWN with flux density, S_{PWN}, at the distance of $d_{SN1993J}$ is

$$L_{PWN} = (S_{PWN}).(4\pi d_{SN1993J}^2) \qquad (7.4)$$

and the spectral luminosity of the Crab nebula is

$$L_{Crab}=(S_{Crab}).(4\pi d^2_{Crab}) \qquad (7.5)$$

The flux density of the Crab nebula at 5 GHz at the distance, d_{Crab}, of 2 kpc is 600 Jy (see Kafatos, 1985), and the upper limit on the flux density in the centre of SN 1993J at 5 GHz at the distance $, d_{SN1993J},$ of 4 Mpc is determined to be 28 μJy. In order to state L_{PWN} in the centre of SN 1993J in terms of L_{Crab} we have

$$L_{PWN}=\frac{S_{PWN}}{S_{Crab}}.\left(\frac{d_{SN1993J}}{d_{Crab}}\right)^2 \qquad (7.6)$$

which gives us

$$L_{PWN}<0.19\,L_{Crab} \qquad (7.7)$$

This is our conservative relative upper limit on the spectral luminosity of any PWN, or emission region associated with a black hole, that should exist in the centre of the shell of SN 1993J.

Chapter 8

Discussion of Results

In this chapter we discuss the results from investigations of image errors of the clean images made from simulated VLBI observations as described in Chapter 6. Specifically, we present a discussion of the modulation of the brightness along the ridge of the shell of the clean images of SN 1993J from earlier epochs, namely, a) 1996 Dec. 13 and 1997 Nov. 15, b) the epoch that has been mainly used for this thesis, 2007 Nov. 3, and c) the latest epoch of VLBI observations, 2010 Mar. 5. The epochs are chosen as to represent images with diameters of ~ 5.6 mas, 15.0 mas and ~ 19.5 mas, respectively, which approximately match the diameters in our simulation study. We compare the clean images of SN 1993J from these different epochs with the corresponding clean images made from simulated visibility data to figure out whether the modulation of the brightness in the VLBI images is real or just due to image errors. When we say that the modulation is real, we mean is that modulation is present along the ridge of the shell. Furthermore, we discuss the central area of the clean images of SN 1993J and the brightness limit for any compact source in the center of SN 1993J that may be expected there.

In Chapter 6 we found that clean images for different models of supernovae, namely the symmetric spherical shell model and the asymmetric spherical shell model, have similar values for the image errors as long as they have been made from the same selection of parameters in the CLEAN algorithm. In other words, the image errors of the clean images are fairly independent of the shell model of the supernova. That is an important result in the context of evaluating the reliability of the brightness distribution in the whole series of observations of SN 1993J and simplities further discussion whether brightness variations along the ridge of the shell are real or not since physically it is expected that the structure of the supernova changes with time. We now want to use our results and discuss examples of images of SN 1993J.

8.1 Comparison of the clean images of SN 1993J from different epochs of VLBI observations with our simulations for different θ_o

This section is devoted to discussing whether the apparent modulation of the brightness along the ridge of the shell for several already published and unpublished examples of images of SN 1993J is real or due to image errors. To shed more light on this crucial question we compare the clean images of SN 1993J from different epochs of VLBI observations with the clean images made from simulated visibility data for the symmetric spherical shell model, for θ_o = 5.6, 15.0 and 19.5 mas, weighting scheme C, robustness factor 0, clean components 20000, gain 0.08 and the full u-v coverage.

8.1.1 Comparison of clean images of SN 1993J from VLBI observations with the simulated image for θ_o = 5.6 mas

In Figure 8.1 we present a few clean images of SN 1993J from two different epochs of VLBI observations at 5.0 and 8.4 GHz and compare them with the simulated image for θ_o=5.6 mas (Figure 8.2) to investigate the modulation of the brightness along the ridge. Based on the acquired results from our analysis as described in detail in Chapter 6 we measured relatively small image errors for the simulated image with θ_o=5.6 mas (see Table 6.5 line # 3). As is seen in Figure 8.2, the brightness along the ridge of the shell is fairly uniform and no strong modulation was found.

Now we want to evaluate the variation of the brightness around the ridge of the shell for each of the clean images of SN 1993J which are shown in Figure 8.1, based on our simulation study. We list the key characteristics of the four images and the simulated image in Table 8.1. As we learned from our simulation study, the ratio of $rms_{diff}/\sigma_{noise}$ is about 1.6. This means that the image errors are 1.6 times larger than the background noise rms. For the number of 4000 for the clean components and a gain of 0.05, the ratio is, as mentioned in Chapter 7, surprisingly smaller, namely 1.3 (see # 2 in Table 7.2). To be conservative, we used a value of, 1.6 to estimate the image errors for each clean image shown in Figure 8.1.

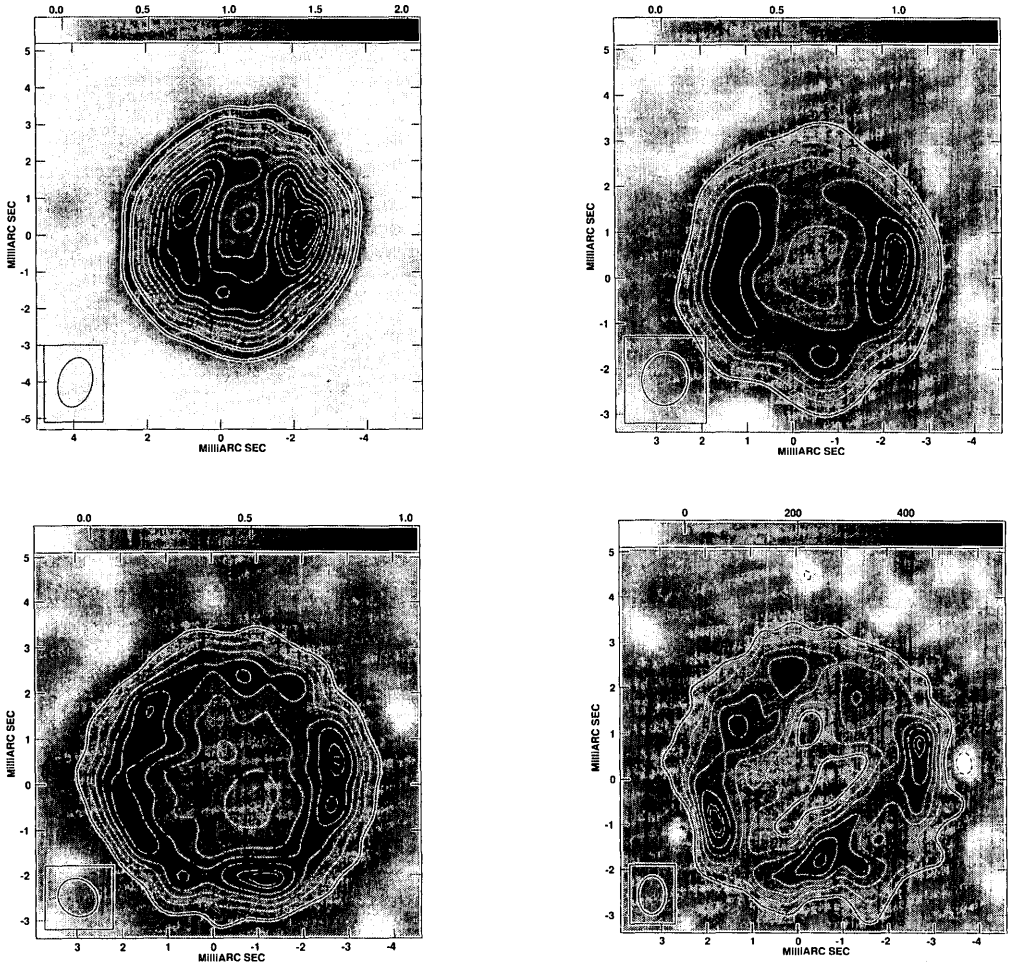

Figure 8.1 Clean images of SN 1993J from earlier epochs of VLBI observations at 5.0 and 8.4 GHz. The left panels are for 5.0 GHz and the right panels are for 8.4 GHz. First row: Clean images of SN 1993J taken on 1996 Dec. 13. The left panel was made from weighting scheme CS and robustness parameter 0.1. The right panel made from weighting scheme CS and robustness parameter 1. The contours are drawn at -10, 10, 20, 30, 40, 50, 60, 70, 80, 85, 90 and 95 of the peak brightness of 2.0 mJy/beam. Second row: Clean images of SN 1993J taken on 1997 Nov. 15. Both clean images were made from weighting scheme CS and robustness factor 0. The contours are drawn at -15, 15, 20, 30, 45, 60, 75, 90 and 95 of the peak

brightness of 1.0 (5.0 GHz) and 0.56 mJy/beam (8.4 GHz). Different grey scales were used for the images. All images of SN 1993J are taken from Bietenholz et al. (2002).

Table 8.1 Key characteristics of the clean images of SN 1993J and simulated image for θ_o=5.6 mas

Image 1	B_{max} 2 (μJy/beam)	B_{min} 3 (μJy/beam)	σ_{noise} 4 (μJy/beam)	$\sigma_{noise,SN}$ 5 (μJy/beam)	rms_{diff} 6 (μJy/beam)	$\frac{rms_{diff}}{\sigma_{noise}}$ 7	σ 8 (μJy/beam)	FWHM, p.a. 9 (mas), (deg)
5.0	2000.0	-130.0	———	31.9	———	———	51.1	1.37 ×0.91, -15.4
8.4	1300.0	-180.0	———	54.0	———	———	86.4	1.17 × 1.02, -8.84
5.0	1000.0	-160.0	———	43.0	———	———	68.8	0.91 × 0.82, -53.1
8.4	560.0	-110.0	———	28.1	———	———	44.9	0.83× 0.61, -1.75
sim	85.5	-20.0	3.2	———	5.1	1.59	———	1.07×1.04, 21.4

1. The first and third lines show VLBI observations of SN 1993J for 5.0 GHz, the second and the fourth lines are for 8.4 GHz. The fifth line is for simulation of VLBI observations for 5.0 GHz. The simulated image is based on observations on 2007 Nov. 3, for the symmetric spherical shell model with θ_0=5.6 mas, weighting scheme C, robustness factor 0, clean components 20000, gain 0.08 and u-v coverage full.
2. The peak of the brightness of the clean image.
3. The minimum value of the brightness of the clean image.
4. The rms of the background noise of the simulated image.
5. The rms of the background noise of the clean image of SN 1993J for different frequencies.
6. The image errors of the simulated image.
7. The ratio of the rms_{diff} to σ_{noise}. This ratio is an important indicator of image errors.
8. The image errors of the clean images of SN 1993J.
9. The FWHM of the Gaussian beam and the position angle.

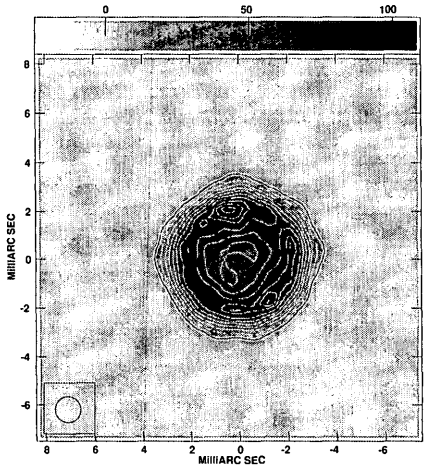

Figure 8.2 Clean image from Figure 6.6 in chapter 6 made from simulations of VLBI observations for the symmetric spherical shell model for θ_o=5.6 mas, weighting scheme C, robustness factor 0 and the full u-v coverage. The contours are drawn at -10, 10, 20, 30, 40, 50, 60, 70, 80, 85, 90 and 95 of the peak brightness, namely 107 μJy/beam .

How does our result compare with the variation of the brightness around the ridge of the image from the simulation study in Figure 8.2 ? We can see that the brightness varies between the 80% contour and the peak of 107 μJy/beam or by 21 μJy/beam. The background noise rms, σ_{noise}=3.2 μJy/beam, and multiplied by 1. 6 is 5.1 μJy/beam (see Table 8.1). The measured image errors for the simulated image are 5.1 μJy/beam. The maximum to minimum variation of the brightness along the ridge is therefore 4.1 times the image errors, a reasonable value. We now want to inspect the clean images in Figure 8.1 and figure out how large the variations are for these images. If they are equal or sma-

ller than those in the simulated image then we would have to conclude that the apparent variations are likely not real on the basis of our analysis. If they are larger, then they are most likely real.

First row left panel: For this particular image the image errors are 1.6 x σ_{noise} = 1.6 x 31.9=51.0 μJy/beam. Now we try to figure out whether the variation of the brightness around the ridge is real or caused by image errors. We measure the difference between the peak of 2.0 mJy/beam and the minimum at the 60% contour of the peak brightness around the ridge for the clean image of SN 1993J. This difference is = 800 μJy/beam or 15.7 times the image errors. This in an important result because based on the obtained value we can say that the variation of the brightness around the ridge is about 16 times larger than the image errors of the clean image. This means that the modulation of the brightness for this clean image of SN 1993J is almost certainly real.

First row right panel: For this particular image the image errors are 1.6 x σ_{noise} = 86.4 μJy/beam. Then we measure that the difference between the peak and the minimum is between 100% and ~ 75% of the peak brightness along the ridge of the shell. Since the peak brightness is 1.3 mJy/beam, the difference is 325 μJy/beam. This means that the variation of the brightness around the ridge is 3.8 times larger than the image errors of this clean image. That by itself would indicate that the variation of the brightness is not real. However, the images at 5.0 and 8.4 GHz have large similarities. We can therefore

conclude that the modulation of the brightness on the basis of the similar brightness distribution indicates that it is likely real after all. That probably means that our simulation analysis is quite conservative and that variations in brightness 3.8 times the image errors could still be real.

Second row left panel. The image errors for this particular image are 1.6 x σ_{noise} = 68.8 μJy/beam. We measure that the difference between the peak and minimum is between 100% and 55% of the peak brightness along the ridge of the shell. Since the peak of the brightness is 1.0 mJy/beam, the difference is 450 μJy/beam. This means that the variation of the brightness around the ridge is 6.5 times larger than the image errors for this clean image. Then we can conclude that the variations of the brightness around the ridge of the shell are almost certainly real.

Second row right panel: For this particular image the image errors are 1.6 x σ_{noise} = 45.0 μJy/beam. We measure that the difference between the peak and the minimum of the brightness around the ridge is between 100% and 40% of the peak brightness along the ridge of the shell. Since the peak of the brightness is 0.56 mJy/beam, the difference is 340 μJy/beam. This means that the difference is 7.6 times larger than the image errors. Now we can again infer that the variation of the brightness around the ridge is real.

So we conclude on the basis of our analysis and on the comparison between images that the brightness around the ridge is not uniform but shows variations. In particular the

western and eastern parts in the 1996 images show strong emission while the pattern of emission is more complex in 1997. This variation may have resulted from a non-uniform shocked CSM around the supernova, inhomogeneities in the ejecta and possibly also from Rayleigh-Taylor fingers stretching out from the contact surface.

8.2.2 Comparison of the best clean image of SN 1993J with the simulated image for θ_o = 15.0 mas

In this section we investigate the modulation of the brightness distribution along the ridge of the shell for a clean image of SN 1993J with different sizes of the FWHM of the Gaussian clean beam. The first one is the best clean image of SN 1993J (epoch 2007 Nov. 3) as shown in Chapter 7 (Figure 7.2, left panel). We display it here again in Figure 8.3 (upper left panel). First we discuss the modulation of the brightness along the ridge for the high-resolution image of SN 1993J as we call it the best clean image in Chapter 7 earlier. We discuss, now quantitatively, the comparison of the best clean image of SN 1993J made for the combination of (C, 4000, 2, 0.05) with the simulated image of the symmetric spherical shell model with θ_o = 15 mas, for the combination of (C, 4000, 2, 0.05, the full u-v coverage) (Figure 7.2, right panel). By comparing these two images quantitatively we are trying to figure out in detail whether the variations of the brightness along the ridge of the shell are real or due to image errors. We list the main characteristics of the images in Table 8.3.

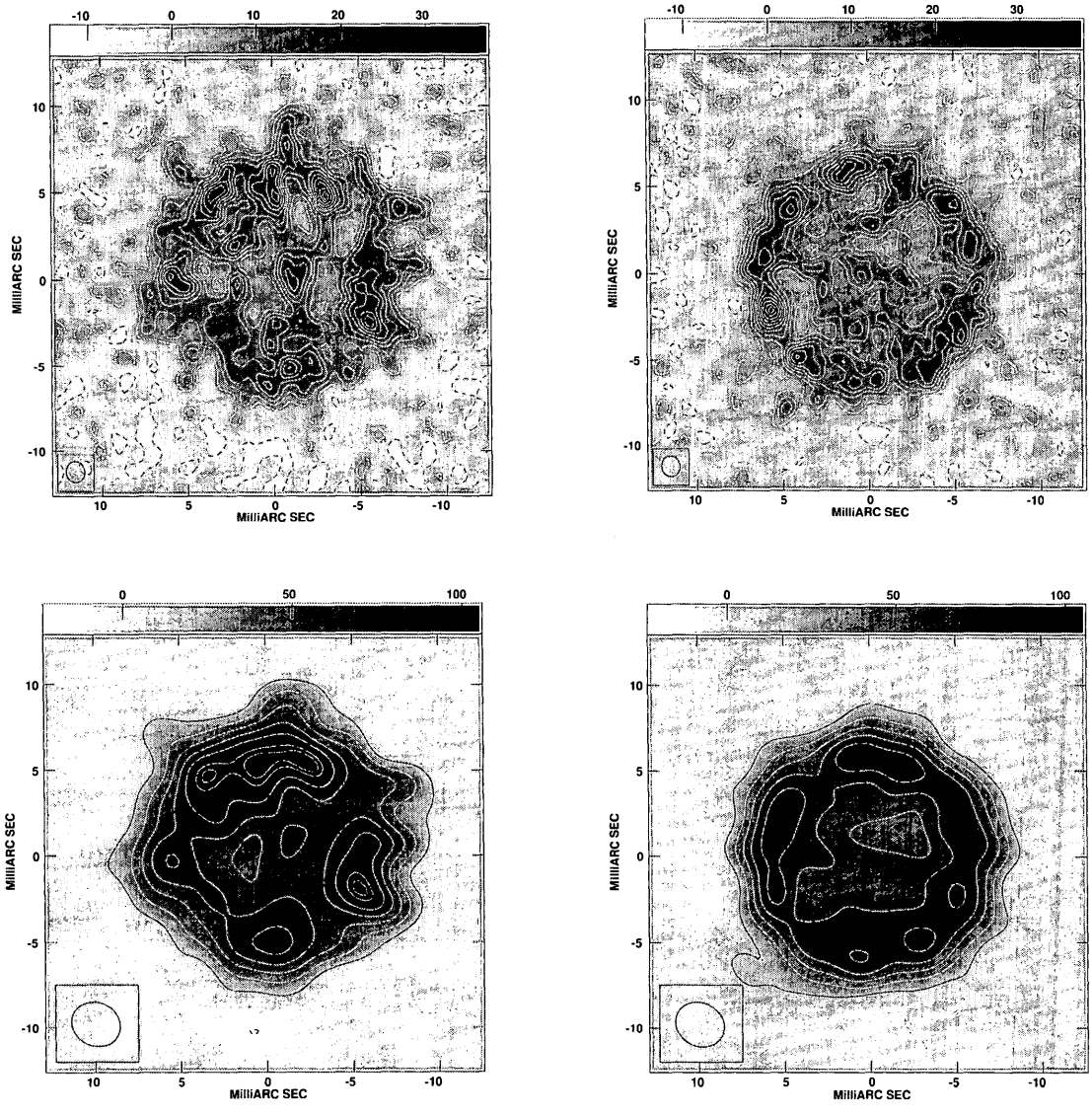

Figure 8.3 First row, left panel: The high-resolution image of SN 1993J taken on 2007 Nov. 3 as shown in Figure 7.2 (left panel) and again shown here for easy comparison. Right panel: The high-resolution simulated image. The contours are drawn at -10, 10, 20, 30, 40, 50, 60, 70, 80, 90 and 95 % of the peak brightness 37.0 μJy/beam for the best clean image of SN 1993J and 39.0 μJy/beam for the simulated image. Second row: Left panel is the image of SN 1993J from first row left panel, but now tapered. Right panel is the tapered simulated image from the first row. The contours of the tapered image of SN 1993J are drawn at -15, 15, 30 , 45, 60 , 75, 90 and 95% of the peak brightness 104.5 μJy/beam. The contours of the of the simulated image are drawn at -15, 15, 30, 45, 60 , 75, 90 and 95% of the peak brightness 108.0 μJy/beam.

First, we want to investigate the modulation of the brightness around the ridge for the best clean image (high-resolution) of SN 1993J. We estimated the image error, σ, to be 1.3 x σ_{noise} = 1.3 x 3.1= 4.0 μJy/beam (see Table 7.2 for the ratio of $rms_{diff}/\sigma_{noise}$). However, for this discussion, we think that the ratio of $rms_{diff}/\sigma_{noise}$ = 1.3 is unusually low and to be conservative we again use a ratio of 1.6 as in section 8.1.1. The image error is therefore 1.6 x 3.1= 5.0 μJy/beam. We measure that the difference between the peak and the minimum is between 100% and 10% of the peak brightness along the ridge of the shell. Since the peak is 37.0 μJy/beam, this difference is 33.3 μJy/beam. This tells us that the variation of the brightness around the ridge is 6.7 times larger than the image error. That would indicate that the variation of the brightness is real. The small-scale variation in brightness is however very similar to that of the simulated image. As indicated already in Chapter 7, the large-scale structure appears to be systematic, clearly not random as in the simulated high-resolution image.

We therefore tapered the version of the clean image of SN 1993J to find out whether or not the large-scale modulations of the brightness along the ridge of the expanding shell are clearly real and perhaps more significantly so than the small-scale modulation. We limited the length of the longest baselines of the u-v coverage as so to produce a clean image with the size of the beam which is close to the size of the beam of the clean image of SN 1993J made from the latest VLBI observations taken on 2010 Mar. 5 (see Chapter 8.2.3). This tapered clean image is shown in Figure 8.3 (lower panel).

Table 8.2 Key characteristics of the best clean images of SN 1993J and the simulated images for 2007 Nov. 3

Image 1	B_{max} 2 (μJy/beam)	B_{min} 3 (μJy/bea)	σ_{noise} 5 4 (μJy/beam)	rms_{diff} 5 (μJy/beam)	σ 6 (μJy/beam)	FWHM, (mas), p.a. 7 (deg)
High-res	37.0	-13.8	3.1	—	4.0	1.02 × 1.07, 10.2
Simulated image, high-res	39.0	-19.0	2.9	3.8	—	1.02 × 1.07, 10.2
Tapered	104.5	-22.1	4.87	—	7.8	2.90 x 2.53, 61.8
Simulated image tapered	108.8	-27.1	4.54	7.2	—	2.90 x 2.53, 61.8

1. The high-resolution image of SN 1993J taken on 2007 Nov. 3 and the high-resolution simulated image. Also given are the tapered and the simulated tapered versions of the images in the first two rows.
2. The peak brightness of the clean image.
3. The minimum value of the brightness of the each image.
4. The background rms of the brightness of noise of each image.
5. The parameter rms_{diff} refers to image errors for both simulated images.
6. The parameter σ refers to image errors of the high-resolution and the tapered image of SN 1993J. The parameter σ was computed so as to increase σ_{noise} by the factor of $rms_{diff}/\sigma_{noise}$ from the simulated image. For the high-resolution image, to be conservative, we increased σ to 5.0 (see text).
7. The FWHM and position angle of the elliptical Gaussian clean beam.

Using the tapering procedure means that we down-weighted the longer baselines. It has the effect of making the beam larger. A broader pattern may emerge that could again be checked to see whether the variation of the brightness distribution is real. This is also advisable in view of the 2010 Mar. 5 clean image of SN 1993J at 1.7 GHz, which has a larger beam and should be compared with the 5.0 GHz image here (see Chapter 8.2.3). We discuss the modulation of the brightness along the ridge for the tapered clean image

with the FWHM of the beam of 2.90 mas x 2.53 mas (Figure 8.3, lower left panel). We also show the tapered simulated image in Figure 8.3 (lower right panel). We want to investigate the modulation of the brightness around the ridge for this tapered clean image of SN 1993J. The image errors of this particular image are 1.6 x σ_{noise} = 1.6x 4.9 = 7.8 μJy/beam. Now we are going to measure the difference between the peak and the minimum that is between 100% and 50% of the peak brightness along the ridge of the shell. Since the peak is 104.5 μJy/beam, this difference is 52.2 μJy/beam. This means that the variation of the brightness along the ridge is 6.7 times larger than the image errors. Then we can again infer that the modulation of the brightness along the ridge is real.

It is interesting to measure the difference between the peak and the minimum of the brightness along the ridge of the simulated tapered image. We measure that to be between 100% and 75% of the peak brightness. Since the peak is 108.8 μJy/beam, this difference becomes 27.2 μJy/beam. The image errors of the simulated image are 1.6 x 4.5= 7.2 μJy/beam. This means that the difference of the brightness along the ridge is 3.7 times larger than the image errors. This confirms that the tapered clean image has large-scale brightness variations that are clearly larger than in the tapered simulated image and are therefore indeed real.

8.2.3 Comparison of the clean image of SN 1993J for 2010 Mar. 5 with the simulated image for θ_o = 19.5 mas

In this section we present the clean image of SN 1993J from the latest epoch of VLBI observations taken on 2010 Mar. 5 at 8.4 GHz (Bietenholz et al. 2011) along with the image made from a simulation of VLBI observations for the symmetric spherical shell model with θ_o=19.5 , weighting scheme C, robustness factor 0, clean components 20000, gain 0.08 and the full u-v coverage. The latter image was tapered so as to have approximately the same beam size as the clean image from 2010 Mar. 5. We compare these clean images to investigate the pattern which appears along the ridge of the shell. The images are shown in Figure 8.4 and their characteristics listed in Table 8.3.

Now we are going to investigate the modulation of the brightness around the ridge of the shell for the latest image of SN 1993J using the obtained result from our simulation study. The image errors of this clean image are 1.6 x σ_{noise} = 1.6 x 3.7= 5.9 μJy/beam. We measure that the difference between the peak and the minimum is between 100% and 45% of the peak brightness along the ridge of the shell. Since the peak is 117 μJy/beam, the difference is 64.4 μJy/beam. This means that variations of the brightness along the ridge are 10.9 times larger than the image errors. Now we can again infer that variations of the brightness around the ridge are real.

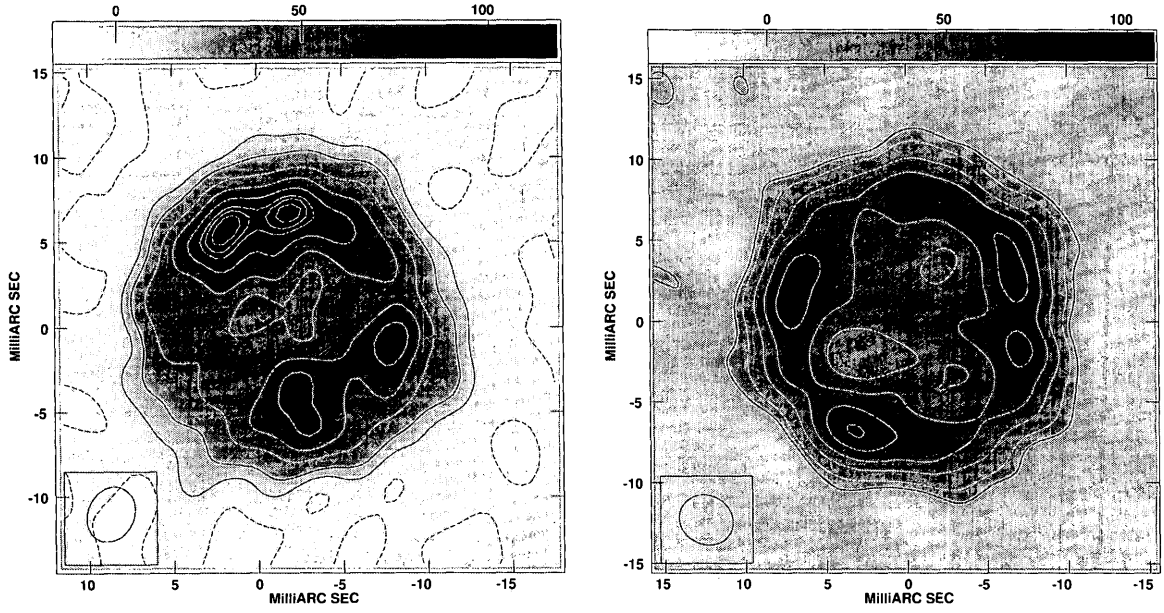

Figure 8.4 The left panel shows a clean image of SN 1993J from VLBI observations taken on 2010 Mar. 5 at 8.4 GHz. The contours are drawn at -18, 0, 9, 18, 36, 54, 72, 85, 90 and 95% of the peak of the brightness of 117.0 μJy/beam. This clean image was made using weighting scheme C and robustness parameter 0, clean components 5000, gain 0.67 . The right panel shows the simulated clean image for the symmetric spherical shell model, θ_o=19.5 mas, weighting scheme C, robustness factor 0, clean components 20000, gain 0.08 and the full u-v coverage. The clean image of SN 1993J is taken from Bietenholz et al. (2011).

Table 8.3 Key characteristics of the clean image of SN 1993J and the simulated image for θ_o=19.5 mas for 2010 Mar. 5

Images 1	B_{max} 2 (μJy/beam)	B_{min} 3 (μJy/beam)	σ_{noise} 4 (μJy/beam)	rms_{diff} 5 (μJy/beam)	σ 6 (μJy/beam)	FWHM, p.a. 7 (mas), deg
2010 Mar. 5	117	-14.7	3.7	——	5.9	3.34 × 2.75, -25.8
simulated image tapered	107	-31.7	4.4	7.0	——	3.42 × 3.02, 61.7

1. First row is for the clean image of SN 1993J taken on 2010 Mar. 5. Second row is for the simulated image based on observations on 2007 Nov. 3 for the symmetric spherical shell model, θ_0=19.5 mas, weighting scheme C, robustness factor 0, clean components 20000, gain 0.08 and the u-v coverage full.
2. The peak of the brightness of the clean image.
3. The minimum value of the brightness of the clean image.
4. The rms of the background noise of the clean image.
5. The parameter rms_{diff} refers to image errors of the tapered, simulated image.
6. The parameter σ refers to image errors of the clean image of SN 1993J. For the computation of σ, see Table 8.2.
7. The FWHM of the Gaussian beam and the position angle.

It is also interesting to find out the variation of the brightness around the ridge of the shell in comparison to the image errors for the simulated image. The image errors of the simulated image are 1.6 x σ_{noise} = 1.6 x 4.4= 7.04 μJy/beam. We measure that the difference between the peak and the minimum of the brightness is between 100% and

85% of the peak brightness along the ridge of the shell. Since the peak is 107 μJy/beam, the difference is 16.1 μJy/beam. This means that the variation of the brightness along the ridge is 2.3 times larger than the image errors. This is a rather small relative variation around the ridge compared with the previous values of ~ 3.7 (section 8.2.2). It may indicate that our limit of ~ 4.5 for real radiation variations is conservative. We can also compare the 2010 Mar. 5 image with the 2007 Nov. 3 image. It is clear that they are similar. The northern, southern and south-western emission regions appear in both images. This is further indication that the brightness variations are real.

Now we want to summarize our discussion regarding the variation of the brightness distribution around the ridge of the shell.

1. The modulation of brightness in images from the 1996 and 1997 epochs of VLBI observation are definitely real or, in case of the 8.4 GHz 1996 image, likely real since the pattern is similar for the 5.0 GHz and 8.4 GHz images even though the variation of the brightness is only ~ 4 times larger than the image errors.

2. The variation of brightness in the high-resolution clean image of SN 1993J taken on 2007 Nov. 3 is 6.7 times larger than the image errors. However, this variation of brightness is similar to the variation of brightness in the high-resolution simulated image casting doubt on whether the variations in the clean image are real. The variation of

of brightness in the tapered clean image of SN 1993J is also 6.7 times larger than the image errors and the pattern is clearly not random Then we can infer that at least the large-scale variation of the brightness around the ridge of the shell is real.

3. The variation of brightness in the clean image of SN 1993J taken on 2010 Mar. 5 is 10.9 times larger than the image errors, and the variation pattern is similar to that of the tapered clean image of SN 1993J taken on 2007 Nov. 3. This means that the apparent variation of the brightness is also real.

4. However, how many details of the brightness variations are real depends on how much larger they are than the image errors.

Chapter 9

This chapter is devoted to summarizing the conclusions of this thesis.

1. We made a simulation study on the basis of VLBI observations taken on 2007 Nov. 3 and investigated in detail how noise and the incomplete u-v coverage contribute to image errors and how these errors are affected by the a) model supernova, b) outer angular diameter, c) weighting scheme, d) robustness factor, e) number of clean components, f) gain and g) u-v coverage.

2. Image errors arise mostly due to noise and the incomplete u-v coverage.

3. Image errors were found to be ~ 1.6 times larger than the background noise.

4. Image errors are fairly independent of a supernova model. Any asymmetries of the brightness distribution would therefore not largely affect our results.

5. Image errors increase with the outer angular diameter of the symmetric spherical shell model for a constant beam size.

6. Image errors can be reduced by adjusting parameters in the CLEAN algorithm, namely weighting scheme, robustness factor, number of clean components and gain. We determined that the best image for our VLBI observations with a good compromise between small image errors and good resolution are weighting scheme C,

robustness factor 2, clean components 4000 and gain 0.05.

7. Image errors appear to be affected by the number of clean components in the CLEAN algorithm. Using a larger number of clean components produces somewhat larger image errors in the clean images even if the cleaned flux density remains close to 100 % of the total flux density.

8. Image errors are affected by the gain. Using a larger gain in the CLEAN algorithm produces somewhat larger image errors in the clean images even if, again, the cleaned flux density remains close to 100% of the total flux density.

9. We introduced the formula used to estimate the image errors of the best image of SN 1993J. This formula is $\sigma = (rms_{diff}/\sigma_{noise}).(\sigma_{noise,SN1993J})$. The best image of SN 1993J had small estimated image errors of only 4.0 μJy/beam. Also we place an upper limit on the spectral luminosity of any compact component, likely a PWN, in terms of the spectral luminosity of the Crab nebula of $L_{PWN} < 0.19\, L_{Crab}$.

10. On the basis of our simulation study we conclude that the images from observations of 1996, 1997, 2007 and 2010 all have brightness modulations that are real. One marginal case is the image from 1996 Dec. 13 at 8.4 GHz. Here we infer the reality of the modulation on the basis of the similarities of the modulation pattern between

the images at 5.0 and 8.4 GHz. Our simulation study in this case indicates that the results from it are conservative.

Chapter 10 Future work

In this thesis our main objective was to determine image errors for one epoch of observations and to find the combination of parameter values that would give us the best clean image. The parameters were: model of a supernova, size, weighting scheme, robustness factor, number of clean components, gain and u-v coverage. Each of these parameters had up to 11 values. Ideally, we could have tried all possible combinations of parameter values to find the best combination. However, that would have clearly be beyond the scope of the thesis. Instead we chose a particular path through the multi -dimensional parameter space. This path was determined by the range of parameter values we considered, the sequence we chose in varying the values of one parameter and leaving the other parameters fixed at particular values and the choice we made as to which parameter values we left fixed. This strategy naturally allows for many other approaches. In fact, at the end of our analysis we noticed that the sequence should perhaps have been chosen differently. We think that it would have been better to start the sequence with varying the number of clean components and then the gain first. We realized at the end that the selection of 20,000 clean components and a gain of 0.08 was not the optimal choice for having these values as fixed parameter values while varying all the other parameter values. To our surprise, the number of clean components and the gain were quite sensitive parameter values for the image errors. Future work could start

with determining the optimal number of clean components, likely 4000 as we determined and the optimal gain, likely 0.05 as we determined, that would give close to 100% of the total flux density in the clean image and then vary the other paramete values in the sequence we used in the thesis.

Another improvement could be by doing our analysis for different epochs of VLBI observations. Observations were made at about 37 epochs. In this thesis we used the results from the analysis with different sizes to match roughly observations at earlier and a later epoch. A better way would have been to do the simulation analysis on the basis of those observations and not on the basis of the observations at the particular epoch we chose for the thesis. Again, the number of 37 epochs is clearly too large for the analysis in this thesis. Future work could be done with simulations on the basis of observations at different epochs to see how accurate our discussion of image errors for observations at the earlier epochs and the later epoch was.

Further improvements could be made regarding an analysis with different supernova models. A more complex asymmetric model could be included in the simulation analysis. Perhaps a better assessment of the significance of the brightness modulation around the ridge could then be made. Also, we found relatively large image errorsfor the disk model. It would be interesting to know which combination of parameter values could reduce these image errors. However, a disk brightness distribution is only expected at the very

early epochs. For SN 1993J the supernova was so compact at these epochs that a detailed image could not be made. Therefore such an analysis would only be of limited practical use.

Bibliography

Bartel, N., Rogers. A. E. E., Shapiro, I.I., Gorenstein, M. V., Gwinn, C. R., Marcaide, J. M., Weiler, K. W. 1985. *Hubble's constant determined using very-long baseline interferometry of a supernova,* Nature, 318, 25

Bartel, N. 1985. *Angular diameter determinations of radio supernovae and the distance scale.* Supernovae as distance indicators; Proceedings of the Workshop, Berlin and New York, Springer-Verlag, 107-122

Bartel, N., Rupen, M.P., Shapiro, I.I., Preston, R. A. and Rius, A. 1991. A *high-resolution radio image of a young supernova,* Nature, 350, 212

Bartel, N., et al. 1994. *The shape, expansion rate and distance of supernova 1993J from VLBI measurements,* Nature, 369, 584

Bartel, N., Rupen, M. P. and Shapiro. I. 1987. IAU. Circ., 4292, 2. Edited by Marsden. B.G

Bartel, N., et al. 2000. *The Changing Morphology and Increasing Deceleration of Supernova 1993J in M81,* Science, 287, 112

Bartel, N., Bietenholz, M. F., Rupen, M. P., Beasly, A.J., Graham, D.A., Altunin, V.L., Venturi, T., Umana, G., Canon, W. H. and Conway, J.E. 2002. *SN 1993J VLBI II.*

Related Changes of the deceleration, flux density decay, and spectrum, ApJ, 581, 404

Bartel, N. and Bietenholz, M. F. 2003. SN 1979C VLBI: 22 Years of Almost Free Expansion, ApJ, 591, 301

Bartel. N., Bietenholz. M. F., Rupen. M. P., and Dwarkadas, V.V. 2007 *SN 1993J VLBI. IV. A Geometric Distance to M81 with the Expanding Shock Front Method,* ApJ, 668, 924

Bartel. N. and Bietenholz. M. F., 2008. *Shell Revealed in SN 1979C,* ApJ, 682,1065

Bartel. N. and Bietenholz. M.F. 2008. Private communication

Bartel. N. and Bietenholz. M. F., 2013. *Recent developments in supernova research with VLBI.* Proceeding IAU Symposium No. 296, in press

Beswick. R. J. 2006. *Radio Supernovae*. Proceedings of the 8th European VLBI Network Symposium, p.51

Bietenholz, M. F., Bartel, N. and Rupen, M.P. 2001. SN 1993J VLBI. I. *The Center of the* Explosion and a Limit on Anisotropic Expansion, ApJ, 557, 770

Bietenholz, M., Bartel, N. and Rupen, M.P . 2002. *SN 1986J VLBI: The Evolution and Deceleration of the Complex Source and a Search for a Pulsar Nebula,* ApJ, 581, 113

Bietenholz, M. F., Bartel, N. and Rupen, M.P. 2003. *SN 1993J VLBI. III. The Evolution of* the Radio Shell, ApJ, 597, 374

Bietenholz, M. F., Bartel, N. and Rupen, M.P. 2004. *Discovery of a Compact Radio Component in the Center of Supernova 1986J,* Science, 304,1947

Bietenholz, M. F. and Bartel, N., 2008. *The evolution of the central component in SN 1986J.* Advances in Space Research, Volume 41, Issue 3, p. 424-428.

Bietenholz, M. F., Bartel, N., Rupen, M.P. and Dwarkadas, V.V. 2010. Proceedings of the 10th European VLBI Network Symposium and EVN Users Meeting*: VLBI and the new generation of radio arrays.*

Bietenholz. M. F., Bartel. N. and Rupen, M.P. 2010 *Supernova 1986J Very Long Baseline Interferometry. II. The Evolution of the Shell and the Central Source,* ApJ, 712, 1057

Briggs, D. S.1995. *High Fidelity Deconvolution of Moderately Resolved sources*. Ph.D. Thesis, New Mexico Institute of Mining and Technology

Brunthaler, A., Martí-Vidal, I., Menten K. M., Reid, M, J., Henkel, G. C., Falcke, H., Feng, H., Kaaret, N. R., Morgan, A. N. and Weib, A. 2010. VLBI observations of SN 2008iz. I. *Expansion velocity and limits on anisotropic expansion,* A&A 516, A27

Burke, F., Graham-Smith, F. 1997. *An Introduction to Radio Astronomy*. Cambridge.

Chevalier, R. A. and Fransson, C. 1994. *Emission from Circumstellar Interaction in normal Type II Supernovae,* ApJ, 420, 268

Chevalier, R. A. 2012. C*ommon envelope evolution leading to supernovae with dense interaction,* ApJ, 752,

Heywood, I., Blundell.ö M. K., Klöckner, H., and Beasley. A.J .2009. *The radio remnant of SN 1993J: an instrumental explanation for the evolving complex structure,* Mon. Not. R. Astron. Soc. 392, 855–867

Höflich. P., Langer, N. and Duschinger .M. 1993. *Supernova 1993J- Explosion of a Massive Cool Supergiant with a Small Envelop Mass,* A&A 275, 29

Hogbom, J. 1974, *Aperture Synthesis with a Non-Regular Distribution of Interferometer Baselines,* A & A Supplement Series 15, 417.

Jauncey, D.L., Kemball, A., Bartel, N., Shapiro,I. I., Whitney, A, R., Rogers, A. E. E., Preston, R, A. and Clark, T.A .1998. *Supernova 1987A- A radiosphere resolved with VLBI five days after the neutrino burst,* Nature. 334.412

Manchester, R.N., Gaensler, B.M., Wheaton, V.C., Staveley-Smith, L., Tzioumis, A. K., Bizunok. N. S., Kesteven, M. J and Reynolds. E. 2002. *Evolution of the Radio Remnant of SN 1987A: 1990-2001, Publ.* Astron. Soc. Aust,19, 207

Marcaide, J. M. et al. 1993. IAU Circ., 5820, 2. Edited by Green, D. W. E

Marcaide, J. M. et al. 1994. *Radio-size estimates of SN 1993J,* ApJ, 424, 25

Marcaide, J. M. et al. 1995. *Discovery of shell-like structure of SN 1993J,* Nature, 373, 44

Marcaide, J. M. et al. 1995. *Expansion of SN 1993J,* Science, 270, 1475

Marcaide, J. M., Martí-Vidal, I., Alberdi, A. et al. 2009a. A&A, 505, 927

Marcaide, J. M., Martí-Vidal, I., Perez-Torres, M. A. et al. 2009b, A&A, 503,869

Marcaide, J. M. and Martí-Vidal, 2012. *Highlights of the expansion of SN 1993J.*

Proceedings of Science

Marscher A. P. 1985 . " *Distance determinations of Extragalactic Supernovae*". 130 Proceeding Cambridge, Springer- Verlag

Martí-Vidal. I., et al. 2011. The ApJ, 668, 924

Ng, C-Y., Potter. M. P., Staveley-Smith. L., Gaensler. B.M. and Phillips. C, et al. 2011. *First VLBI detection of the radio remnant of supernova 1987A: evidence for small-scale features*. ApJ, 728, 15

Phillips, J. A., Kulkarni, S.R., Skiff, B., Hanzel. D., 1993 IAU., 5775, 1. Edited by Green, D. W. E

Pooley, G.G., Green, D.A., Romanishin, W. 1993. IAU Circ., 5773, 1. Edited by Green, D. W. E

Rohlfs, K. & Wilson, T. L. 1996. *Tools of Radio Astronomy* (Second ed.) Springer Verlag

Henry, Richard., *The Crab Nebula and Related Supernova Remnants*. Edited by Minas C. Kafatos

Schlegel, E.M et al 1996. The AJ, 111, No 4

Tingay, S,. et al. 2009. Proceedings of the 8th International e-VLBI Workshop.

Thompson, A. R., Moran, J. M., & Swenson, G. W. 1986. *Interferometry and Synthesis in Radio Astronomy*. John Wiley & Sons.

Van Dyk, S.D., Weiler, K. W., Sramek, R. A., Rupen, M. P., Panagia, N., 1993. BASS, Vol. 25, No. 4, p. 1339

Weiler, K. et al. 1994. BAAS, 185th AAS Meeting, 33.06

Weiler, K. et al. 2007. ApJ , 671, 1959

Zelik, M., Gregory, S. A. and Smith, E.v.P, 1992 *Introductory Astronomy & Astrophysics*. Third Edition. Saunders